STUDY OF GREEN'S FUNCTIONS OF POTENTIALS AND FIELDS IN LAYERED MEDIA COMPOSED OF LEFT-HANDED AND RIGHT-HANDED MATERIALS

by

Aytaç Alparslan

A Thesis Submitted to the
Graduate School of Engineering
in Partial Fulfillment of the Requirements for
the Degree of

Master of Science

in

Electrical & Computer Engineering

Koç University

September, 2008

Koç University
Graduate School of Sciences and Engineering

This is to certify that I have examined this copy of a master's thesis by

Aytaç Alparslan

and have found that it is complete and satisfactory in all respects,
and that any and all revisions required by the final
examining committee have been made.

Committee Members:

Prof. M. İrşadi Aksun

Prof. Alphan Sennaroğlu

Assoc. Prof. Hakan Ürey

Assoc. Prof. Özgür Esat Müstecaplıoğlu

Date:

To my parents

ABSTRACT

Green's functions of vector and scalar potentials, and fields have been studied in layered media composed of materials with positive and negative refractive indices, also referred to as right-handed and left-handed materials, respectively. Since Green's functions are nothing but the potentials or fields due to a given point source in a given environment, they facilitate the use of the superposition integral to calculate the radiation from an arbitrary source in the same environment, as the Maxwell equations are linear for linear materials. To begin with, the derivation of the spectral-domain Green's functions in planarly layered media is reviewed with the detailed investigation of their singularities, namely, the surface wave poles, branch-point singularities, and the leaky wave poles. To incorporate left-handed materials and real metals at optic frequencies into the study of multilayered structures, the salient features of such materials are reviewed, with a special emphasis on their response to electromagnetic waves. Once the spectral-domain Green's functions have been studied in multilayered structures composed of any kind of materials, artificial and/or natural, their spatial-domain counterparts are obtained by i) numerical integration of the time-consuming Sommerfeld integrals, and ii) the discrete complex image method. Although there are contributions in both parts of the study, the main contribution of this work is to obtain the closed-form approximations to the spatial-domain Green's functions that can account for any wave nature - spherical, cylindrical, and conical - at any distances from the source location, i.e., near-, intermediate- and far-field zones. Although the main engine of this approximation is the discrete complex image method, which was extensively used and discussed in the literature on the closed-form approximations of the spatial-domain Green's functions, its implementation has been modified in order to capture the branch-point contributions of the integrals. As a result of this work, it was demonstrated that the closed-form Green's functions in the spatial domain can be obtained efficiently and accurately in all ranges of materials and distances.

Keywords: Green's functions, layered media, left-handed materials, 3-level DCIM, surface waves, surface plasmon polaritons

ÖZETÇE

Kırılma indisi pozitif (doğal malzemeler) ve negatif (solak malzemeler) olan malzemelerden oluşturulan katmalı yapıların skalar ve vektörel potansiyel ve alan Green's fonksiyonları çalışıldı. Green's fonksiyonları, noktasal bir kaynağın, herhangi bir geometride oluşturduğu alan veya potansiyel bilgisi olduğundan ve lineer yapılarda Maxwell denklemleri lineer olduğundan, herhangi şekildeki bir yapının oluşturacağı alan veya potansiyel bilgisi Green's fonksiyonlarının bindirme integralleri ile elde edilebilir. Başlangıç olarak, katmalı yapılarda spektral tanım kümesindeki Green's fonksiyonlarının elde edilmesinin üzerinden geçildi ve bu yapılarda oluşabilecek olan tekillikler detaylı olarak incelendi. Solak malzemeleri ve optik frekanslarındaki metalleri de katmalı yapılarda kullanabilmek için, bu tür yapıların dikkat çekici özellikleri elektromanyetik dalgalara olan tepkileri göz önünde tutularak araştırıldı. Katmanlı yapılarda (yapılar doğal malzemeler, solak malzemeler v.b. oluşabilir) spektral tanım kümesindeki Green's fonksiyonları elde edildikten sonra, uzamsal tanım kümesindeki karşılıkları iki yolla elde edildi: 1) zaman alıcı Sommerfeld integrallerini nümerik olarak alarak, ve 2) ayrık karmaşık imge metodu kullanılarak. Bu tezde, her iki kısma da katkılar yapılmasına karşın en önemli katkı spektral tanım kümesindeki Green's fonksiyonlarının kapalı-form yaklaşık değerlerinin elde edilmesi olmuştur. Yaklaşık değerlerin elde edilmesinde, literatürde yaygın bir şekilde kullanılan ve tartışılan ayrık karmaşık imgeler metodu çeşitli değişikler yapılarak kullanılmıştır. Bu değişiklikler sonunda, dallanma noktasının etkisi elde edilmiş ve çeşitli dalga tiplerinin (küresel, silindirik ve konik) kullanılmasıyla kaynağa olan her mesafede (yakın, ara ve uzak mesafeler), yaklaşık değerler doğru bir şekilde elde edilmiştir. Sonuç olarak, kapalı-form Green's fonksiyonlarının, uzamsal tanım kümesinde etkili, hızlı ve hatasız olarak elde edilebileceği gösterilmiştir.

Anahtar kelimeler: Green's fonksiyonları, katmanlı yapılar, 3-adım DCIM, solak malzemeler, yüzey dalgaları, yüzey plasmon polaritonları.

ACKNOWLEDGMENTS

I would like express my gratitude to Prof. M. İrşadi Aksun who has been a great source of inspiration and encouragement and also provided valuable comments and suggestions.

I would like to thank Prof. Alphan Sennaroğlu, Assoc. Prof. Hakan Ürey and Assoc. Prof. Özgür Esat Müstecaplıoğlu for being in my jury and reviewing the thesis.

I would like thank my friends who have been patient and provided me a moral support and optimism during the hard times of the research. I would like to thank my office friends, Pınar and Engin for their help and encouragement.

I would also like to thank The Scientific and Technological Research Council of Turkey (TÜBİTAK) for having provided the graduate scholarship during my M.S. study, and for the support of my research project under contract 105E141.

Finally, I thank my family for their endless support and love, which made it possible to achieve my goals in my life.

TABLE OF CONTENTS

LIST OF TABLES

LIST OF FIGURES

NOMENCLATURE

DCIM	Discrete Complex Image Method
EM	Electromagnetics
GPOF	Generalized Pencil of Function
HED	Horizontal Electric Dipole
HMD	Horizontal Magnetic Dipole
LHM	Left Handed Material
RHM	Right Handed Material
SIP	Sommerfeld Integration Path
SPP	Surface Plasmon Polariton
SWP	Surface Wave Pole
TL	Transmission Line
VECT-FIT	Vector Fitting
VED	Vertical Electric Dipole
VMD	Vertical Magnetic Dipole

Chapter 1

INTRODUCTION

From the time Marconi and his assistants successfully achieved the propagation of electromagnetic waves over large distances on earth, way beyond the line-of-sight distance to the horizon, in early 1900s, radiation from infinitesimal dipoles, horizontal and vertical with respect to the layer interface, have attracted a great deal of interests [1]. Originally, the main interest was to understand the physical mechanisms of the wave constituents of electromagnetic wave propagation over a lossy medium, in order to better design the first versions of today's widely used wireless communication systems. Once this goal has been achieved successfully, with the help of the mathematical derivations of the fields due to dipoles in layered media, it was realized that electromagnetic fields play as important role in the analysis and design of high-frequency circuits as voltages and currents do in the low frequency circuits. In other words, circuits operating in short wavelength regime, as compared to the size of the circuit components, require the field quantities, rather than voltages and currents, to asses their performances through their terminal parameters, such as the input and output impedances, powers delivered to the load or drawn from the circuits, etc. Therefore, recognizing the linearity of Maxwell's equations in linear media, fields of a dipole source in a given medium have been treated as the impulse responses of the medium, facilitating the analysis of arbitrary current density profile in the same medium via superposition integral. When this view is coupled with the advancement of the computational power of personal computers and workstations, it has paved the way for rigorous analysis of devices, circuits and even systems, which were computationally intractable until recently, resulting in a flurry of activities in the field of computational electromagnetics and optics. To be more specific, Green's functions have played an important role in the development of one of the key numerical techniques employed in the analysis of layered structures in microwave and antenna applications, namely, the method of moments, during the last three decades [2–12].

Based on this evolutionary and chronological order of the perceived importance of dipole radiation, it is safe to state that Green's functions in the spatial domain are now important for the sake of computational efficiency of the analysis of printed structures in multilayered environment. Therefore, most of the recent study on Green's functions have concentrated on their efficient computation. To appreciate the proposed methods and approaches in the literature to achieve this task, Green's functions in the spectral and spatial domains need to be defined, in general terms, in planar multilayered media first. For now, it would be sufficient to known that spectral-domain Green's functions in planar multilayered structures can be obtained analytically, and their spatial-domain counterparts are obtained either through inverse Fourier transform or inverse Hankel transform integrals (the latter is also known as Sommerfeld integral), both of which require integration of complex and oscillatory functions over infinite domains [6,13]. Based on this knowledge, it is obvious that there could be two different approaches to improve the computational efficiency of these transformation integrals: i) improving the computational efficiency of numerical evaluation of the integrals via some transformation techniques [14–16], ii) trying to approximate the transformations in closed forms [17–31]. As can be seen from the list of references for the latter approach, which is by no means a complete list, the approximation of the spatial-domain Green's functions in closed forms have attracted significant amount of interest in computational EM community. The work in this thesis falls into the second category, and the contributions can be stated as follows: i) closed-form approximations of the spatial-domain Green's functions are improved to account for the conical waves, which is due to the branch-point singularities of the spectral-domain Green's functions; ii) singularities of the spectral-domain green's functions defined for multilayered planar structures composed of natural and artificial materials are investigated; iii) Green's functions defined for planar slabs of left-handed materials and real metals, which may support surface plasmons, as well as surface waves and conical waves, have been studied; iv) closed-form expressions of the spatial-domain Green's functions of potentials and fields have been obtained in general multilayered environment, including layers that have been made up of LHMs, RHMs and real metals.

It would be instructive to give a brief historical development of the closed-form approximations of the spatial-domain Green's functions via discrete complex images, which are nothing but spherical waves originating from a set of complex image points in space. The first published result on the discrete complex images of a dipole source in a half space or in a microstrip structure is considered to be the article by D. G. Fang et. al., in 1988 [17], where they proposed approximating the spectral-domain Green's functions in terms of complex exponentials, and transforming them into the spatial domain analytically with the help of the Somerfeld identity. However, there were a couple of issues that rendered the algorithm inefficient and not-robust, which were, namely, i) the inaccuracy of the resulting image representation for intermediate and large distances (beyond a few wavelength, even less, depending upon the geometry), ii) the noise sensitivity and instability of the exponential approximation algorithm used in the work, the Prony's method. As a result, they had to use the so-called "relay race" approach, in which complex images were used up to a distance, beyond which the surface-wave pole contributions were used only. It is understandable that not being able to predefine the switching distance encouraged the researchers to find a single expressions for all ranges involved. As a result, unified closed-form expressions for the spatial-domain Green's functions were derived specifically for thick microstrip substrates [18], carrying almost the same problems as those of the previous approach, except for the relay race implementation. The method starts with the extraction of the surface-wave poles (SWP) and quasi-static terms (corresponding to the large spectral portion of the inverse Hankel transform integrals, or to the low frequency limit), and then, the rest is approximated in terms of complex exponential functions via Prony's method. Hence, the transformation integral, i.e., the Sommerfeld integral, can be evaluated analytically in closed forms facilitated by the known analytical transforms of the SWP contributions, quasi-static terms and the discrete complex-image terms. Even though the proposed approach had a few problems to be resolved, which are, namely, i) the geometry specific extraction of the quasi-static terms, ii) the noise sensitivity of Prony's method, and iii) the large amount of samples required for the implementation of Prony's method, it has inspired some new work and provided the underlying algorithm for the following work. This approach was first extended to microstrip structures with a superstrata [19], still suffering from almost the same problems as the original approach. However, with the introductions of the generalized pencil-of-function method for exponential approximation [20], which is much less noise sensitive as compared to Prony's method and its variants, and the two-level sampling algorithm [21], which significantly reduces the number of samples required for the exponential approximation, the algorithm has proved to have a potential to be robust and accurate for all ranges of distances. Since then, there have been a plenty of publications that propose improvements and/or new approaches for the closed-form representation of the spatial-domain Green's functions, and this thesis is also one of them, trying to improve the original algorithm to incorporate any types of materials and to cover any ranges of distances.

It is imperative to define the basic steps of the derivation of the spectral-domain and spatial-domain Green's functions, in order to provide the details of the contributions in this thesis. Therefore, Chapter 2 starts with the derivation of these Green's functions in unbounded media, and followed with the derivations in multilayered media. Then, the wave constituents of dipole radiation in layered media are discussed, and transformation between the spectral-domain and spatial-domain representations are provided with critical study of the surface wave poles. In Chapter 3, the fundamentals of the wave propagation in left-handed materials are given in addition to the discussions of the surface wave poles and other wave constituents in such materials. As the main contribution of the thesis, the derivation of the closed-form approximations of the spatial-domain Green's functions is introduced, with special emphasis given to the conical waves in certain layer configurations, and to the structures composed of LHMs and RHMs, all in Chapter 4. In order to cover the whole spectrum of the materials, several examples of layer configurations are studied and their results are provided in Chapter 4, for the sake of discussions and conclusions.

Chapter 2

GENERAL DERIVATIONS AND DISCUSSIONS OF GREEN'S FUNCTIONS

The concept of Green's function in electromagnetic problems is equivalent to the impulse response in circuit and system problems [13]. In circuit and system theory, if one knows the impulse response of a time-invariant linear system, the response of an arbitrary input signal can be simply calculated as the convolution of the impulse response with the input signal. Equivalently, the response of the system in the frequency domain can be determined by the multiplication of the Fourier transforms of the input signal and impulse response of the system, as the convolution operator in time domain corresponds to multiplication in frequency domain. In physical terms, Fourier transformation makes it possible to write the frequency content of signals by the use of functions which form an orthogonal set such as sines, cosines, complex exponentials, etc., in time domain. By taking the Fourier transform of the input signal and the impulse response of the system, one can easily obtain the frequency content of the output signal by a simple multiplication of the frequency domain representations of the input signal and the impulse response (the frequency domain representation of the impulse response is called the frequency response) of the system. To determine the output signal of the system in time domain, a Fourier transform must be performed. Note that the impulse input signal for circuit and system problems is defined in time domain, $\delta(t)$, as the input signals in such systems are usually functions of time. However, in EM problems, since the field and/or potential distributions due to an arbitrary source distribution in space are important, the impulse source in space will be the source for the Green's function. In other words, since Green's functions in EM problems play the role of the impulse response in system theory, point source, which is an impulse source in space, plays the role of the impulse function in time.

The field and potential Green's functions for general unbounded and layered structures in spectral domain will be be derived in sections 2.1 and 2.2, respectively. Then, in section

2.3, a basic discussion on transforming the spectral (spectrum: equivalent to the frequency domain in circuit and system theory) domain Green's functions into spatial (space: equivalent to time domain in circuit and system theory) domain will be given.

2.1 Derivation of Spectral-Domain Green's Functions in Unbounded, Homogeneous and Isotropic Media

Since electric and magnetic fields can be written in terms of vector and scalar potentials, their Green's functions can also be obtained from the Green's functions of the potentials using the same relations. So, the field expressions in terms of potentials are given below, skipping their derivations for the sake of brevity, [13]:

$$\mathbf{E}(\mathbf{r}) = -j\omega\mathbf{A}(\mathbf{r}) - \nabla\phi(\mathbf{r}) \tag{2.1}$$

$$\mu\mathbf{H}(\mathbf{r}) = \nabla\times\mathbf{A}(\mathbf{r}) \tag{2.2}$$

where $\phi(\mathbf{r})$ and $\mathbf{A}(\mathbf{r})$ are the scalar and vector potentials, respectively, and they are related by the Lorentz gauge as

$$\nabla\cdot\mathbf{A}(\mathbf{r}) = -j\omega\varepsilon\mu\phi(\mathbf{r}) \tag{2.3}$$

Note that $e^{j\omega t}$ time convention is used and suppressed in this work, and μ and ε are the permeability and the permittivity of the medium, respectively. Substituting (2.3) into (2.1) results in the following electric field expression in terms of the vector potential:

$$\mathbf{E}(\mathbf{r}) = -j\omega\left[\bar{\mathbf{I}} + \frac{\nabla\nabla}{k^2}\right]\cdot\mathbf{A}(\mathbf{r}) \tag{2.4}$$

where $\bar{\mathbf{I}} = \hat{x}\hat{x}+\hat{y}\hat{y}+\hat{z}\hat{z}$ is called the idem factor or idem diad. From (2.2) and (2.4) one can see that, if Green's function for the vector potential is known, Green's functions for the electric and magnetic fields can be obtained by simple differentiations. Hence, finding Green's functions for fields reduces down to obtaining Green's function for the vector potential, for which the governing equation is the inhomogeneous Helmholtz equation:

$$\nabla^2\mathbf{A}(\mathbf{r}) + k^2\mathbf{A}(\mathbf{r}) = -\mu\mathbf{J}(\mathbf{r}) \tag{2.5}$$

To find the Green's function for the vector potential, the source term is assumed to be an electric current dipole oriented in an arbitrary direction $\hat{\alpha}$, represented as $\mathbf{J}(\mathbf{r}) =$

$\hat{\alpha} Il\delta(\mathbf{r}-\mathbf{r}')$. Hence the solution of the Helmholtz equation for a point source is obtained as

$$\mathbf{A}(\mathbf{r},\mathbf{r}') = \hat{\alpha}\mu Il \frac{e^{-jk|\mathbf{r}-\mathbf{r}'|}}{4\pi|\mathbf{r}-\mathbf{r}'|} \tag{2.6}$$

where $\mathbf{r}$ and $\mathbf{r}'$ are the observation and source points, respectively, and $k(=\omega\sqrt{\epsilon\mu})$ is the wave number of the medium. Once the vector potential is obtained, substituting (2.6) into (2.4), and (2.6) into (2.2) would result in the electric and magnetic fields, respectively, in a homogeneous, isotropic and unbounded medium:

$$\mathbf{E}(\mathbf{r}) = -j\omega\left[\bar{\mathbf{I}} + \frac{\nabla\nabla}{k^2}\right]\cdot\hat{\alpha}\mu Il \frac{e^{-jk|\mathbf{r}-\mathbf{r}'|}}{4\pi|\mathbf{r}-\mathbf{r}'|} \tag{2.7}$$

$$\mathbf{H}(\mathbf{r}) = \nabla\times\hat{\alpha}\mu Il \frac{e^{-jk|\mathbf{r}-\mathbf{r}'|}}{4\pi|\mathbf{r}-\mathbf{r}'|} \tag{2.8}$$

So far, the Green's functions for potentials and fields have been obtained due to a dipole source in α-direction in an unbounded medium. For the sake of illustration and of getting some intuitive feelings, 3D plots of the magnitudes of the potentials and the field components of an x-directed dipole in free-space are provided in Figs. 2.2 - 2.7 at the operating frequency of $1.0GHz$. The data for these plots were obtained for the geometry shown in Fig. 2.1, where the source and observation planes are explicitly shown. It should be noted that all results

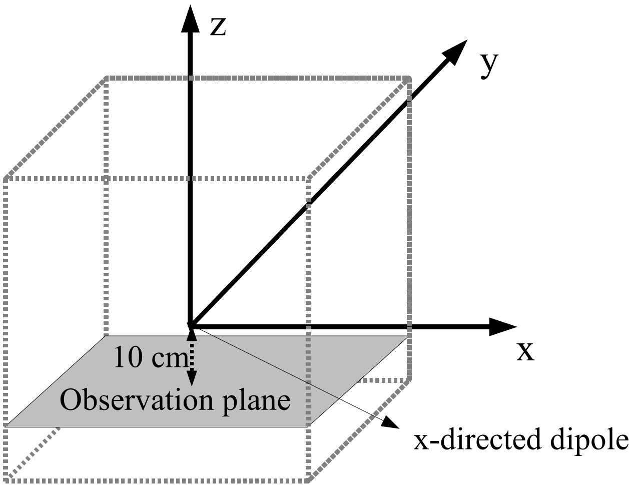

Figure 2.1: The locations of the x-directed dipole and the observation plane. (Observation plane is at z=-0.1 m.)

shown above are for an x-directed electrical dipole with unit strength, i.e., $Il = 1$ in (2.6),

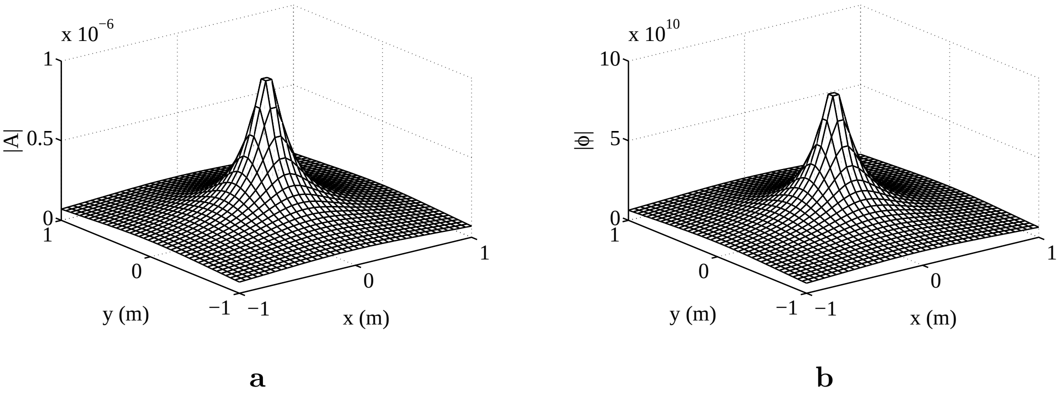

Figure 2.2: The magnitude of (a) vector and (b) scalar potentials on the observation plane shown in Fig. 2.1.

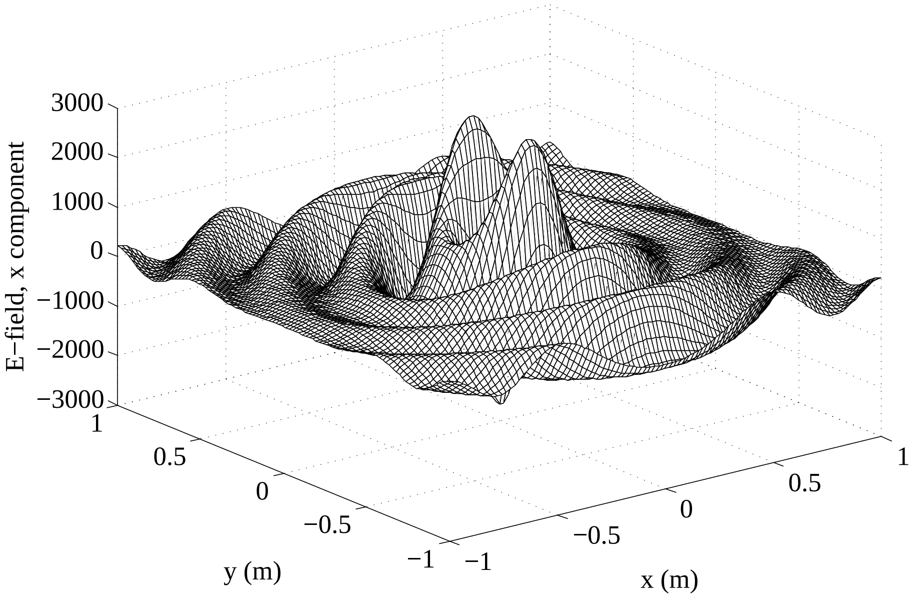

Figure 2.3: Real part of E-field, x component on the observation plane shown in Fig. 2.1.

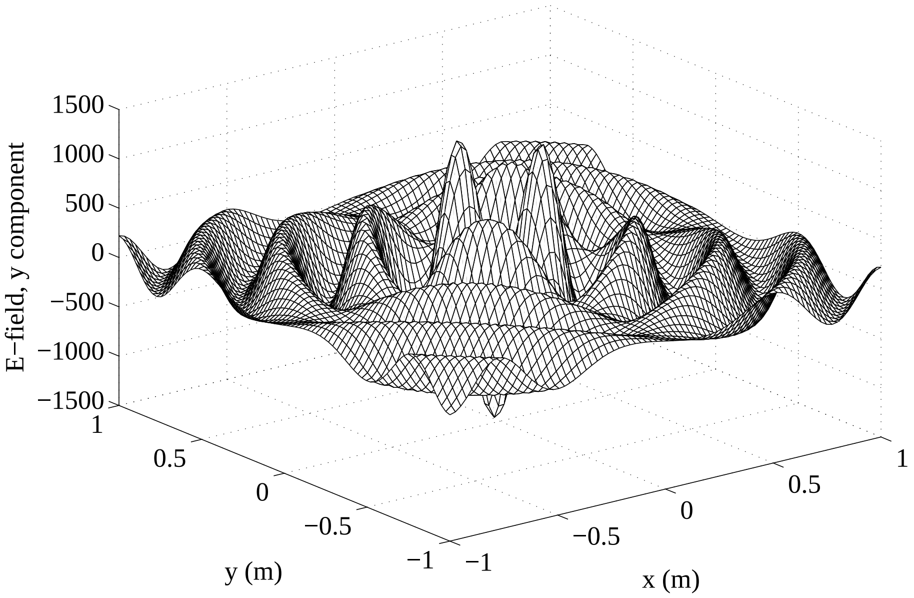

Figure 2.4: Real part of E-field, y component on the observation plane shown in Fig. 2.1.

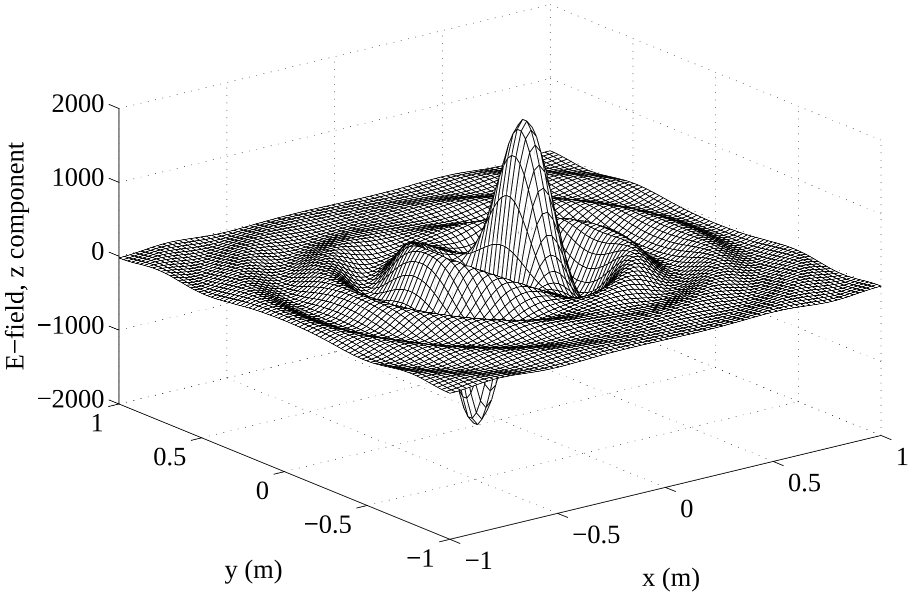

Figure 2.5: Real part of E-field, z component on the observation plane shown in Fig. 2.1.

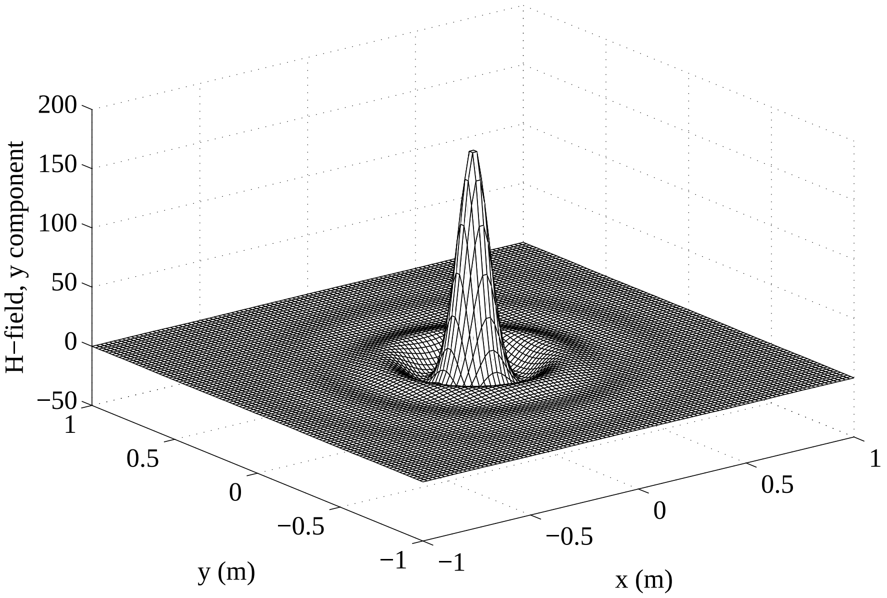

Figure 2.6: Real part of H-field, y component on the observation plane shown in Fig. 2.1.

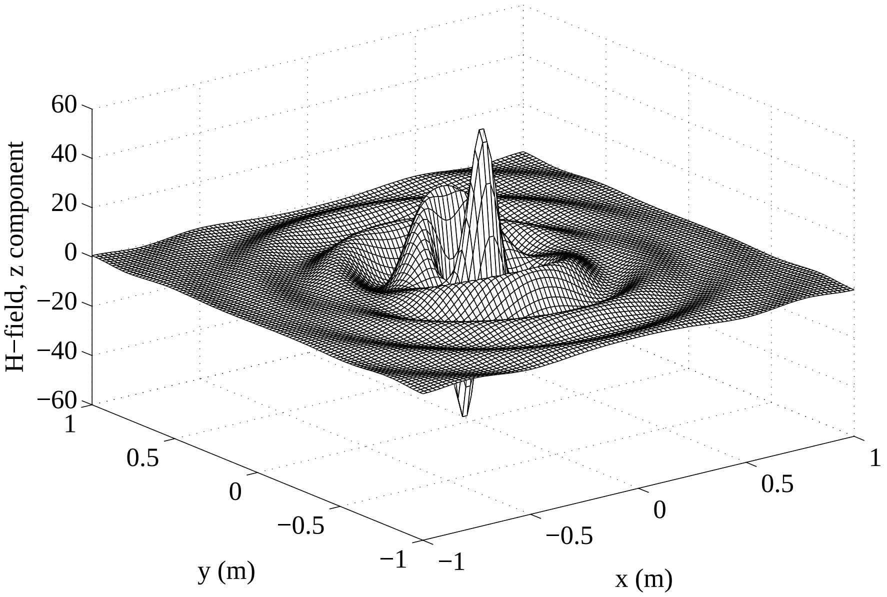

Figure 2.7: Real part of H-field, z component on the observation plane shown in Fig. 2.1.

and that the field results shown in Figs. 2.3 - 2.7 were obtained by numerical differentiation performed on the vector and/or scalar potentials, according to the expressions provided in (2.1) and (2.2).

2.2 Derivation of Spectral-domain Green's Functions in Layered Media

As a starting point of the study of Green's functions in layered media, the potential and field Green's functions in unbounded, homogeneous and isotropic media were derived and their relations with each other were obtained in section 2.1. Note that since the vector potential due to a point source in unbounded media can be represented in closed-forms as spherical waves, as given in (2.6), all Green's functions in the spatial domain were obtained analytically. However, this is not the case for a layered medium, where the Green's functions can usually be represented in closed forms in the spectral domain only. Therefore, in this section, the field and potential Green's functions in the spectral domain will be derived in a planarly layered structure, as shown in Fig. 2.8. Throughout this work, the location of the source is assumed to be the origin of the whole system, and the observation point(s) may be in any layer, with its coordinates specified as referenced to the origin.

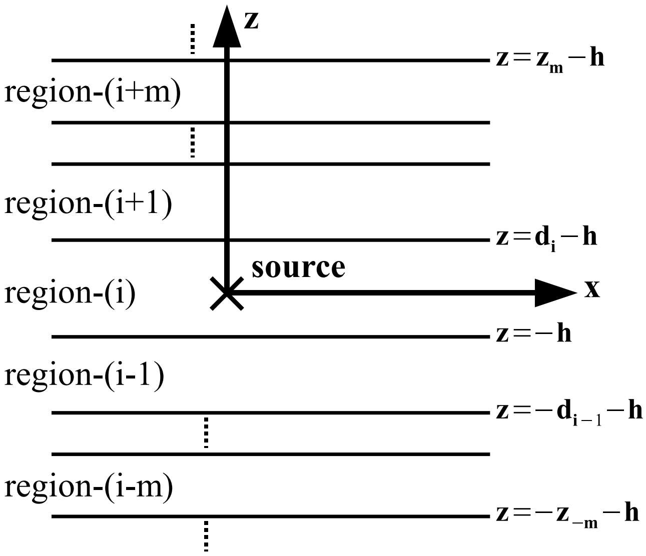

Figure 2.8: A general layered medium.

Based on a simple reasoning, Green's functions of the potentials and fields in layered media can be deduced from those obtained in unbounded medium by taking into account the reflections and transmissions at the planar interfaces of the layers. However, closed-form reflection and transmission coefficients at the planar interface between two media can only be defined for incident plane waves, and, as noted in section 2.1, Green's functions of the vector potential and the fields in an unbounded medium are in the forms of spherical waves and the spatial derivatives of the spherical waves, respectively. Therefore, the spherical wave nature of the solutions given in (2.1) and (2.2) need to be expanded in terms of plane waves by using the Weyl identity:

$$\frac{e^{-jkr}}{r} = \frac{1}{\pi} \int_{-\infty}^{\infty} \int_{-\infty}^{\infty} dk_x dk_y e^{-jk_x x - jk_y y} \frac{e^{-jk_z|z|}}{j2k_z} \tag{2.9}$$

where $k^2 = k_x^2 + k_y^2 + k_z^2$ and $|\mathbf{r}| = \sqrt{x^2 + y^2 + z^2}$. Note that (2.9) is the 2D inverse Fourier transform of the spectral-domain Green's functions obtained in an unbounded medium, and provides the plane wave spectrum of a point source, including the contributions of the evanescent spectrum ($k^2 < k_x^2 + k_y^2$, yielding dominantly imaginary k_z) as well as those of propagating spectrum ($k^2 \geq k_x^2 + k_y^2$, yielding dominantly real k_z.) Since the medium is translationally invariant on xy-plane, the phase matching condition requires that k_x and k_y are the same in all layers involved, leaving the propagation along the stratification to be determined in each layer only.

Before going into the details of the derivation of Green's functions in layered media, it would be instructive to address the issue of non-uniqueness of the potentials in layered media. In unbounded homogeneous media, it can be shown that a single vector component of the vector potential in the direction of the dipole is sufficient to define the rest of the fields. However, it is a well-known fact that this is not the case if there is a plane boundary, for which a single vector component cannot describe the electromagnetic field everywhere [5, 32]. This is due to the solenoidal behavior of the magnetic field generated by a dipole. In the case of an x-directed HED in a layered structure, as seen in Fig. 2.8, at least two components of the vector potential are needed, since the magnetic field generated by the dipole has two components on the boundary: one is normal (z component) and the other is parallel (y component) to the planar surface. Since the normal component is discontinuous, and the parallel component is continuous between two different regions, a single component of the vector potential cannot describe the overall magnetic fields in all the regions. Since the ultimate goal is to satisfy the boundary conditions of the fields at the interface, any combinations of the vector and scalar potentials that satisfy the necessary boundary conditions could be satisfactorily employed, as some suitable combinations were proposed in [5], in addition to the traditional form of the vector and scalar potentials. In the traditional form, the normal component (z-component) of the vector potential is assumed in addition to the component that is in the same direction as the dipole. Therefore, in the traditional form, the components of the vector potential Green's function due to any arbitrary dipole orientation in a layered structure stratified in z-direction can be written as

$$\bar{\mathbf{G}}^{\mathbf{A}} = (\hat{x}\hat{x} + \hat{y}\hat{y})G^A_{xx} + \hat{z}\hat{x}G^A_{zx} + \hat{z}\hat{y}G^A_{zy} + \hat{z}\hat{z}G^A_{zz} \tag{2.10}$$

where G^A_{ij} is i-component of the vector potential due to the dipole in j-direction. As the result of the selection above, i.e., the traditional form, the horizontal dipoles are assumed to result in two components of the vector potentials (e.g. G^A_{xx} and G^A_{zx} for x-directed dipole), whereas the vertical dipoles ought to yield only one component of the vector potential (e.g. G^A_{zz} for z-directed dipole) to describe the electromagnetic fields everywhere in the layered medium. Moreover, the scalar potentials due to a vertical dipole and horizontal dipole are not the same. Therefore, one needs to define five potential functions (3 for HED or HMD and 2 for VED or VMD) in order to be able to obtain all the field components uniquely in a layered structure.

2.2.1 Spectral-Domain Green's Functions in Source Layer - Horizontal Electric Dipole (HED) and Horizontal Magnetic Dipole (HMD)

The derivation of the spectral-domain Green's functions for an HED starts with writing the longitudinal field components in an unbounded medium, with the constitutive parameters of the source region, which is assumed to be layer-i in this work with the constitutive parameters of ε_i and μ_i. Hence, by using (2.7) and (2.8), the longitudinal field components in the source layer i are obtained as [1]:

$$E_{zi} = -\frac{jIl}{4\pi\omega\varepsilon_i}\frac{\partial^2}{\partial z\partial x}\frac{e^{-jk_i r}}{r} \tag{2.11}$$

$$H_{zi} = -\frac{Il}{4\pi}\frac{\partial}{\partial y}\frac{e^{-jk_i r}}{r} \tag{2.12}$$

---

[1] Note that, throughout this work, field expressions are written for the geometry shown in Fig. 2.8, where the source is always at the origin, i.e., $\mathbf{r}' = 0$. The author believes that this convention is better suited for layered media when writing the field expressions in any layer of the structure.

As stated earlier, the spherical wave term ($e^{-jk_i r}/r$) in both expressions needs to be expanded in terms of plane waves, in order to account for the reflections and transmissions at the boundaries. This can simply be achieved by using the Weyl identity 2.9) in (2.11) and (2.12), resulting in the following longitudinal field components:

$$E_{zi} = \frac{\pm Il}{8\pi^2 \omega \varepsilon_i} \int_{-\infty}^{\infty} \int_{-\infty}^{\infty} dk_x dk_y k_x e^{-jk_x x - jk_y y} e^{-jk_{zi}|z|} \tag{2.13}$$

$$H_{zi} = \frac{Il}{8\pi^2} \int_{-\infty}^{\infty} \int_{-\infty}^{\infty} dk_x dk_y k_y e^{-jk_x x - jk_y y} \frac{e^{-jk_{zi}|z|}}{k_{zi}} \tag{2.14}$$

where the ± sign is due to the derivative of $e^{-jk_{zi}|z|}$ with respect to z variable: + sign for $z > 0$ and − sign for $z < 0$. It may be necessary to emphasize the following facts one more time: i) k_x and k_y are equal in all layers due to the phase matching condition at the boundaries; ii) $e^{-j(k_x x + k_y y)}$ is considered to be the kernel of the 2D inverse Fourier transform; and therefore, iii) the rest of the terms in the integrands are the Fourier transforms of the longitudinal fields generated by an HED in an unbounded medium. As a result of these observations, the spectral-domain representations of the fields can be considered as the plane waves propagating in z-direction, and working in the spectral domain requires the tracking of the longitudinal variation of the fields only. Therefore, the fields in a layered medium can be written intuitively by considering the reflected waves from the boundaries as follows:

$$E_{zi} = \frac{Il}{8\pi^2 \omega \varepsilon_i} \int_{-\infty}^{\infty} \int_{-\infty}^{\infty} dk_x dk_y k_x e^{-jk_x x - jk_y y} F_{TM} \tag{2.15}$$

$$H_{zi} = \frac{Il}{8\pi^2} \int_{-\infty}^{\infty} \int_{-\infty}^{\infty} dk_x dk_y k_y \frac{e^{-jk_x x - jk_y y}}{k_{zi}} F_{TE} \tag{2.16}$$

where

$$\begin{aligned} F_{TE} &= e^{-jk_{zi}|z|} + A_h^e e^{jk_{zi}z} + C_h^e e^{-jk_{zi}z} \\ F_{TM} &= \pm e^{-jk_{zi}|z|} + B_h^e e^{jk_{zi}z} + D_h^e e^{-jk_{zi}z} \end{aligned} \tag{2.17}$$

It is intuitive because, as can be seen from the expressions in (2.17), the total fields inside the source region are written as the sum of incident wave and the reflected waves from upper and lower boundaries, modifying only the z variation. Note that once the fields due to an HED are obtained, those for an HMD can be written directly by the principle of duality: $\mathbf{E} \rightarrow \mathbf{H}$, $\mathbf{H} \rightarrow -\mathbf{E}$, $\mathbf{J} \rightarrow \mathbf{M}$, $\mathbf{M} \rightarrow -\mathbf{J}$, $\varepsilon \rightarrow \mu$, $\mu \rightarrow \varepsilon$, leading to the replacement of $Il \rightarrow -j\omega\mu IA$, where A is the area of the current loop modeling the magnetic dipole.

After having obtained the longitudinal field components E_{zi} and H_{zi} due to an HED and HMD in layered media in terms of unknown coefficients, it is time to determine these coefficients by imposing the continuity of the fields at the two boundaries, i.e., at $z = d_i - h$ and $z = -h$. Since the details of the implementation of the boundary conditions have been well documented [6, 13], for the sake of brevity, it is not repeated here, only the unknown coefficients A, B, C and D are provided in terms of the reflection coefficients defined at the interfaces, [20]:

$$A_h^{e,m} = e^{-jk_{zi}(d_i-h)}\tilde{R}^{i,i+1}_{TE,TM}\left[e^{-jk_{zi}(d_i-h)} + \tilde{R}^{i,i-1}_{TE,TM}e^{-jk_{zi}(d_i+h)}\right]M_i^{TE,TM} \tag{2.18}$$

$$B_h^{e,m} = e^{-jk_{zi}(d_i-h)}\tilde{R}^{i,i+1}_{TM,TE}\left[e^{-jk_{zi}(d_i-h)} - \tilde{R}^{i,i-1}_{TM,TE}e^{-jk_{zi}(d_i+h)}\right]M_i^{TM,TE} \tag{2.19}$$

$$C_h^{e,m} = e^{-jk_{zi}h}\tilde{R}^{i,i-1}_{TE,TM}\left[e^{-jk_{zi}h} + \tilde{R}^{i,i+1}_{TE,TM}e^{-jk_{zi}(2d_i-h)}\right]M_i^{TE,TM} \tag{2.20}$$

$$D_h^{e,m} = e^{-jk_{zi}h}\tilde{R}^{i,i-1}_{TM,TE}\left[-e^{-jk_{zi}h} + \tilde{R}^{i,i+1}_{TM,TE}e^{-jk_{zi}(2d_i-h)}\right]M_i^{TM,TE} \tag{2.21}$$

where M_i, the generalized reflection coefficient $\tilde{R}^{j+1,j}_{TE,TM}$, and the Fresnel reflection coefficients $R^{j,j+1}_{TE,TM}$ are defined as

$$M_i^{TE,TM} = \left[1 - \tilde{R}^{i,i+1}_{TE,TM}\tilde{R}^{i,i-1}_{TE,TM}e^{-jk_{zi}2d_i}\right]^{-1} \tag{2.22}$$

$$\tilde{R}^{j+1,j}_{TE,TM} = \frac{R^{j+1,j}_{TE,TM} + \tilde{R}^{j,j-1}_{TE,TM}e^{-jk_{zj}2d_j}}{1 - R^{j,j+1}_{TE,TM}\tilde{R}^{j,j-1}_{TE,TM}e^{-jk_{zj}2d_j}} \tag{2.23}$$

$$R^{j,j+1}_{TE} = \frac{\mu_{j+1}k_{zj} - \mu_j k_{z(j+1)}}{\mu_{j+1}k_{zj} + \mu_j k_{z(j+1)}} \tag{2.24}$$

$$R^{j,j+1}_{TM} = \frac{\varepsilon_{j+1}k_{zj} - \varepsilon_j k_{z(j+1)}}{\varepsilon_{j+1}k_{zj} + \varepsilon_j k_{z(j+1)}} \tag{2.25}$$

With the knowledge of the unknown coefficients, the Green's functions for the z components of the electric and magnetic fields, when the source and the observation points are in the same layer i, can simply be deduced from (2.15-2.17) as:

$$\tilde{G}^E_{zx} = \frac{1}{2\omega\varepsilon_i}k_x\left[\pm e^{-jk_{zi}|z|} + B_h^e e^{jk_{zi}z} + D_h^e e^{-jk_{zi}z}\right] \tag{2.26}$$

$$\tilde{G}^H_{zx} = \frac{1}{2\omega\varepsilon_i}k_y\left[e^{-jk_{zi}|z|} + A_h^e e^{jk_{zi}z} + C_h^e e^{-jk_{zi}z}\right] \tag{2.27}$$

where the longitudinal propagation constant in layer-i is defined as $k_{zi} = \sqrt{k_i^2 - k_x^2 - k_y^2} = \sqrt{k_i^2 - k_\rho^2}$. It is a well-known fact that, for a layered structure stratified in z-direction (referred to as the longitudinal direction), the transverse field components can be determined from the longitudinal field components by using the following relations [13]:

$$\tilde{\mathbf{H}}_t = \frac{1}{k^2-k_z^2}\left[\frac{\partial}{\partial z}\nabla_t \tilde{H}_z + j\omega\varepsilon\nabla_t \times \hat{z}\tilde{E}_z\right] \quad (2.28)$$

$$\tilde{\mathbf{E}}_t = \frac{1}{k^2-k_z^2}\left[\frac{\partial}{\partial z}\nabla_t \tilde{E}_z - j\omega\mu\nabla_t \times \hat{z}\tilde{H}_z\right] \quad (2.29)$$

Substituting the longitudinal field components in the spectral domain, (2.15), (2.16), the following spectral-domain Green's functions for the transverse fields are obtained:

$$\tilde{G}_{xx}^{E} = \frac{-j\omega\mu_i}{2(k_i^2-k_{zi}^2)}\left[\frac{k_x^2}{k_i^2}\frac{\partial}{\partial z}F_{TM} + \frac{k_y^2}{jk_{zi}}F_{TE}\right] \quad (2.30)$$

$$\tilde{G}_{yx}^{E} = \frac{-j\omega\mu_i k_x k_y}{2(k_i^2-k_{zi}^2)}\left[\frac{1}{k_i^2}\frac{\partial}{\partial z}F_{TM} + \frac{j}{k_{zi}}F_{TE}\right] \quad (2.31)$$

$$\tilde{G}_{xx}^{H} = \frac{k_x k_y}{2(k_i^2-k_{zi}^2)}\left[F_{TM} - \frac{j}{k_{zi}}\frac{\partial}{\partial z}F_{TE}\right] \quad (2.32)$$

$$\tilde{G}_{yx}^{H} = \frac{-1}{2(k_i^2-k_{zi}^2)}\left[k_x^2 F_{TM} - \frac{jk_y^2}{k_{zi}}\frac{\partial}{\partial z}F_{TE}\right] \quad (2.33)$$

Since field Green's functions have higher order singularities than those for the potentials, because of the spatial derivatives involved in their derivations from the potentials (2.2) and (2.4), in most computational tools, the potential Green's functions are employed in the solution of the mixed-potential integral equations (MPIE) for the analysis of printed circuits. Therefore, Green's functions for potentials play crucial role in computational electromagnetics, as well as in the efficient computation of the field Green's functions. The spectral-domain expressions of the potential Green's functions can simply be obtained by remembering that $\mu\mathbf{H} = \nabla\times\mathbf{A}$ and $\mathbf{A} = \hat{x}A_x + \hat{z}A_z$, for x-directed electric dipole in layered media, and that such relations hold for the spectral representations of these quantities. As a result, one can obtain the components of the vector potential as

$$\tilde{A}_x = \frac{\mu}{jk_y}\tilde{H}_z \quad (2.34)$$

$$\tilde{A}_z = -\frac{\mu}{jk_y}\tilde{H}_x \quad (2.35)$$

where the derivatives with respect to one of the transverse directions, x and y, are implemented in the spectral domain simply by using $\partial/\partial x = -jk_x$ and $\partial/\partial y = -jk_y$, as k_x and k_y are unique in the entire structure due to the phase-matching condition. Hence, the components of Green's function of the vector potential due to x-directed dipole are obtained as

$$\begin{aligned}\tilde{G}_{xx}^{A} &= \frac{\mu_i}{j2k_{zi}}\left[e^{-jk_{zi}|z|}+A_h^e e^{jk_{zi}z}+C_h^e e^{-jk_{zi}z}\right] &(2.36)\\ \tilde{G}_{zx}^{A} &= \frac{-\mu_i}{j2k_{zi}}\left[\frac{k_x k_{zi}}{k_\rho^2}\left(A_h^e+B_h^e\right)e^{jk_{zi}z}+\frac{k_x k_{zi}}{k_\rho^2}\left(D_h^e-C_h^e\right)e^{-jk_{zi}z}\right] &(2.37)\end{aligned}$$

Then, the Green's function for the scalar potential due to an HED can be obtained by substituting the components of the vector potential Green's functions into the Lorentz gauge (2.3), which results in

$$\tilde{G}_x^q=\frac{1}{j2\varepsilon_i k_{zi}}\left[e^{-jk_{zi}|z|}+\frac{k_{zi}^2 B_h^e+k_i^2 A_h^e}{k_\rho^2}e^{jk_{zi}z}+\frac{k_i^2 C_h^e-k_{zi}^2 D_h^e}{k_\rho^2}e^{-jk_{zi}z}\right] \tag{2.38}$$

It should be stated one more time that the Green's functions corresponding to an HMD can be obtained from those of an HED by applying the principle of duality, as noted earlier in this section.

2.2.2 Spectral-Domain Green's Functions in Source Layer - Vertical Electric Dipole (VED) and Vertical Magnetic Dipole (VMD)

Similar to the derivation of the Green's functions due to an HED source in layered media, the derivation of Green's functions for a VED starts with writing the longitudinal field components in an unbounded medium, with the constitutive parameters of the source layer-i, as

$$\begin{aligned}E_{zi} &= -\frac{jIl\omega\mu_i}{4\pi k_i^2}\left(k_i^2+\frac{\partial^2}{\partial z^2}\right)\frac{e^{-jk_i r}}{r} &(2.39)\\ H_{zi} &= 0 &(2.40)\end{aligned}$$

where it is observed that the magnetic field has only the transverse components. Because of this, VED source is known to be the source of only TM waves, while VMD source, whose longitudinal electric field is zero as can simply be deduced from the dual of the fields of VED, (2.39) and (2.40), can only excite TE waves. Then, the spherical wave part of the field, $e^{-jk_i r}/r$, are expressed as an integral sum of the plane waves using the Weyl identity (2.9) as

$$E_{zi}=\frac{-Il}{8\pi^2\omega\varepsilon_i}\int_{-\infty}^{\infty}\int_{-\infty}^{\infty}dk_x dk_y\left(k_i^2+\frac{\partial^2}{\partial z^2}\right)e^{-jk_x x-jk_y y}e^{-jk_{zi}|z|} \tag{2.41}$$

Once the plane wave representation of the longitudinal field due to a VED are obtained in an unbounded medium, the influence of the rest of the layers on this field can be accounted for by the reflections and transmissions of the plane wave constituents of the field at the upper and lower boundaries:

$$E_{zi} = \frac{-Il}{8\pi^2\omega\varepsilon_i}\int_{-\infty}^{\infty}\int_{-\infty}^{\infty} dk_x dk_y \frac{k_\rho^2}{k_{zi}} e^{-jk_x x - jk_y y} F_{TM} \tag{2.42}$$

where

$$F_{TM} = e^{-jk_{zi}|z|} + A_v^e e^{-jk_{zi}z} + B_v^e e^{jk_{zi}z} \tag{2.43}$$

As before, the unknown coefficients A and B can be obtained by imposing the boundary conditions at the upper and lower interfaces, resulting in

$$\begin{aligned} A_v^{e,m} &= e^{-jk_{zi}h}\tilde{R}_{TM,TE}^{i,i-1}\left[e^{-jk_{zi}h} + \tilde{R}_{TM,TE}^{i,i+1}e^{-jk_{zi}(2d_i-h)}\right]M_i^{TM,TE} & (2.44)\\ B_v^{e,m} &= e^{-jk_{zi}(d_i-h)}\tilde{R}_{TM,TE}^{i,i+1}\left[e^{-jk_{zi}(d_i-h)} + \tilde{R}_{TM,TE}^{i,i-1}e^{-jk_{zi}(d_i+h)}\right]M_i^{TM,TE} & (2.45)\end{aligned}$$

Hence, by using the equations that relate the longitudinal field components to transverse components (2.29), the following field Green's functions are obtained:

$$\begin{aligned} \tilde{G}_{xz}^E &= \frac{jk_x}{2\omega\varepsilon k_{zi}}\frac{\partial}{\partial z}F_{TM} & (2.46)\\ \tilde{G}_{yz}^E &= \frac{jk_y}{2\omega\varepsilon k_{zi}}\frac{\partial}{\partial z}F_{TM} & (2.47)\\ \tilde{G}_{xz}^H &= -\frac{k_y}{2k_{zi}}F_{TM} & (2.48)\\ \tilde{G}_{yz}^H &= \frac{k_x}{2k_{zi}}F_{TM} & (2.49)\end{aligned}$$

Finally, following the same procedure as in the case of HED and HMD, the potential Green's functions are obtained as

$$\begin{aligned} \tilde{G}_{zz}^A &= \frac{\mu_i}{j2k_{zi}}\left[e^{-jk_{zi}|z|} + A_v^e e^{-jk_{zi}z} + B_v^e e^{jk_{zi}z}\right] & (2.50)\\ \tilde{G}_z^q &= \frac{1}{j2k_{zi}\varepsilon_i}\left[e^{-jk_{zi}|z|} + C_v^e e^{-jk_{zi}z} + D_v^e e^{jk_{zi}z}\right] & (2.51)\end{aligned}$$

where the coefficients A and B are given in 2.44 and 2.45, respectively, and the coefficients C and D are obtained as:

$$\begin{aligned} C_v^{e,m} &= e^{-jk_{zi}h}\tilde{R}_{TM,TE}^{i,i-1}\left[-e^{-jk_{zi}h} + \tilde{R}_{TM,TE}^{i,i+1}e^{-jk_{zi}(2d_i-h)}\right]M_i^{TM,TE} & (2.52)\\ D_v^{e,m} &= e^{-jk_{zi}(d_i-h)}\tilde{R}_{TM,TE}^{i,i+1}\left[-e^{-jk_{zi}(d_i-h)} + \tilde{R}_{TM,TE}^{i,i-1}e^{-jk_{zi}(d_i+h)}\right]M_i^{TM,TE} & (2.53)\end{aligned}$$

where M and the generalized and Fresnel's reflection coefficients are given in (2.22), (2.23) and (2.24-2.25), respectively.

Note that, in all the derivations in this section, the source and observation points are assumed to be in the same layer, namely, layer-i, and because of this, the spectral-domain representations of the Green's functions consist of a direct-wave term ($e^{-jk_{zi}|z|}$), and two reflected-wave terms (one from upper boundary and the other from lower boundary of the source layer), except for the components of the Green's functions that exist only because of the interface, like $\tilde{G}^A_{zx}$. However, in the case of a different observation layer from the source layer, the direct term in the source layer needs to be combined with one of the reflected-wave terms in order to find the amplitude of the incident wave at one of the boundaries. Then, one needs to define a transfer function to find the amplitudes of the up- and down-going waves in the observation layer. These issues will be discussed in details in the following section.

2.2.3 Spectral-Domain Green's Functions - Observation Layer Different from Source Layer

As reminded in the previous section, in cases of different source and observation layers, a transfer function needs to be devised to take care of the crossing of the waves from one layer to another. Naturally, this process has to start from the source layer, as the amplitude of the incident wave from a point source can be uniquely defined. However, in order to facilitate the derivation, it would be nice to introduce a generic field expression in an arbitrary layer in terms of up- and down going waves. For this purpose, let the TE-mode field distribution in region-(j) of Fig. 2.8 be written as follows (where $j = i - m$):

$$G^{TE}_j(z) = A^-_j \left(e^{jk_{zj}z} + \tilde{R}^{j,j-1}_{TE} e^{-jk_{zj}z} e^{jk_{zj}2(-z_{-m}-h)} \right) \tag{2.54}$$

where A^-_j is the amplitude of the down-going wave in layer-j. Likewise, the field distribution of the same mode in region-($j+1$) is also written as:

$$G^{TE}_{(j+1)}(z) = A^-_{j+1} \left(e^{jk_{z(j+1)}z} + \tilde{R}^{j+1,j}_{TE} e^{-jk_{z(j+1)}z} e^{jk_{z(j+1)}2(-z_{-m+1}-h)} \right) \tag{2.55}$$

Since these field representations are the steady-state distributions in the corresponding layers, the down-going waves in region-j can be accounted for by the transmission of the down-going waves in region-$j+1$ and the reflection of the up-going waves in region-j, which is written at the interface between layer-$(j+1)$ and layer-(j), i.e. at $z = -m+1-h$, as

$$\begin{aligned} \underbrace{A_j^- e^{jk_{zj}(-z_{-m+1}-h)}}_{\text{Down-going wave in region-}(j)} &= \underbrace{T_{TE}^{j+1,j} A_{j+1}^- e^{jk_{zj}(-z_{-m+1}-h)}}_{\text{The transmitted wave from region-}(j+1)\text{ to region-j}} \\ &+ \underbrace{A_j^- \tilde{R}_{TE}^{j,j-1} e^{-jk_{zj}(-z_{-m+1}-h)} e^{jk_{zj}2(-z_m-h)} \tilde{R}_{TE}^{j,j+1}}_{\text{The up-going wave in region-}(j)\text{ reflected at the boundary}} \end{aligned} \tag{2.56}$$

where $T^{k,k-1}$ is the transmission coefficient from region-(k) to region-$(k-1)$ (i.e. $T^{k,k-1} = 1 + R^{k,k-1}$). Note that the TE and TM-mode waves must be analyzed separately, since the reflection and transmission coefficients are different for the two polarizations. This can be simply done by changing the polarizations of the transmission and generalized reflection coefficients in (2.56). By solving for A_j^- in (2.56), independent of the polarization, one can obtain the following expression for the amplitude of down-going wave in region-(j) in terms of the amplitude of down-going wave in region-$(j+1)$ (where $j = i - m$)

$$A_j^- = A_{j+1}^- \frac{T^{j+1,j} e^{-j(k_{z(j+1)} - k_{z(j)})(h + z_{-m+1})}}{1 - R^{j,j+1} \tilde{R}^{j,j-1} e^{-jk_{zj}2d_j}} \tag{2.57}$$

Using the same approach, the expression for the amplitude of the up-going wave in region-(j), in terms of the amplitude of the up-going wave in region-$(j-1)$ (where $j = i + m$) is given by

$$A_j^+ = A_{j-1}^+ \frac{T^{j-1,j} e^{-j(k_{z(j-1)} - k_{z(j)})(z_{m-1} + d_i - h)}}{1 - R^{j,j-1} \tilde{R}^{j,j+1} e^{-jk_{zj}2d_j}} \tag{2.58}$$

Since the only known amplitudes are of the up-going and down-going waves in the source region, i.e. A_i^+ and A_i^-, by using the amplitude transfer functions given in (2.57) and (2.58) in an iterative fashion, starting from the source region, one can obtain the overall fields in the observation region, which is different from the source region. The amplitudes of the up and down-going waves in the source region are obtained simply by writing the fields in the source layer as a sum of up-going and down-going waves. As an example, the vector potential G_{xx}^A, as obtained in (2.37), is given in spectral domain as follows

$$\tilde{G}_{xx}^A \propto \left[e^{-jk_{zi}|z|} + A_h^e e^{jk_{zi}z} + C_h^e e^{-jk_{zi}z} \right] \tag{2.59}$$

where the coefficients A and C are given in (2.18) and (2.20), respectively. The relation in (2.59) must be written in the following form

$$A_i^+ \left[e^{-jk_{zi}z} + \tilde{R}_{TE}^{i,i+1} e^{jk_{zi}z} e^{-jk_{zi}2(d_i-h)} \right] \tag{2.60}$$

to obtain A_i^+ (amplitude of up-going wave in the source region) and

$$A_i^- \left[e^{jk_{zi}z} + \tilde{R}_{TE}^{i,i-1} e^{-jk_{zi}z} e^{-jk_{zi}2h)} \right] \tag{2.61}$$

to obtain A_i^- (amplitude of the up-going wave in the source region). Therefore, by writing (2.59) according to (2.60) and (2.61), one can obtain the amplitude of up-going and down-going waves in the source region as

$$A_i^+ = \frac{1 + \tilde{R}_{TE}^{i,i-1} e^{-jk_z 2h}}{1 - \tilde{R}_{TE}^{i,i+1} \tilde{R}_{TE}^{i,i-1} e^{-jk_{zi}2d_i}} \tag{2.62}$$

$$A_i^- = \frac{1 + \tilde{R}_{TE}^{i,i+1} e^{-jk_z 2(d_i - h)}}{1 - \tilde{R}_{TE}^{i,i+1} \tilde{R}_{TE}^{i,i-1} e^{-jk_{zi}2d_i}} \tag{2.63}$$

Starting with these values, one can determine the amplitudes of the waves in the observation region, when it is different than the source region.

2.3 A basic discussion on the transformation of Green's functions from Spectral domain to Spatial domain

In the previous section, the field and potential Green's functions are obtained for general, homogeneous and layered media, in spectral domain. As discussed at the beginning of the chapter, the spectral domain Green's functions are related to the spatial domain ones via the inverse Fourier transform, which was introduced by the Weyl identity (2.9) for EM problems. By using the Weyl identity in the general, homogeneous medium case, all the wave vectors are summed in the spectral domain, which results in a spherical wave propagating away from the source point in the spatial domain, which are shown in Figs. 2.2 - 2.7. For this case one may argue that the frequency response of the medium is 1 for all the wave number values. In the case of the layered structures, again all the wave vector components are summed, but this time, the frequency response is determined by the reflections from the boundaries, which were derived in the previous section in detail.

Another method of transforming spectral domain Green's functions into spatial domain, which is more popular in computational EM, is the "Hankel Transform" which is given by the following Sommerfeld integration [6]:

$$G = \frac{1}{4\pi} \int_{-\infty}^{\infty} dk_\rho k_\rho H_0^{(2)}(k_\rho \rho) \tilde{G}(k_\rho) \tag{2.64}$$

where G and $\tilde{G}$ are the spatial and spectral domain Green's functions, respectively and $H_0^{(2)}$ is the Hankel function of the second kind. Since the Green's functions are even in k_ρ domain, another representation of (2.64) can be obtained by using the following identities:

$$J_0(r) = \frac{1}{2}\left(H_0^{(1)}(r) + H_0^{(2)}(r)\right) \tag{2.65}$$

$$H_0^{(2)}(r) = -H_0^{(1)}(-r) \tag{2.66}$$

which results in

$$G = \frac{1}{2\pi}\int_0^\infty dk_\rho k_\rho J_0(k_\rho \rho)\tilde{G}(k_\rho) \tag{2.67}$$

where J_0 is the Bessel function. The Hankel transform can be seen as a another version of the inverse Fourier transform: in the Hankel Transform, the total field is obtained by a sum of cylindrical waves as opposed to the inverse Fourier transform, in which a plane wave expansion is used. The nature of the cylindrical waves are defined by the Hankel functions, with different directions and magnitudes, which create an orthogonal set that is able to represent all kinds of waves in layered and general, unbounded structures. The Sommerfeld integrals above are defined to be evaluated along the real axis of the complex k_ρ plane, but other paths can also be defined for such integrations [6]. A typical integration path for the Sommerfeld integral for the integration in (2.64), i.e. Sommerfeld integration path (SIP), is shown in Fig. 2.9. For the Sommerfeld integration in (2.67), the SIP shown in Fig. 2.9 can be used on the positive real k_ρ plane. It must be noted that the SIP can be deformed as long as it does not cross any of the singularities, i.e. surface wave poles (SWPs), shown as crosses on the complex k_ρ plane in Fig. 2.9.

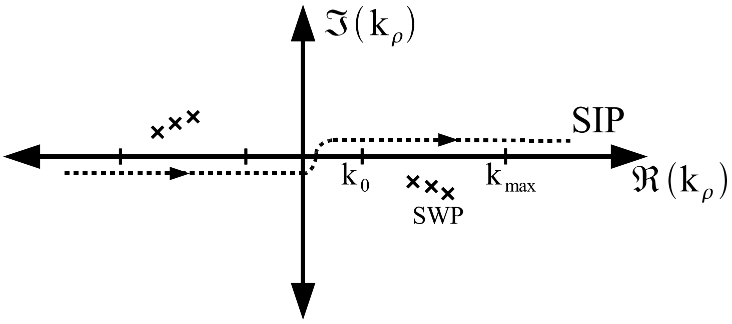

Figure 2.9: Sommerfeld integration path on the complex k_ρ plane.

The transformation in (2.64) and (2.67), i.e. the Sommerfeld integrals are difficult to evaluate, since 1) the SWPs may be close to (or on) the integration path and 2) the integrands are generally oscillatory and slowly convergent. These two problems must be analyzed separately.

2.3.1 Contributions of SWPs and physics of guided waves in layered media

In general, there are two methods to overcome the first problem, i.e. obtaining a singularity-free integrand on the integration path of the Sommerfeld integrals. The first one is as follows: subtract the singularities from the integrands by using Cauchy integration formula, integrate the remaining spectral domain Green's function to obtain the spatial domain Green's functions, without the contributions from the SWPs, and finally add the contributions of the SWPs in spatial domain, which are cylindrical waves with the wave number given by the SWP. This method can be represented mathematically as follows [19]:

$$G^{tot}(\rho) = G^{sw}(\rho) + G^{(w/o)sw}(\rho) \tag{2.68}$$

where $G^{sw}(\rho)$ is the surface wave contribution in spatial domain and given by

$$\begin{aligned} G^{sw}(\rho) &= \frac{1}{4\pi}\sum_{i=1}^{N}\int_{-\infty}^{\infty} dk_\rho k_\rho H_0^{(2)}(k_\rho\rho)\frac{2k_{\rho p(i)}(\text{Residue at } k_{\rho p(i)})}{k_\rho^2 - k_{\rho p(i)}} \\ &= \frac{-j}{2}\sum_{i=1}^{N} k_{\rho p(i)} H_0^{(2)}(k_{\rho p(i)}\rho)(\text{Residue at } k_{\rho p(i)}) \end{aligned} \tag{2.69}$$

where $k_{\rho p(i)}$ is the location of the SWP on the complex k_ρ plane and N is the number of poles. In (2.68), $G^{(w/o)sw}(\rho)$ is the spatial Green's function, without the surface wave contribution and given by:

$$G^{(w/o)sw}(\rho) = \frac{1}{4\pi}\sum_{i=1}^{N}\int_{-\infty}^{\infty} dk_\rho k_\rho H_0^{(2)}(k_\rho\rho)\left(\tilde{G}(k\rho) - \frac{2k_{\rho p(i)}(\text{Residue at } k_{\rho p(i)})}{k_\rho^2 - k_{\rho p(i)}}\right) \tag{2.70}$$

It is widely known that the real parts of SWPs [2] lie between the minimum and maximum values of the wave numbers of the differrent regions in the layered medium. The locations of the SWPs (i.e. the values of k_ρ at which the generalized reflection coefficient is ∞) on

---

[2] If there is a lossy region in the layered medium, the SWPs are complex, i.e. they have an imaginary part that describes the exponential decay along ρ direction of the surface between the different regions. If all the regions are lossless, all the SWPs are purely real.

the complex k_ρ plane can be found by using several techniques [33–36]. Here we present a complex root finding algorithm, that finds the locations of the SWPs of layered media as shown in Fig. 2.10.

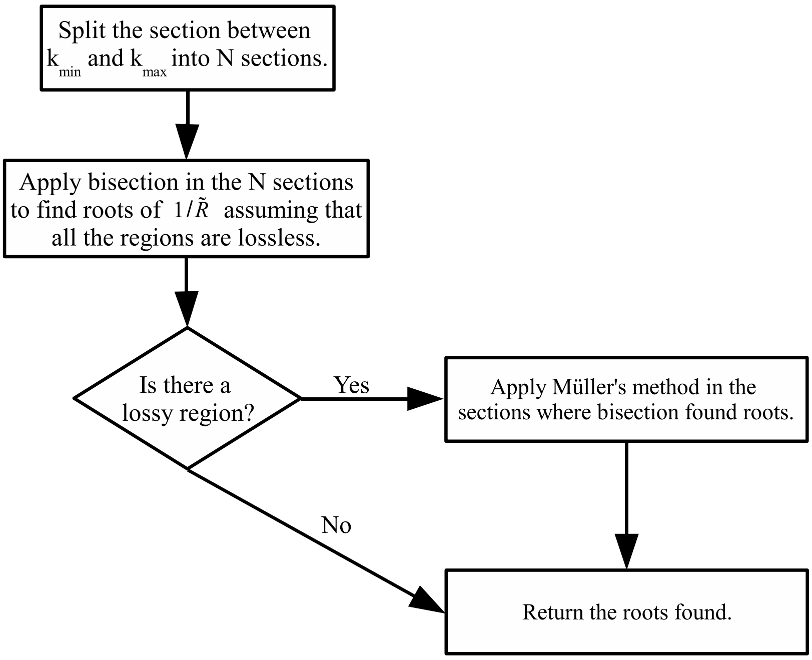

Figure 2.10: Flow chart for the complex root finding algorithm.

As can be seen in Fig.2.10, the method first finds the SWPs (roots of $1/\tilde{R}$) of the layered medium assuming that all the regions are lossless. This is done by setting the imaginary parts of the constitutive parameters of all the regions to zero. After that, if there is a lossy region in the layered medium, Müller's method is applied to determine the exact location of the pole in the complex k_ρ plane. If all the regions are lossless, the location of the SWPs found in the first step are returned. The reason for using two separate root finding algorithms is that the bisection method, even it is very cheap computationally, can only determine the roots of real valued functions, which is the case for lossless layered structures. On the other hand Müller's method can find complex roots but it is expensive computationally when compared to bisection method. Therefore in the case lossy structures, where the SWPs are complex, bisection method provides a guideline for the search location of Müller's method, since the real part of the complex SWP of the lossy structure is very close to the lossless one.

The second method to overcome the issue of singularities is deforming the SIP, so that the surface wave poles are not close to the integration path. An example of such a path deformation is shown in Fig. 2.11. As seen in Fig. 2.11, the SWPs are far away the integration path, therefore the integrand on the deformed integration path becomes smooth and in turn, a singularity-free integration can be performed.

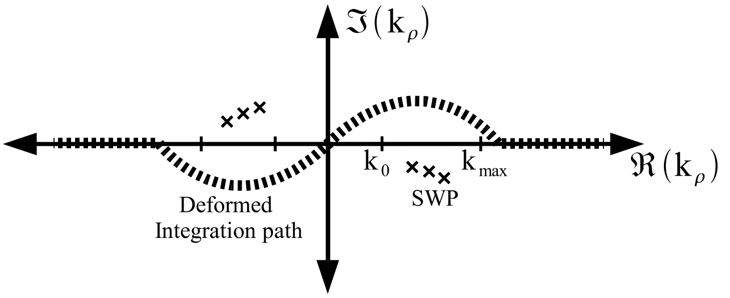

Figure 2.11: Deformed integration path on the complex k_ρ plane.

At this point, the physics of surface waves in layered structures must be introduced to understand the nature of guided waves in layered structures. The SWP is the k_ρ value that makes the denominator of the generalized reflection coefficient, (2.23), equal to 0, which makes the generalized reflection coefficient ∞, and therefore, since the generalized reflection coefficient is directly related to spectral Green's function, a singularity is observed at the location of the SWP in the spectral domain Green's function. To analyze the physics of SWP further, an example will be given here. A three layered structure as seen in Fig. 2.12 has the following TE-mode generalized reflection coefficient:

$$\tilde{R}^{3,2}_{TE} = \frac{R^{3,2}_{TE} + R^{3,1}_{TE} e^{-j2k_{z2}d}}{1 + R^{3,2}_{TE} R^{2,1}_{TE} e^{-j2k_{z2}d}} \tag{2.71}$$

As discussed above, at the location of the SWP, the denominator of the generalized reflection coefficient must be 0, i.e. the following relation must hold:

$$\begin{aligned} 1 + R^{TE}_{3,2} R^{TE}_{2,1} e^{-j2k_{z2}d} = 1 - R^{TE}_{2,3} R^{TE}_{2,1} e^{-j2k_{z2}d} = 0 \\ \Rightarrow R^{TE}_{2,3} R^{TE}_{2,1} = e^{j2k_{z2}d} \end{aligned} \tag{2.72}$$

The same behavior is also seen in Transmission Line (TL) resonators, seen in Fig. 2.13. In Fig.2.13, region-1 and region-3 of Fig. 2.12 are modelled by the impedances Z_1 and Z_3

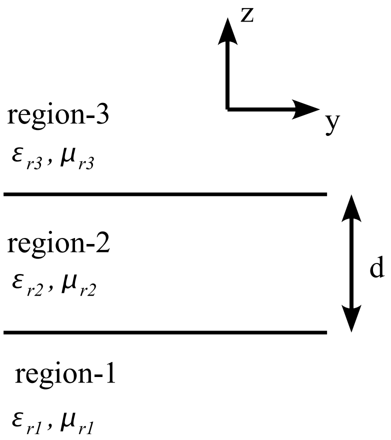

Figure 2.12: A three layered medium.

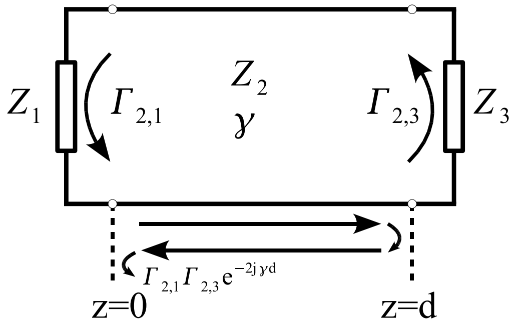

Figure 2.13: TL analogue of the layered medium seen in Fig. 2.12.

respectively. Intrinsic impedance of region-2 is modelled by the characteristic impedance of the TL (Z_1). Finally, the wave vector in z direction in region-2 is modeled by the complex propagation constant γ. From TL theory, the structure in Fig.2.13 is said to be in resonance, if the signal inside the TL is in phase with the input signal after one round-trip. Therefore the resonance condition for the structure in Fig.2.13 is given by:

$$\Gamma_{2,1}\Gamma_{2,3}e^{-j2\gamma d} = 1 \tag{2.73}$$

Note that the equations (2.72) and (2.73) are identical. Therefore one can conclude that "At the locations of surface wave poles, the layered structure is in resonance".

2.3.2 Tail extrapolation for Sommerfeld Integration

The second problem about the Sommerfeld Integrals addressed above is the slow convergence rate and highly oscillatory behavior of the integrand tails. Due to this fact, the Sommerfeld integral must be evaluated up to a very high bound value, which makes it computationally expensive, and even impossible for some cases. To overcome this fact, several series acceleration techniques are proposed [16, 37–39]. Here, we present a series acceleration method that uses the proven and most popular *integration then summation* approach [16, 40]. In the method proposed, for the Sommerfeld integration (2.67), the region between 0 and the first zero crossing of $J(k_\rho \rho)$ after the $\Re(k_{max})$ [3] value of the system is integrated directly [4] to obtain:

$$G^{k_{max}} = \int_0^{\xi_1/\rho} dk_\rho k_\rho J_0(k_\rho \rho) \tilde{G}(k_\rho) \tag{2.74}$$

where ξ_1/ρ is the first zero crossing of $J_0(k_\rho \rho)$ after the k_{max} value. Then, starting from ξ_1/ρ each section between the consecutive zeroes of $J(k_\rho \rho)$ is integrated to obtain obtain a series of which the Nth element is given by:

$$a_N = \sum_{i=1}^{N} \int_{\xi_i/\rho}^{\xi_{i+1}/\rho} dk_\rho k_\rho J_0(k_\rho \rho) \tilde{G}(k_\rho) \tag{2.75}$$

where ξ_i/ρ is the ith zero crossing of $J_0(k_\rho \rho)$ after the k_{max} value of the layered medium. Applying a Prony type exponential fitting routine (e.g. Generalized Pencil of function (GPOF) [41]) to the series of length M in (2.75) gives a set of exponentials and exponents of the form to approximate the series:

$$\sum_{n=1}^{K} b_n e^{\beta_n t} \tag{2.76}$$

where t is the sampling variable $t = 1, 2, 3...M$ and K is the number of exponentials used in the fitting, which is decided by investigating the singular value decomposition in an intermediate step of GPOF. Therefore, the result of the integration, between the first zero crossing of $J_0(k_\rho \rho)$ after k_{max} and ∞ is approximated by the coefficient b_k which is the

---

[3] Here the $\Re$ part of the k_{max} value is taken, since k_{max} is complex for lossy materials.

[4] The integration in this region can be evaluated by using any of the method described in section 2.3.1. Here the derivations are done assuming that the second approach, i.e. deforming the integration path is used.

amplitude of the exponential with the smallest exponent, i.e. $|\beta_k| \approx 0$. Therefore the result of the overall Sommerfeld integral is obtained as:

$$G(\rho) = \frac{1}{4\pi}\left(G^{k_{max}}(\rho) + G^{\infty}(\rho)\right) \tag{2.77}$$

where $G^{\infty}(\rho)$ is:

$$G^{\infty}(\rho) = b_k \qquad \text{such that } |\beta_k| \approx 0 \text{ in (2.76)} \tag{2.78}$$

To demonstrate the proposed method, a simple example is given here. A PEC backed dielectric slab shown in Fig.2.14 is analyzed at the frequency of $f = 1GHz$. The source (HED) and observation points are on the surface between the dielectric and air, with a separation of $\rho = 10cm$ between them.

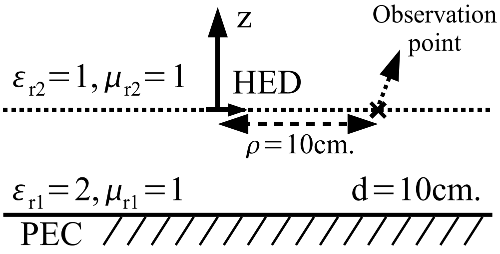

Figure 2.14: Example for the series acceleration technique proposed. ($f = 1GHz$)

The k_{max} value of this layered medium is $\sqrt{2}k_0 = 29.6192m^{-1}$. Therefore the first zero crossing of $J_0(k_\rho \rho) = J_0(0.1k_\rho)$ after the k_{max} value is obtained as $k_\rho = 55.2008m^{-1}$. (This value is the second zero crossing of $J_0(0.1k_\rho)$; the first one is at $k_\rho = 24.0483$.) The spectral domain Green's function ($\mu_0 \tilde{G}^A_{xx}(k_\rho)$), on the $\Re(k_\rho)$ axis, for the geometry in Fig.2.14 can be seen in Fig.2.15.

As seen in Fig.2.15, there is a singularity, which is a SWP found to be at $k_\rho = 22.3162m^{-1}$. In this example, the first approach given in section 2.3.1 is followed. Therefore subtracting the contribution of this pole, by using (2.69), results in a smooth integrand, as seen in Fig. 2.16. Since the SWP contribution is subtracted from the spectral domain Green's function, (2.68) must be modified such that contribution of the surface wave must be added after the numerical integration and the approximation are obtained:

$$G(\rho) = \frac{1}{4\pi}\left(G^{k_{max}}_{(w/o)swp}(\rho) + G^{\infty}_{(w/0)swp}(\rho)\right) + G^{sw}(\rho) \tag{2.79}$$

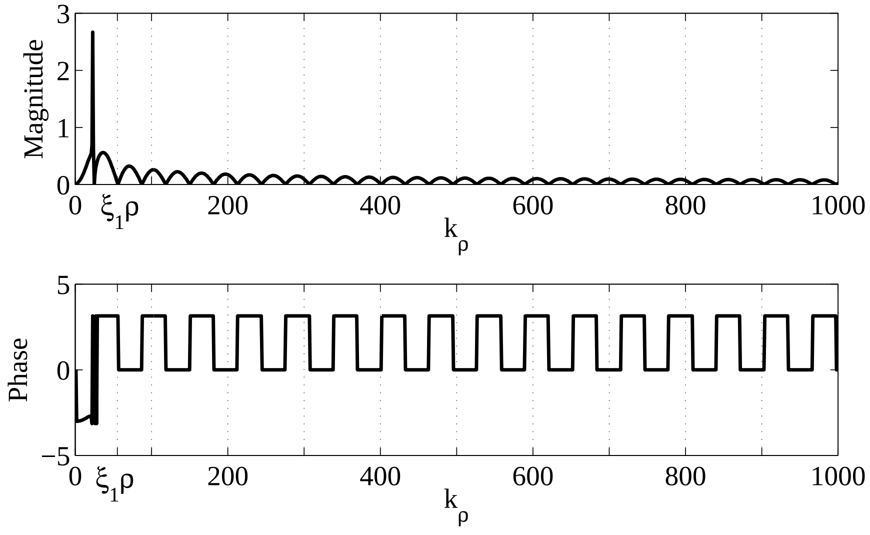

Figure 2.15: Spectral domain Green's function $(\mu_0 \tilde{G}^A_{xx}(k_\rho))$ for the geometry given in Fig. 2.14.

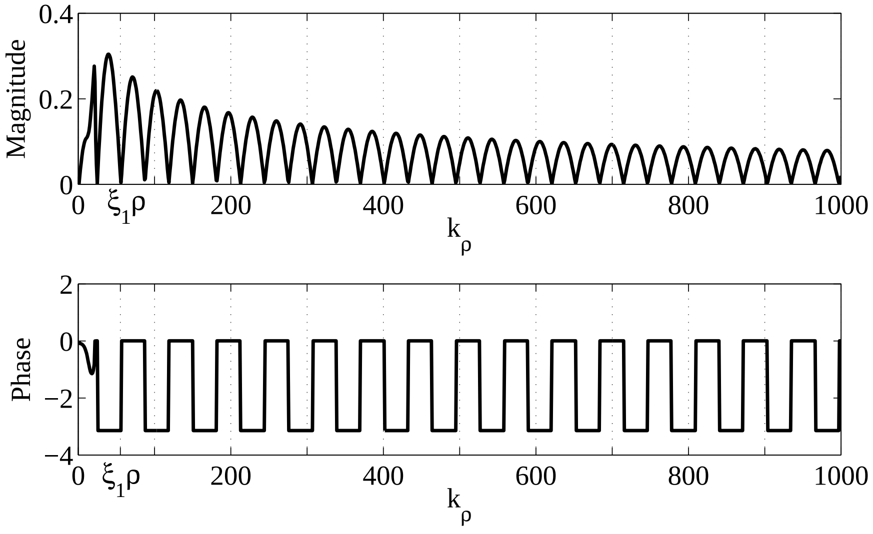

Figure 2.16: Spectral domain Green's function $(\mu_0 \tilde{G}^A_{xx}(k_\rho))$ for the geometry given in Fig. 2.14, SWP contribution subtracted.

where $G^{sw}(\rho)$ is given in (2.69) and the subscript $(w/o)swp$ means "without surface wave pole", which is discussed in (2.70). For the example shown in Fig. 2.14, the result of the GPOF, applied to the series of length 21 obtained by (2.75), are shown in Table 2.1 (thereshold value for the GPOF, i.e. the ratio of the greatest and smallest singular value used in the approximation, is set to 10^{-10}). As seen in Table 2.1, the smallest exponent is at $i = 1$, therefore the integral from $\xi_1\rho$ to ∞ can be approximated by b_1. The result of the fitting and the amplitude of the exponential with the smallest exponent, i.e. the direct term, are plotted in Fig.2.17.

By using the results, the value of the integral is found to be:

$$\begin{aligned} G(\rho) &= \frac{1}{4\pi}\left(G^{k_{max}}_{(w/o)swp}(\rho) + G^{\infty}_{(w/0)swp}(\rho)\right) + G^{sw}(\rho) \\ &= \frac{1}{4\pi}\left(\mu_0(-3.9835 - j1.6435) + \mu_0(2.6918 + j9.4995 \times 10^{-11})\right) - \mu_0(0.9792 - j0.1747) \\ &= -1.3597 \times 10^{-6} - j3.8389 \times 10^{-7} \end{aligned} \tag{2.80}$$

where $\mu_0 = 1.2566 \times 10^{-6}$. Note that $G^{k_{max}}_{(w/o)swp}(\rho)$ is obtained directly by numerical integration and $G^{sw}(\rho)$ is obtained analytically as explained above. To check the validity of the result, the same example is analyzed by using Aitken method [16] which gave $-1.3597 \times 10^{-6} - j3.8389 \times 10^{-7}$ as the result, which is the same as the result obtained by the method proposed here. In general the difference between the two methods is less than %0.01.

i	b_i	β_i
1	$2.6918 + \jmath 9.4995 \times 10^{-11}$	$-1.0202 \times 10^{-12} - \jmath 6.3175 \times 10^{-21}$
2	$0.1352 - \jmath 3.6912 \times 10^{-12}$	-1.7496+j3.1416
3	$0.8111 + \jmath 5.4924 \times 10^{-11}$	-0.0067+j3.1416
4	$0.6779 + \jmath 3.6557 \times 10^{-11}$	-0.0610+j3.1416
5	$0.4642 + \jmath 9.1844 \times 10^{-12}$	-0.1747+j3.1416
6	$0.2484 - \jmath 1.3640 \times 10^{-11}$	-0.3599+3.14156
7	$0.0203 - \jmath 1.4521 \times 10^{-11}$	-1.0644+j3.1416
8	$0.0940 - \jmath 2.1630 \times 10^{-11}$	-0.6405+j3.1416

Table 2.1: The result of the GPOF, applied to the series obtained for the example seen in Fig. 2.14

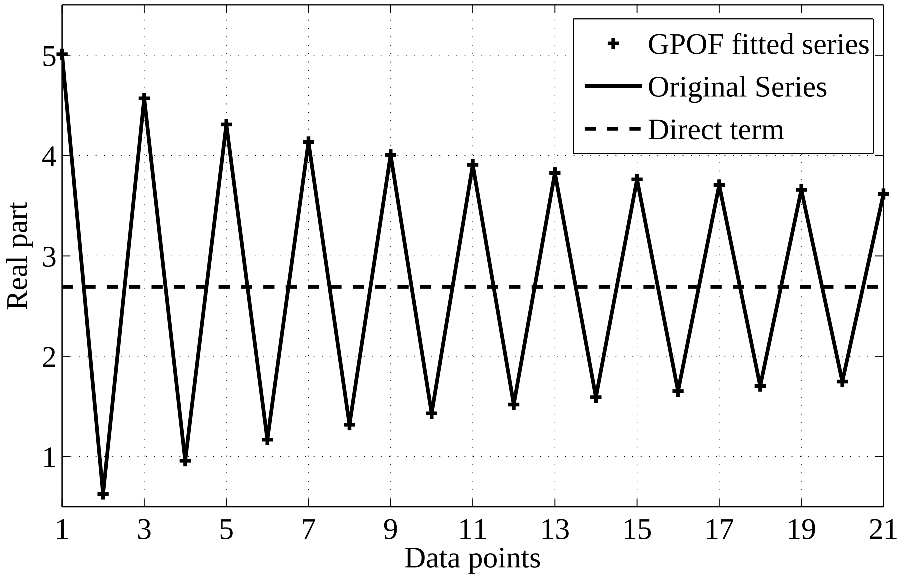

Figure 2.17: Result of the GPOF, applied to the series obtained by (2.75), for the example shown in Fig. 2.14.

Chapter 3

BASICS OF LEFT HANDED MATERIALS

Most of the materials in nature have positive real parts of permittivity (ε) and permeability (μ), therefore, from the Maxwell's equations and causality principle, they form a right handed triad of electric field ($\mathbf{E}$), magnetic field ($\mathbf{H}$) and the wave vector ($\mathbf{k}$) [13]. Due to this fact, such materials are called Right Handed Materials (RHM), when characterizing them depending on their constitutive parameters. When both of the constitutive parameters (ε and μ) have a negative real part, the three vectors $\mathbf{E}$, $\mathbf{H}$ and $\mathbf{k}$ form a left handed triad, due to which, this kind materials are called Left Handed Materials (LHM) [42–45]. Due to the difference of the propagation nature of waves in LHMs and RHMs, when an EM wave travels from RHM (or LHM) to LHM (or RHM), the transmission angle becomes negative compared to incident angle, therefore the refraction scheme between to different media is called “negative refraction”.

LHMs and the concept of negative refraction have attracted a great flurry of interest in recent years, due to their potential applications originating from building a perfect lens [46]. Although the theory of LHM was first proposed by Veselago [42], it was not popular until the realization of negative permittivity and permeability materials artificially over the same frequency band [47,48]. The structure that acts like an LHM was constructed using a periodic combination of metallic novel microstructures called “Split Ring Resonators” (SRR), to obtain negative values of μ [49] with thin wires, to obtain negative values of ε [50] simultaneously at the microwave region. Addition to such structures, several new structures were proposed that support negative refraction at the visible spectrum [51–55]. Also several constitutive parameter retrieval techniques were proposed to analyze such complex structures by using their homogeneous equivalents, with the constitutive parameters obtained [56–58]. As a result of such a huge and diverse interest on the LHMs, their behavior in layered structures became crucial as they promise potential applications, such as cloaking devices [59,60] and increasing the resolution of optical systems [46,61].

In Section 3.1, the foundations of LHMs and negative refraction will be introduced analytically and numerical results of refraction patterns of plane waves in layered media will be given. Then, in Section 3.2 an analysis will be carried out in the spectral domain, to understand the interesting behaviors observed in layered media composed of a combination of RHMs and LHMs.

3.1 Analytical analysis of Left Handed Materials

3.1.1 Analytical Foundations of LHM Physics

In [44], the sign and square root branches for the LHMs are derived with respect to $e^{-i\omega t}$ time convention. Here, the crucial steps of the derivation will be carried out with respect to $e^{j\omega t}$ time convention for sake of completeness.

In LHMs, the relative constitutive parameters satisfy:

$$\varepsilon_r = |\varepsilon_r|e^{-j\phi_\varepsilon} \qquad \text{where} \qquad \phi_\varepsilon \in \left(\frac{\pi}{2}, \pi\right] \tag{3.1}$$

$$\mu_r = |\mu_r|e^{-j\phi_\mu} \qquad \text{where} \qquad \phi_\mu \in \left(\frac{\pi}{2}, \pi\right] \tag{3.2}$$

from which one can interpret that both the real and the imaginary (if lossy) parts of the constitutive parameters are negative for LHMs. Here the definitions of the refractive index and the intrinsic impedance are important, i.e. the phase information of the following identities must be decided carefully:

$$n = |n|e^{-j\phi_n} \tag{3.3}$$

$$\eta = |\eta|e^{-j\phi_\eta} \tag{3.4}$$

which are given by the following square roots:

$$n = \sqrt{\varepsilon_r\mu_r} = \sqrt{|\varepsilon_r||\mu_r|e^{-j(\phi_\varepsilon+\phi_\mu)}} = \sqrt{|\varepsilon_r||\mu_r|}e^{-j\left(\frac{\phi_\varepsilon+\phi_\mu}{2}+l\pi\right)} \tag{3.5}$$

$$\eta = \sqrt{\frac{\mu_r}{\varepsilon_r}} = \sqrt{\frac{|\mu_r|}{|\varepsilon_r|}e^{-j(\phi_\mu-\phi_\varepsilon)}} = \sqrt{\frac{|\mu_r|}{|\varepsilon_r|}}e^{-j\left(\frac{\phi_\mu-\phi_\varepsilon}{2}+l\pi\right)} \tag{3.6}$$

As can be seen in (3.5) and (3.6), there are two possible solutions to the square roots, which are not independent of each other. These two solutions for the square roots are given by:

$$\phi_n = \frac{\phi_\varepsilon + \phi_\mu}{2} \in \left(\frac{\pi}{2}, \pi\right] \tag{3.7}$$

$$\eta_n = \frac{\phi_\mu - \phi_\varepsilon}{2} \in \left(-\frac{\pi}{4}, \frac{\pi}{4}\right] \qquad \text{for } l = 0 \tag{3.8}$$

and

$$\phi_n = \frac{\phi_\varepsilon + \phi_\mu}{2} \in \left(\frac{3\pi}{2}, 2\pi\right] \tag{3.9}$$

$$\eta_n = \frac{\phi_\mu - \phi_\varepsilon}{2} \in \left(\frac{3\pi}{4}, \frac{5\pi}{4}\right] \qquad \text{for } l = 1 \tag{3.10}$$

Equivalently, the signs of the refractive index and the intrinsic impedance are given as:

$$n = -n_r - jn_i; \qquad \eta = \eta_r \pm \eta_i \qquad \text{where } l = 0 \tag{3.11}$$

$$n = n_r + jn_i; \qquad \eta = -\eta_r \pm \eta_i \qquad \text{where } l = 1 \tag{3.12}$$

The correct choice of the square roots can be obtained by using the causality principle, which states that if $\varepsilon(\omega)$ and $\mu(\omega)$ are transformed to the time domain via the inverse Fourier transformation given by:

$$\varepsilon(t) = \frac{1}{2\pi}\int_{-\infty}^{\infty} d\omega\varepsilon(\omega)e^{j\omega t} \tag{3.13}$$

$$\mu(t) = \frac{1}{2\pi}\int_{-\infty}^{\infty} d\omega\mu(\omega)e^{j\omega t} \tag{3.14}$$

$\varepsilon(t)$ and $\mu(t)$ are strictly causal in the sense that

$$\varepsilon(t) = 0 \qquad t < 0 \tag{3.15}$$

$$\mu(t) = 0 \qquad t < 0 \tag{3.16}$$

and $\varepsilon(t)$ and $\mu(t)$ are real functions, which implies that

$$\varepsilon(-\omega) = \varepsilon^*(\omega), \;\; \mu(-\omega) = \mu^*(\omega) \qquad \text{for real } \omega \tag{3.17}$$

and $\varepsilon(\omega)$ and $\mu(\omega)$ must be analytic functions for $\Im(\omega) \leq 0$, due to the causality given by (3.15) and (3.16). Therefore the singularities of $\varepsilon(\omega)$ and $\mu(\omega)$ must lie in $\Im(\omega) > 0$. Therefore the square roots that defines the refractive index and the intrinsic impedance must be analytic in $\Im(\omega) < 0$, i.e. the branch cut introduced by the square root must be in $\Im(\omega) > 0$. Due to these facts, one finds that

$$\sqrt{\varepsilon(\omega)} = \sqrt{-|\varepsilon(\omega)|} = -j\sqrt{|\varepsilon(\omega)|} \tag{3.18}$$

$$\sqrt{\mu(\omega)} = \sqrt{-|\mu(\omega)|} = -j\sqrt{|\mu(\omega)|} \tag{3.19}$$

which corresponds to the choice given in (3.8), from which the signs of the refractive index and the intrinsic impedance are given by (3.11)

As the last step, one needs to determine the wave directions inside a LHM. Consider an x-polarized wave propagating along the z-axis:

$$\mathbf{E} = \hat{x}E_0 e^{-jkz} \tag{3.20}$$

$$\mathbf{H} = \hat{y}H_0 e^{-jkz} \tag{3.21}$$

The average Poynting's vector, i.e. the direction of power flow is given by:

$$\mathbf{S} = \frac{1}{2}(\mathbf{E} \times \mathbf{H}^*) = \hat{z}\frac{|E_0|^2}{2}\Re(\frac{1}{Z^*})e^{2k_i z} \tag{3.22}$$

where k_i is the imaginary part of wave vector $\mathbf{k} = \hat{z}nk_0$, and Z is the wave impedance ($Z = \eta Z_0$). By using the result obtained, i.e. the definitions given by (3.11), the direction of the power flow and the wave vector are found to be:

$$\mathbf{S} = \hat{z}|S| \qquad \mathbf{k} = -\hat{z}|S| \tag{3.23}$$

As seen in (3.23), the direction of the power flow is antiparallel with the direction of the wave vector, which results in a left handed triad of **E**, **H** and **k**, as discussed at the beginning of the Chapter. Also it must be noted that the exponential decay of the wave is in the same direction with the direction of power flow, as seen in (3.22), which is the physical outcome of the causality principle.

3.1.2 Numerical Examples on the Propagation of Plane Waves in LHM

Here, numerical examples that demonstrate the propagation, reflection and transmission of plane waves in LHMs are demonstrated. Before giving the results, the Snell's law must be reminded, to understand the analytical reasoning for the negative refraction. Assume that a plane wave is obliquely incident, from region-1 to region-2, on a plane dielectric boundary between them. By the Snell's law, the direction of the reflected and transmitted waves are given, in terms of the incident angle, by [62]:

$$\theta_i = \theta_r \tag{3.24}$$

$$\frac{\sin(\theta_t)}{\sin(\theta_i)} = \frac{n_1}{n_2} \tag{3.25}$$

where θ_i, θ_r and θ_t are the angles of the incident, reflected and the transmitted waves and n_1 and n_2 are the refractive indices of region-1 and region-2, respectively. By using the Snell's law one can easily show that the direction of the transmitted wave depends highly on the combinations of the signs of the refractive indices of the two different media. The resulting wave propagation patterns for the four different combinations can be seen schematically below in Fig.3.1, where the boundary between the two different regions is the plane $z = 0$.

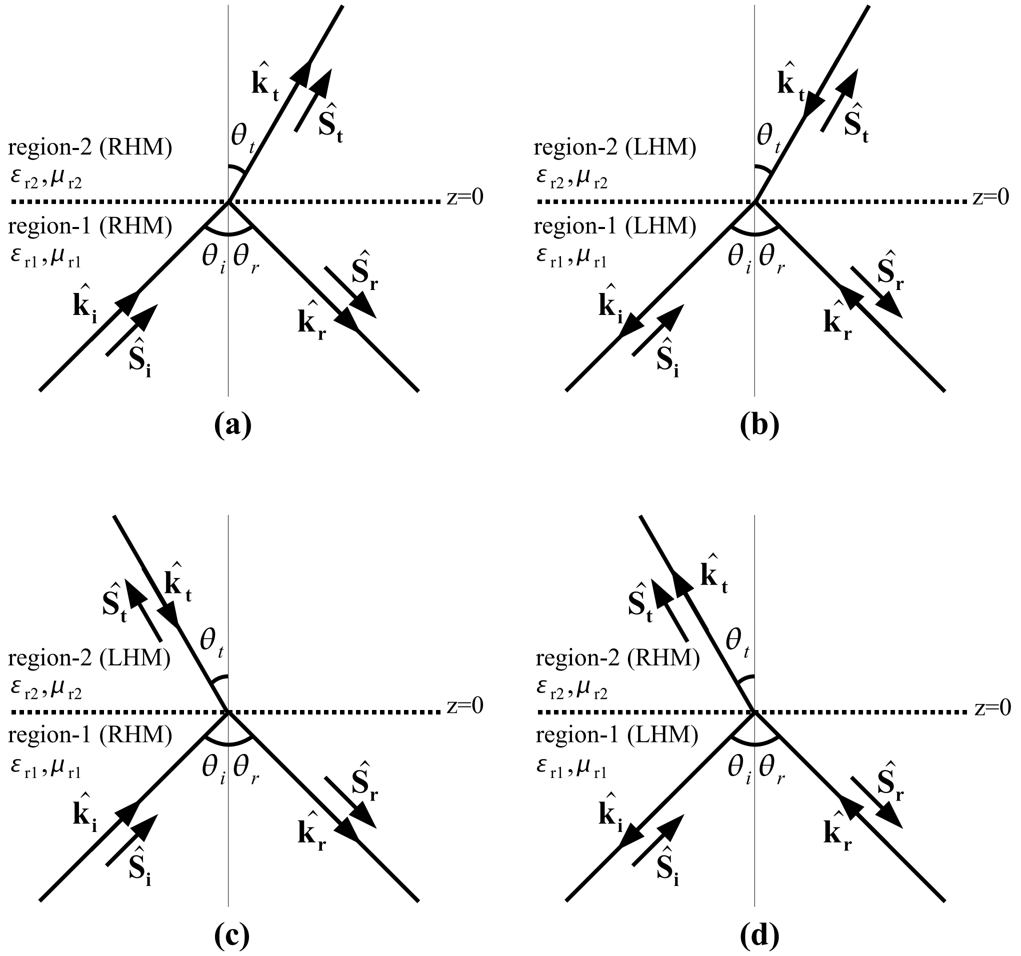

Figure 3.1: Different propagation patterns for the 4 different combinations of the media. A plane wave is sent from region-1 with the incident angle of θ_i. (a) and (b): Ordinary refraction, (c) and (d): Negative refraction.

In Fig.3.1, $\hat{\mathbf{k}}_i$, $\hat{\mathbf{k}}_r$ and $\hat{\mathbf{k}}_t$ are the directions of the incident, reflected and transmitted wave vectors, respectively and $\hat{\mathbf{S}}_i$, $\hat{\mathbf{S}}_r$ and $\hat{\mathbf{S}}_t$ are the directions of the incident, reflected and transmitted Poynting vectors, respectively. The magnitudes of the reflected and transmitted waves can be determined by using the Fresnel's Reflection coefficients given by (2.24) and (2.25). By using the fact that the z component of the wave number is given by, for example for the incident wave $k_{zi} = k_i \cos(\theta_i)$, the Fresnel's reflection coefficients have the following form:

$$R_{TE}^{j,j+1} = \frac{\mu_{r2}\cos(\theta_i)k_i - \mu_{r1}\cos(\theta_t)k_t}{\mu_{r2}\cos(\theta_i)k_i + \mu_{r1}\cos(\theta_t)k_t} \tag{3.26}$$

$$R_{TM}^{j,j+1} = \frac{\varepsilon_{r2}\cos(\theta_i)k_i - \varepsilon_{r1}\cos(\theta_t)k_t}{\varepsilon_{r2}\cos(\theta_i)k_i + \varepsilon_{r1}\cos(\theta_t)k_t} \tag{3.27}$$

All the directions of the wave vectors are shown in Fig.3.1. Also the Fresnel's transmission coefficients are determined by $T = 1 + R$. Therefore, by using these forms of the Fresnel's reflection coefficients, one can first find the directions of the wave vectors by using the Snell's law given in (3.25) and then the amplitudes of the reflected and transmitted waves are found by using the Fresnel's reflection coefficient given in (3.26) and (3.27). As can be seen, when one of the media is RHM and the other LHM, a negative refraction is observed (Fig.3.1 (c) and (d)), whereas, when both of the media is of the same kind, an ordinary refraction is observed(Fig.3.1 (a) and (b)). Since the Snell's law is valid for all kinds of materials including RHMs and LHMs, all the concepts derived from the Snell's law, (e.g. total reflection, Brewster's angle ...) can be determined by the appropriate choice of refractive index sign.

To analyze the propagation of plane waves in layered media, a code that determines the propagation pattern is written by using the amplitude transfer function discussed in Chapter 2. The code can be seen in appendix B. Below, two interesting examples are demonstrated to analyze the propagation of waves in layered media.

The Brewster's Angle

As an example, the Brewster's angle, i.e. the incidence angle at which there is no reflected wave, is determined by setting the numerator of the Fresnel's reflection coefficients (3.26) and (3.27) equal to zero, which are obtained as:

$$\theta_b^{TE} = \arcsin\left(\sqrt{\frac{1 - \mu_{r1}\varepsilon_{r2}/\mu_{r2}\varepsilon_{r1}}{1 - (\mu_{r1}/\mu_{r2})^2}}\right) \tag{3.28}$$

$$\theta_b^{TM} = \arcsin\left(\sqrt{\frac{1 - \varepsilon_{r1}\mu_{r2}/\varepsilon_{r2}\mu_{r1}}{1 - (\varepsilon_{r1}/\varepsilon_{r2})^2}}\right) \tag{3.29}$$

A numerical example is given below, at which a plane wave with unit magnitude is sent with the incident angle of the Brester's angle, where it is found to be the same for an

RHM-RHM interface and its RHM-LHM counterpart. For the RHM-RHM interface the constitutive paremeters of the different regions is $(\varepsilon_{r1} = 1, \mu_{r1} = 2, \varepsilon_{r2} = 3, \mu_{r2} = 4)$ and for the RHM-LHM interface, $(\varepsilon_{r1} = 1, \mu_{r1} = 2, \varepsilon_{r2} = -3, \mu_{r2} = -4)$. The frequency of operation is $f = 1GHz$. For these values of constitutive parameters, the Brewster's angle is found to be 37.7612 degrees for the TM case. The result obtained by the code in appendix B can be seen Fig.3.2

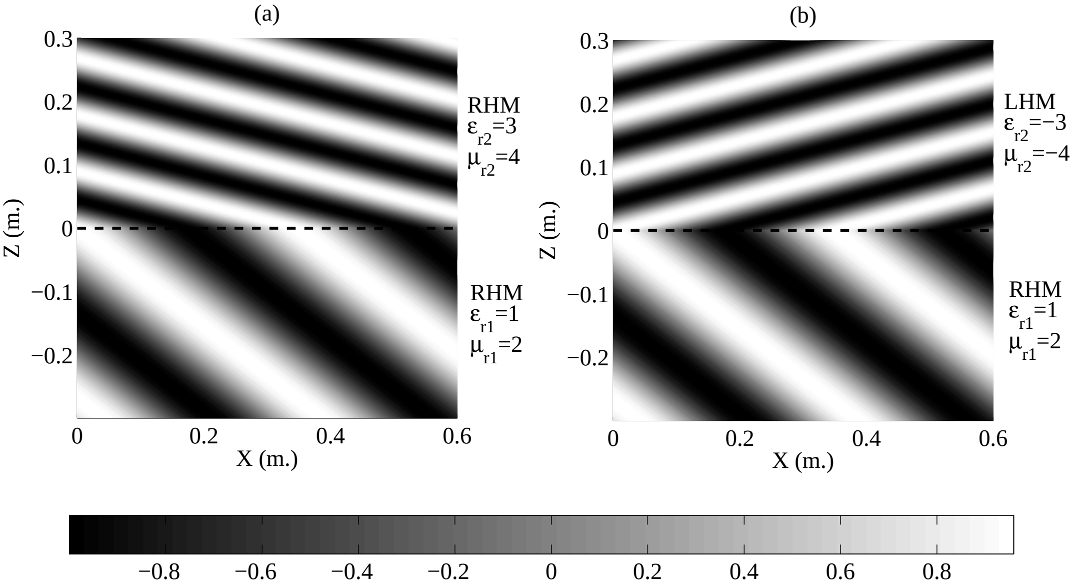

Figure 3.2: The propagation pattern of waves at Brewster's angle, 37.7612 degrees, TM-mode, $\Re$ part of H-field, y-component. (a) RHM-RHM interface, (b)RHM-LHM interface. $f = 1GHz$ for both of the simulations.

A Lossy Slab

As the second example, the propagation pattern of plane waves in a layered geometry, where a lossy material is put in air ($\varepsilon_{r1} = \varepsilon_{r3} = 1$, $\mu_{r1} = \mu_{r3} = 1$), is analyzed. To see the difference in the propagation patterns between the RHM and LHM slabs, the slab is analyzed both for an RHM slab ($\varepsilon_{r2} = 2 - j0.4$, $\mu_{r2} = 1.5 - j0.4$) and its LHM counterpart (($\varepsilon_{r2} = -2 - j0.4$, $\mu_{r2} = -1.5 - j0.4$)). The frequency of operation is $f = 1GHz$ and the incident angle is taken to be 45 degrees. The results obtained by the code in appendix B can be seen in Figs. 3.3 and 3.4, for TE and TM modes respectively.

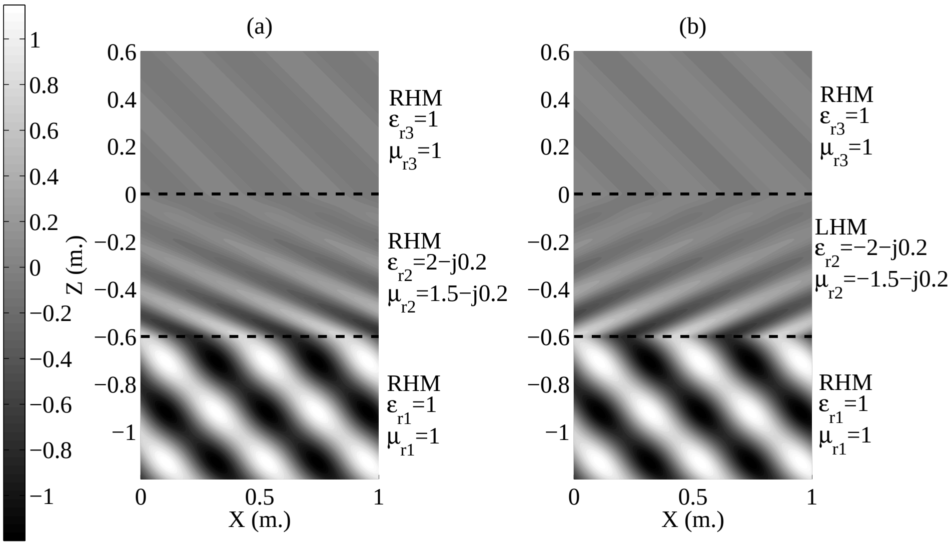

Figure 3.3: The propagation pattern of waves in a lossy slab geometry with the incident angle of 45 degrees, TE-mode, $\Re$ part of E-field, y-component. (a)RHM-RHM-RHM configuration (b)RHM-LHM-RHM configuration. $f = 1GHz$ for both of the simulations.

As can be seen in the results, the propagation patterns of the waves changes dramatically depending on the constitutive parameter combinations. As discussed in section 3.1.1, a negative refraction is observed between two different materials. But when the two materials are of the same kind, an ordinary refraction occurs.

3.2 Behavior of Left Handed Materials in Spectral Domain

As analyzed in Chapter 2 the locations of the singularities in the spectral domain Green's functions are very important, since they have a very high influence on the spatial domain, and also their exact locations must be known to make the evaluation of Sommerfeld integrals easier, or perform the Discrete Complex Image Method (DCIM), which will be discussed in Chapter 4.

In the case of layered media composed of only RHMs, it is widely known that all the singularities lie between the k_{min} and k_{max} values of the structure [63]. Also, these singularities

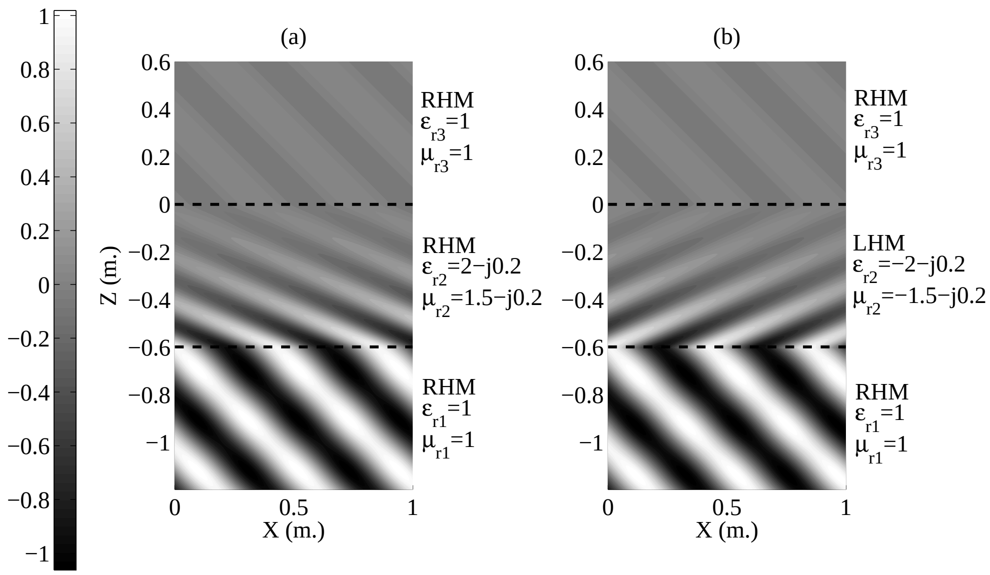

Figure 3.4: The propagation pattern of waves in a lossy slab geometry with the incident angle of 45 degrees, TM-mode, $\Re$ part of H-field, y-component. (a)RHM-RHM-RHM configuration (b)RHM-LHM-RHM configuration. $f = 1GHz$ for both of the simulations.

are because of the resonance of the layers (as discussed in Section 2.3.1), which results in a SWP in the generalized reflection coefficient. In the case of layered structures composed of a combination of RHMs and LHMs, the possible pole locations can be between k_{min} up to ∞ [64–68]. Moreover, another singularity due to the discontinuity of two different regions, i.e. Surface Plasmon-Polariton (SPP), can be observed in a RHM-LHM interface [69–74]. These two sources of singularities will be analyzed analytically and numerically in this Section.

3.2.1 Surface Wave Poles in Layered Structures containing LHMs and the Concept of Critical Thickness

For a layered geometry seen in Fig.3.5, the generalized reflection coefficient is given by:

$$\tilde{R}^{i,i+1}_{TE,TM} = \frac{R^{i,i+1}_{TE,TM} + \tilde{R}^{i+1,i+2}_{TE,TM} e^{-jk_{z(i+1)}2d_{(i+1)}}}{1 - R^{i+1,i}_{TE,TM}\tilde{R}^{i+1,i+2}_{TE,TM} e^{-jk_{z(i+1)}2d_{(i+1)}}} \tag{3.30}$$

The SWP, as discussed in Chapter 2, is the k_ρ value at which the denominator of the generalized reflection coefficient becomes zero. Therefore, at the location of the SWP, the

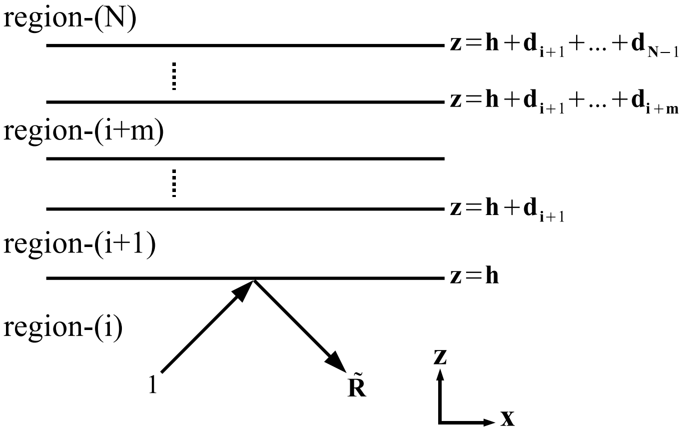

Figure 3.5: A layered geometry defining the coordinate system.

following resonance condition must hold:

$$R^{i+1,i}_{TE,TM}\tilde{R}^{i+1,i+2}_{TE,TM} = e^{jk_{z(i+1)}2d_{(i+1)}} \tag{3.31}$$

Obviously, the location of the $\Re$ part of the SWP can be on three different sections on the $\Re(k_\rho)$ axis, which are shown in Fig.3.6.

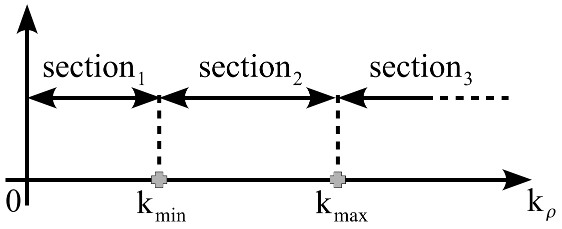

Figure 3.6: Sections on the $\Re(k_\rho)$ axis for the investigation of the SWPs.

The resonance condition given by (3.31) only checks if there is a resonance in region-$(i+1)$. But since the generalized reflection coefficient is obtained in an iterative fashion, starting with the Fresnel's reflection coefficient between the regions-$(N-1)$ and (N), if there is a resonance in any region between region-(N) and (i), it will be seen as a singularity in the generalized reflection coefficient. In other words, the resonance of a layered structure do not depend on the location of the source. In the discussion below, only the resonance condition of region-$(i+1)$ is investigated without loss of generality.

Analyzing the resonance condition, (3.31), reveals that for structures that can handle SWPs at locations greater than the k_{max} value, i.e. section$_3$ of Fig.3.6, as the thickness of the structure increases ($d_{(i+1)}$ in (3.31)), the $\Re$ part of the SWP migrates towards the k_{max} value from right. This is due to the fact that, the $\Im$ part of $k_{z(i+1)}$ must be smaller to satisfy the resonance condition for the greater $d_{(i+1)}$ values, since the change in the reflection coefficients, i.e. multiplication given by the RHS of (3.31), cannot change as rapidly as the exponential decay given by the LHS. By using this information, one can define a "*Critical Thickness*" for the slab, beyond which it is guaranteed that all the SWPs lies between the k_{min} and k_{max} values of the structure, i.e. in section$_2$ of Fig.3.6. By using this fact, at the location of the critical thickness, the SWP must be at a location very close to the k_{max} value, i.e. the following equality must hold:

$$R^{i+1,i(\sigma)}_{TE,TM}\tilde{R}^{i+1,i+2(\sigma)}_{TE,TM} = e^{jk_{z(i+1)}2d_{(i+1)}} \tag{3.32}$$

where the superscript σ of the reflection coefficients means that they are evaluated at $k_\rho = (1+\sigma)k_{max}$ with $0 < \sigma \ll 1$. Solving for $d_{(i+1)}$ gives the critical thickness value for region-$(i+1)$ as:

$$d^{TE,TM}_{crit} = \Re\left(\frac{\ln\left(R^{i+1,i(\sigma)}_{TE,TM}\tilde{R}^{i+1,i+2(\sigma)}_{TE,TM}\right)}{j2k_{z(i+1)}}\right) \tag{3.33}$$

To analyze the migration of poles as a function of the region thickness and the concept of critical thickness, a numerical example is given here. The layered media shown in Fig.3.7 is analyzed at the frequency of $f = 1GHz$. For the values of constitutive parameters,

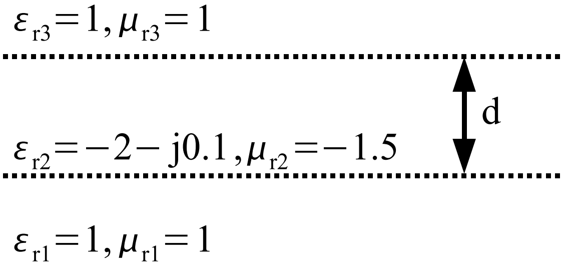

Figure 3.7: The geometry of the SWP migration example.

the critical thickness of the slab is found to be $d_{crit}^{TE} = 4.4991cm$ and $d_{crit}^{TM} = 3.3631cm$, at $\sigma = 10^{-6}$, for TE and TM-modes, respectively. The locations of SWPs are plotted in Figs.3.8, 3.9, 3.10 and 3.11 for various thicknesses of the slab.

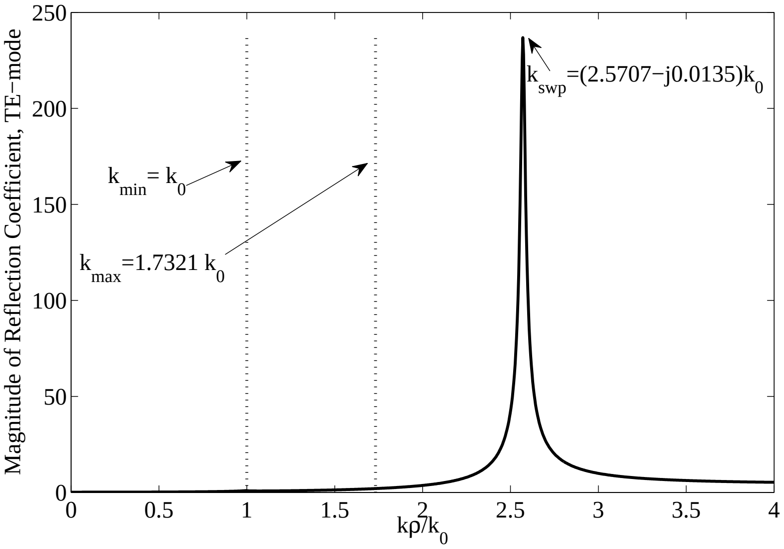

Figure 3.8: The location of the SWP at $d = 3cm$ (less than critical thickness), for the geometry shown in Fig.3.7, TE-mode. A single, positive SWP is observed.

As can be seen in the results shown in Figs.3.8, 3.9, 3.10 and 3.11, after the critical thickness value, all the SWPs lies between k_{min} and k_{max} values of the structure. Another important result that can be obtained from the figures is that there are two different kinds of SWPs in such structures. The first one is the positive SWP, which has a negative imaginary part and the second one is the negative SWP, which has a positive imaginary part. Since the surface waves cannot grow exponentially along the surface in passive media in the direction of propagation, which is defined to be positive ρ [63], the surface wave poles with positive imaginary part are not physical. Therefore, due to the even nature of the generalized reflection coefficient, their negative values must be taken which defines a surface wave with negative phase velocity, and decays exponentially in the direction of propagation. This fact is important when determining the spatial domain Green's functions, by using Sommerfeld integrals or DCIM, as will be discussed in Chapter 4.

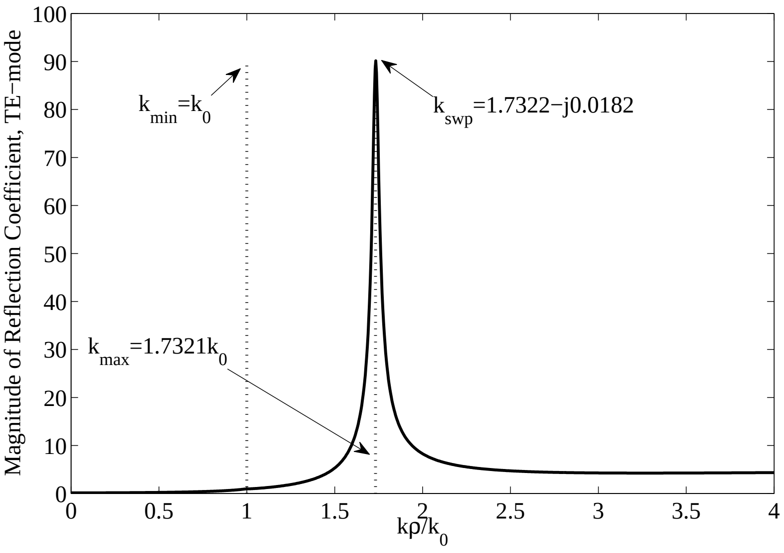

Figure 3.9: The location of the SWP at $d = 4.4991cm$ (at critical thickness), for the geometry shown in Fig.3.7, TE-mode. A single, positive SWP is observed.

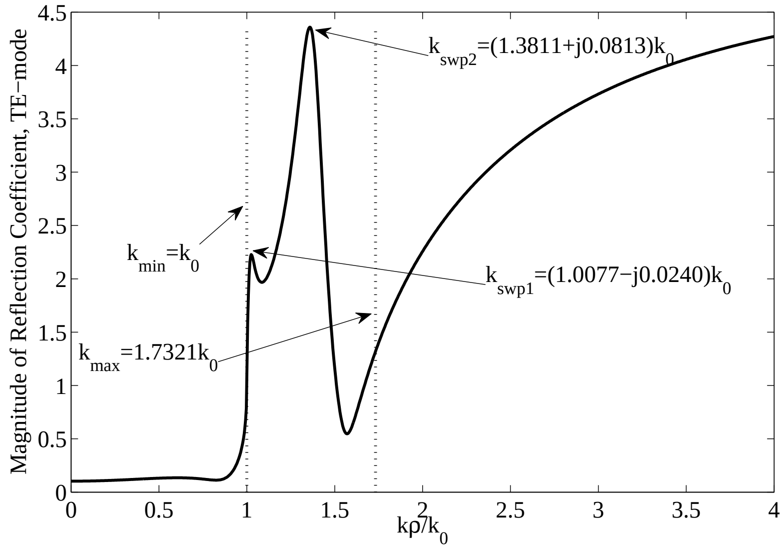

Figure 3.10: The location of the SWPs at $d = 20cm$ (greater than critical thickness), for the geometry shown in Fig.3.7, TE-mode. One positive (k_{swp1}) and one negative (k_{swp2}) SWPs are observed.

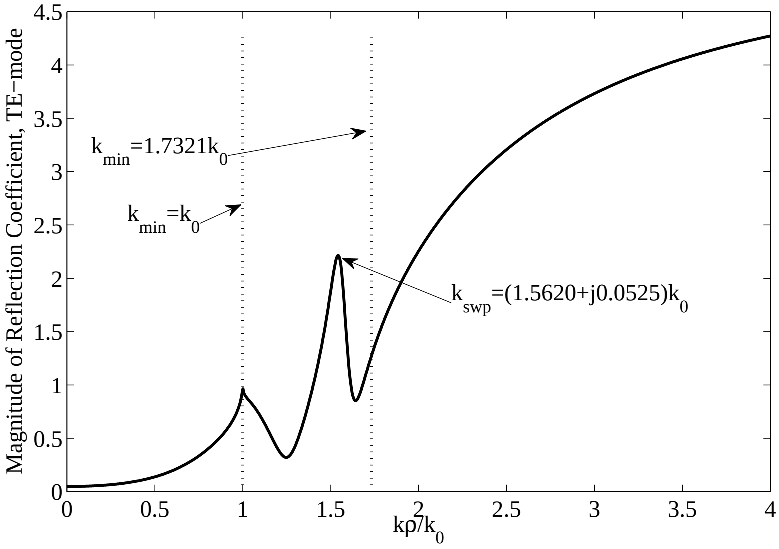

Figure 3.11: The location of the SWPs at $d = 25cm$ (greater than critical thickness), for the geometry shown in Fig.3.7, TE-mode. A single, negative SWP is observed.

3.2.2 Surface Plasmon-Polaritons in Layered Structures containing LHMs and the Concept of Threshold Thickness

The surface plasmon polariton is the kind of surface wave that is generated due to the discontinuity at the interface of two different materials. Unlike the case of SWPs, SPPs can be generated in a two layered geometry as seen in Fig.3.12. SPPs decay inside both of the regions exponentially (z component of the wave vectors in both of the media is purely imaginary (for lossless materials) or have a very small real part (for lossy materials)), and

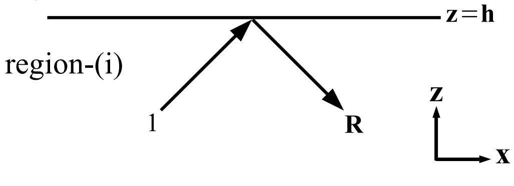

Figure 3.12: A two layered geometry defining the coordinate system.

due to this fact they are always in section$_3$ of Fig.3.6. Mathematically, the SPP wave vector is obtained from the pole of the Fresnel's reflection coefficient, which is given by:

$$R_{TE}^{i,i+1} = \frac{\mu_{i+1}k_{zi} - \mu_i k_{z(i+1)}}{\mu_{i+1}k_{zi} + \mu_i k_{z(i+1)}} \tag{3.34}$$

$$R_{TM}^{i,i+1} = \frac{\varepsilon_{i+1}k_{zi} - \varepsilon_i k_{z(i+1)}}{\varepsilon_{i+1}k_{zi} + \varepsilon_i k_{z(i+1)}} \tag{3.35}$$

therefore at the location of the SPP pole the following equality must hold:

$$\mu_{i+1}k_{zi} = -\mu_i k_{z(i+1)} \qquad \text{for TE-mode} \tag{3.36}$$

$$\varepsilon_{i+1}k_{zi} = -\varepsilon_i k_{z(i+1)} \qquad \text{for TM-mode} \tag{3.37}$$

By solving for k_ρ in the relations (3.36) and (3.37), the location of the SPP pole is given by:

$$k_{sp}^{TE} = k_0\sqrt{\frac{\mu_{ri}\mu_{r(i+1)}\big(\mu_{r(i+1)}\varepsilon_{ri} - \mu_{ri}\varepsilon_{r(i+1)}\big)}{\mu_{r(i+1)}^2 - \mu_{ri}^2}} \qquad \text{for TE-mode} \tag{3.38}$$

$$k_{sp}^{TM} = k_0\sqrt{\frac{\varepsilon_{ri}\varepsilon_{r(i+1)}\big(\varepsilon_{r(i+1)}\mu_{ri} - \varepsilon_{ri}\mu_{r(i+1)}\big)}{\varepsilon_{r(i+1)}^2 - \varepsilon_{ri}^2}} \qquad \text{for TM-mode} \tag{3.39}$$

The regions where the 2-layered structure shown in Fig.3.12 can handle SPPs in TE-mode are plotted in Fig.3.13 [71]. By using the duality principle, the chart for the TM-mode can be simply obtained by interchanging the ε values with μ values.

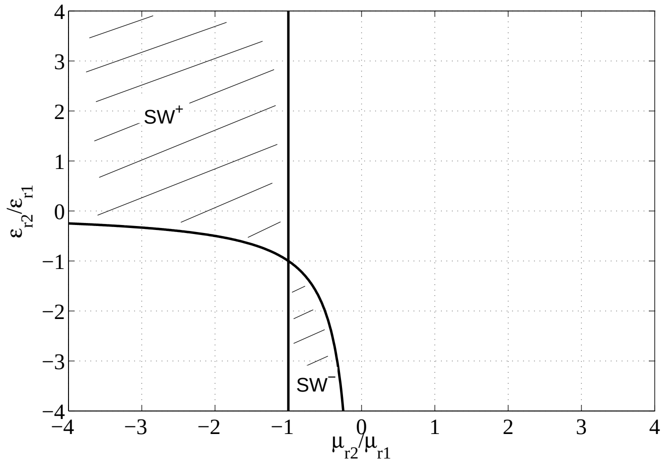

Figure 3.13: The combinations of the constitutive parameters of the 2-layered structure shown in Fig.3.12, TE-mode. In the region shown with SW^-, SPPs with negative wave numbers are generated, whereas, in the region shown with SW^+, SPPs with positive wave numbers are generated.

The SPPs can also seen as singularities of the generalized reflection coefficient in a multilayered structure, as seen in Fig.3.5. From a simple comparison of the generalized and Fresnel's reflection coefficients ((3.30) and (3.34) or (3.35)), it is obvious that the locations of the SPP wave vectors would be different. However, for large thicknesses of region-$(i+1)$, the generalized reflection coefficient converges to Fresnel's reflection coefficient as the second terms, both in the numerator and denominator of the generalized reflection coefficient, tend to zero exponentially due to the loss in the slab (since the wave number of SPP is greater than the wave number of region-$(i+1)$[1]); and, as a result, in the limit $d_{(i+1)} \rightarrow \infty$, the locations of SPP wave vectors of the layered structure converges to the analytically obtained SPP pole location for the two-layer structure, i.e. (3.38) or (3.39). Using this information, one can define a threshold thickness, beyond which the analytical SPP wave vector can be used with negligible error for the layered configuration. At the the threshold thickness value, Fresnel's and generalized reflection coefficients must be approximately equal to each other, at a location near the SPP wave number, i.e. the following inequalities must hold simultaneously:

$$\begin{aligned} \frac{\left|\tilde{R}^{i+1,i+2}_{TE,TM}\right| e^{\Im(k_{z(i+1)})2d^{TE,TM}_{thr}}}{\left|R^{i,i+1}_{TE,TM}\right|} &\leq \sigma \\ \left|R^{i+1,i}_{TE,TM}\right| \left|\tilde{R}^{i+1,i+2}_{TE,TM}\right| e^{\Im(k_{z(i+1)})2d^{TE,TM}_{thr}} &\leq \sigma \end{aligned} \tag{3.40}$$

where $0 < \sigma \ll 1$. Using (3.40), the threshold thickness value (the maximum value of d_{thr}, such that both of the inequalities are satisfied) is obtained as:

$$d^{TE,TM}_{thr} = \max\left(\frac{\left| ln\left(\frac{\sigma|R^{i,i+1}_{TE,TM}|}{|\tilde{R}^{i+1,i+2}_{TE,TM}|} \right) \right|}{|2\Im\left(k_{z(i+1)}\right)|}, \frac{\left| ln\left(\frac{\sigma}{|R^{i,i+1}_{TE,TM}||\tilde{R}^{i+1,i+2}_{TE,TM}|} \right) \right|}{|2\Im\left(k_{z2}\right)|} \right) \tag{3.41}$$

In (3.41), the Fresnel's and generalized reflection coefficients are evaluated not at $k_\rho = k_{sp}$, where they may be singular, but in a near vicinity like $k_\rho = (1+\sigma)k_{sp}$. Therefore, (3.41) guarantees that the analytical expressions (3.38) or (3.39), can be used as the SPP wave vector for the layered structure, with a region-$(i+1)$ thickness greater than the threshold thickness value, with a negligible error given by σ. It is obvious that (3.41) is derived given

---

[1] Here the same approach that was used to analyze the thickness dependence of SWPs (the only region under consideration is region-$(i+1)$ of Fig.3.5) is used to analyze locations of SPP wave vectors in layered structures, without loss of generality.

that the observation layer is region-i, therefore the interface between region-i and $(i+1)$ must support SPPs for the given polarization to be able to use (3.41). If the interface between region-(i) and $(i+1)$ does not support SPPs, a threshold thickness value can be obtained by changing the observation layer to region-$(i+2)$ (i.e. defining the generalized reflection coefficient from region-$(i+2)$ to region-$(i+1)$) under the condition that the interface between region-$(i+1)$ and $(i+2)$ supports SPPs.

To analyze the migration of SPPs depending on thickness values in layered structures, several examples of three layered structures, shown in Fig.3.14, those handle SPPs are given here.

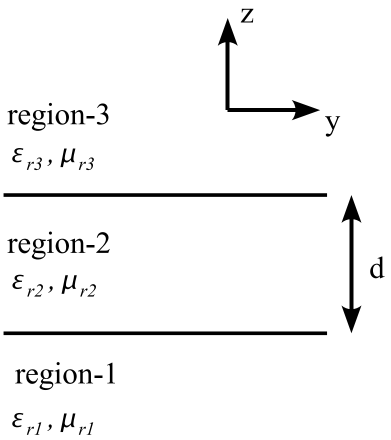

Figure 3.14: The three layered geometry used to analyze the thickness dependent behavior of SPPs.

Metallic Slab, TM mode SPP

Thickness dependent behavior of the SPP wave vectors in a metal slab, with constitutive parameters of $\varepsilon_{r2} = -33.22 - j1.17$ and $\mu_{r2} = 1$ is studied at $\lambda_0 = 852nm$ for two different configurations of the surrounding media: (i) region-1 and -3 are free-space, and (ii) region-1 and -3 are different dielectric materials with $\varepsilon_{r1} = 2$, $\mu_{r1} = 1$ and free-space respectively. Since only the permittivity value of metals has a negative real part, only TM waves can generate SPPs in such structures. By (3.39), the SPP wave vectors for the two layered semi-infinite structures are found to be $k_{sp} = (1.0154 - j0.0006)k_0$ and $k_{sp} = (1.4587 - j0.0016)k_0$

for configuration (i) and (ii), respectively, where $k_0 = (2\pi/\lambda_0)$ is the free-space wavenumber. For the two configurations, the threshold thickness values are obtained from (3.41), TM mode, as $175.5nm$ and $137.5nm$ for configuration (i) and (ii) respectively with $\sigma = 10^{-3}$. The locations of the SPP wave vectors are shown in Figs.3.15 and 3.16 for two different thicknesses of the metal slab in each configuration, one below and the other above the threshold thickness values. As seen in Figs.3.15 and 3.16, for two different slab configurations, there are two SPP wave vectors for the thickness less than the corresponding threshold thickness values. For configuration (i), Fig.3.15, both of the SPP wave vectors are observed as singularities of the generalized reflection coefficient ($k_{sp1} = (1.0007 - j2.16 \times 10^{-6})k_0$ which corresponds to long range SPP and $k_{sp2} = (1.2983 - j0.0183)k_0$ which corresponds to short range SPP [75]), whereas in configuration (ii), Fig.3.16, one of the SPP wave vectors is seen as a singularity ($k_{sp2} = 1.4803 - j0.0037$) and the other is observed as a dip in the reflection coefficient. This is due to the fact that the SPP pole at the metal-air (between region-2 and resion-3) is less than the wavenumber of region-1, which makes it possible for

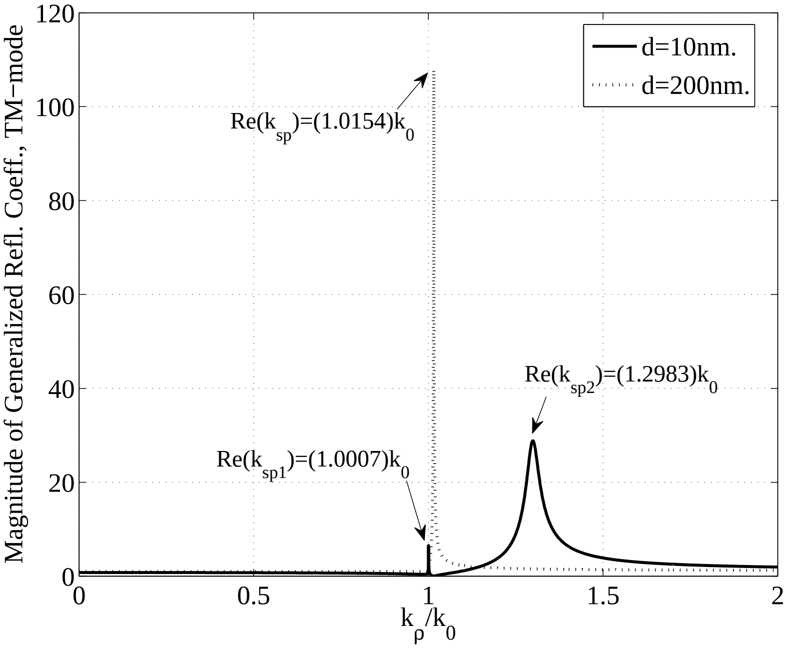

Figure 3.15: SPP poles of the metal slab for different thicknesses, observation layer: region-1. region-2 is metal with $\varepsilon_{r2} = -33.22 - 1.17j$, $\mu_{r2} = 1$, and the thickness d. region-1 and region-3 are free-space.

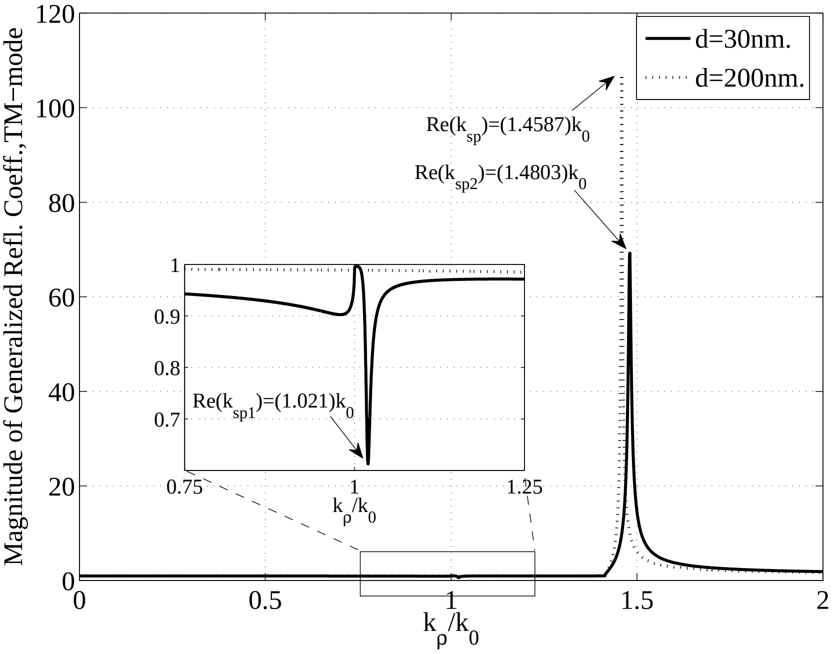

Figure 3.16: SPP poles of the metal slab for different thicknesses, observation layer: region-1. region-2 is metal with $\varepsilon_{r2} = -33.22 - 1.17j$, $\mu_{r2} = 1$, and the thickness d. region-1 is a dielectric material with $\varepsilon_{r1} = 2$, $\mu_{r1} = 1$, and region-3 is free-space.

an incident radiating wave in region-1 to excite SPP at the metal-air interface, thus resulting in a dip on the reflection coefficient plot at $k_\rho = k_{sp1}$, as shown in the inset of Fig.3.16. However for configuration (i), since both of the SPP poles are greater than the wave number of region-1, they could only be excited by the evanescent waves at the dielectric-metal interface, resulting in pole singularities on the generalized reflection coefficient plot, as shown in Fig.3.15.

LHM slab, TE mode SPP

Thickness dependent behavior of the SPP wave vectors in a LHM slab, with constitutive parameters of $\varepsilon_{r2} = -3$ and $\mu_{r2} = -0.9$ is studied at $\lambda_0 = 852nm$ for two different configurations of the surrounding media: (i) region-1 and -3 are free-space, and (ii) region-1 and -3 are different dielectric materials with $\varepsilon_{r1} = 0.5$, $\mu_{r1} = 1$ and free-space respectively. For this configuration, only TE waves can generate SPPs, since the combinations of the constitutive parameters of neighbor media has a solution of (3.38) only. By (3.38), the SPP wave vectors for the two layered semi-infinite structures are found to be $k_{sp} = (-3.1539)k_0$ and $k_{sp} = (-3.4755)k_0$ for configuration (i) and (ii), respectively. For the two configurations, the threshold thickness values are obtained from (3.41), TE mode, as $624.6nm$ and $452.0nm$ for configuration (i) and (ii) respectively with $\sigma = 10^{-3}$. The locations of the SPP wave vectors are shown in Figs.3.17 and 3.18 for two different thicknesses of the LHM slab in each configuration, one below and the other above the threshold thickness thickness values.

As seen in Figs.3.17 and 3.18, for two different slab configurations, there are two SPP wave vectors for the thickness less than the corresponding threshold thickness values. Since, the wavenumber of region-1 is less than the wavenumber of region-3 in configuration (ii), both of the SPP wave vectors are seen as singularities in reflection coefficient.

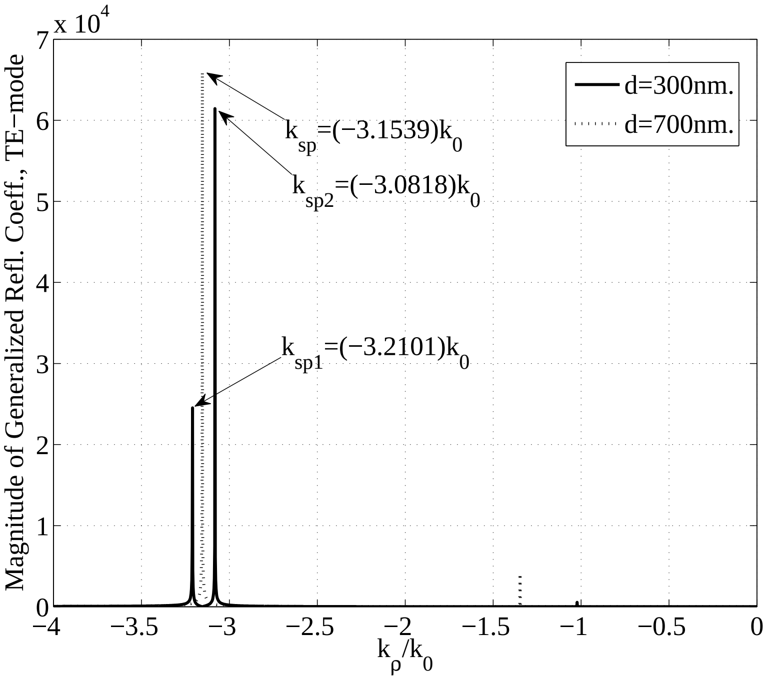

Figure 3.17: SPP poles of the LHM slab for different thicknesses, observation layer: region-1. region-2 is LHM with $\varepsilon_{r2} = -3$, $\mu_{r2} = -0.9$, and the thickness d. region-1 and region-3 are free-space.

Metallic slab, both TE and TM mode SPPs

To demonstrate a structure that supports SPPs for both the TE and TM modes, a metal slab with the constitutive parameters of $\varepsilon_{r2} = -10 - 0.1j$ and $\mu_{r2} = 1$ is put between

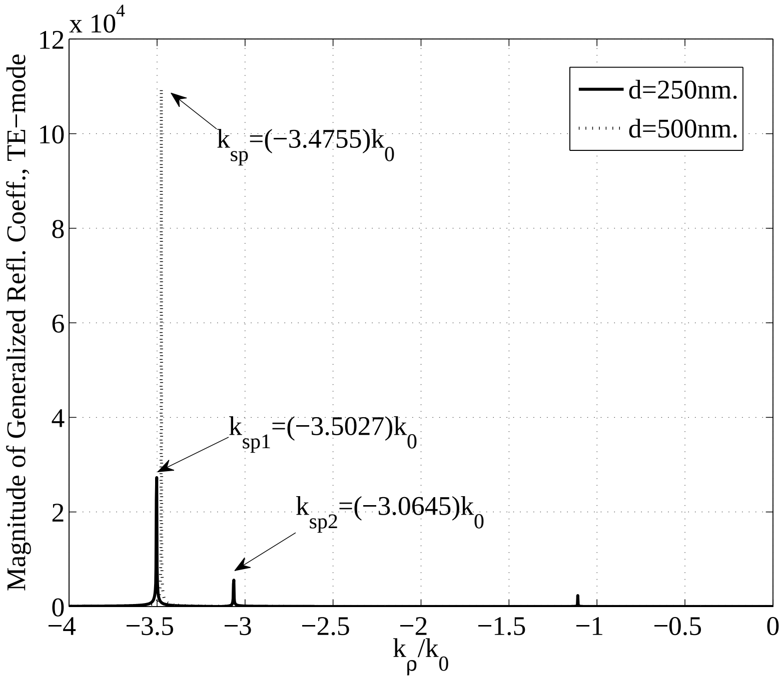

Figure 3.18: SPP poles of the LHM slab for different thicknesses,observation layer: region-1. region-2 is LHM with $\varepsilon_{r2} = -3$, $\mu_{r2} = -0.9$, and the thickness d. region-1 is a dielectric material with $\varepsilon_{r1} = 0.5$, $\mu_{r1} = 1$, and region-3 is free-space.

free-space with $\varepsilon_{r1} = 1$ and $\mu_{r1} = 1$ and a LHM medium with $\varepsilon_{r1} = -10$ and $\mu_{r1} = -0.1$. This configuration supports TM mode SPPs at the interface between region-1 and -2 ($k_{sp} = (1.0541 - j0.0006)k_0$) and TE mode SPPs at the interface between region-2 and -3 ($k_{sp} = (-1.0541 - j0.0005)k_0$). By TM mode (3.41) and with the observation layer taken to be region-1, the threshold thickness value is obtained as $244.5nm$, and for the TE mode, with the observation layer taken to be region-3, the threshold thickness value is obtained as $238.3nm$ for $\sigma = 10^{-3}$. The locations of the SPP wave vectors are shown in Figs.3.19 and 3.20 for different thicknesses of the metal slab for TM and TE modes respectively.

As seen in Fig.3.19, the location of the TM mode SPP wave vector changes depending on the thickness of the slab, due to the reflections from the interface between region-2 and -3. As in the previous cases, for thickness values greater than the threshold thickness, the location of the SPP wave vector coincides with the one that is found by (3.39). In the TE mode case, Fig.3.20, for thickness values less than the threshold thickness, the SPP wave vector generated in the interface between region-2 and -3 is seen as a singularity in the

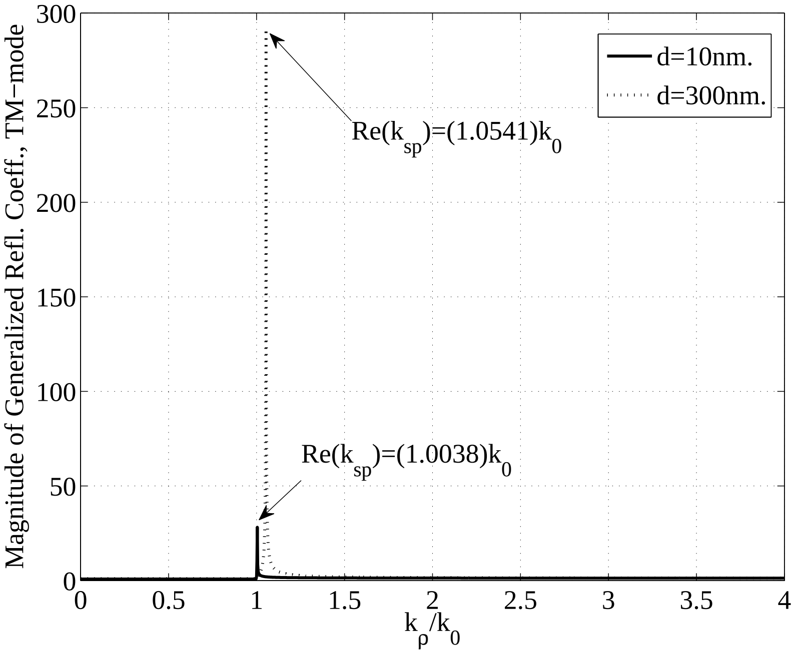

Figure 3.19: SPP poles of the LHM slab for different thicknesses, observation layer: region-1, TM mode. region-2 is metal with $\varepsilon_{r2} = -10 - j0.1$, $\mu_{r2} = 1$, and the thickness d. region-1 is free-space and region-3 is LHM with $\varepsilon_{r3} = -10$, $\mu_{r1} = -0.1$.

reflection coefficient. For thickness values greater than the threshold thickness value, the SPP wave vector coincides with the one that is found by (3.38), when the observation layer is region-3. But the SPP wave vector is not observed in the reflection coefficient, when the observation layer is region-1, due to the exponential decay in the slab.

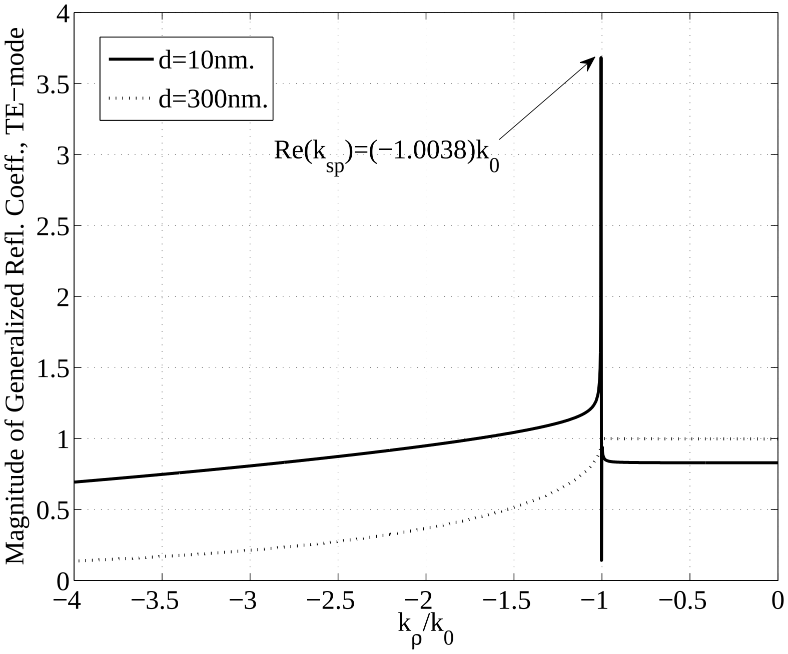

Figure 3.20: SPP poles of the LHM slab for different thicknesses, observation layer: region-1, TE mode. region-2 is metal with $\varepsilon_{r2} = -10 - j0.1$, $\mu_{r2} = 1$, and the thickness d. region-1 is free-space and region-3 is LHM with $\varepsilon_{r3} = -10$, $\mu_{r1} = -0.1$.

Chapter 4

APPROXIMATION OF SPATIAL DOMAIN GREEN'S FUNCTIONS

As discussed in Chapter 2, the transformation of Green's functions from spectral domain to spatial domain is obtained by the following Sommerfeld integrals:

$$\begin{aligned} G &= \frac{1}{4\pi}\int_{SIP} dk_\rho k_\rho H_0^{(2)}(k_\rho \rho)\tilde{G}(k_\rho) \\ G &= \frac{1}{2\pi}\int_{SIP} dk_\rho k_\rho J_0(k_\rho \rho)\tilde{G}(k_\rho) \end{aligned} \tag{4.1}$$

where G and $\tilde{G}$ are the spatial and spectral domain Green's functions, respectively and $H_0^{(2)}$ and J_0 are the Hankel function of the second kind and the Bessel function, respectively. SIP is the Sommerfeld integration path which was discussed in detail in Chapter 2 (An example of SIP is given in Fig.2.9). The evaluation of the Sommerfeld-type integrals is a time consuming process, due to the oscillatory and singular behavior of the integrand and the bounds of the integration which extends to ∞, as discussed in Chapter 2. Due to this fact, several approximation methods were introduced to eliminate the numerical integration.

In Section 4.1, an historical overview of approximation methods for spatial domain Green's functions will be given. In Section 4.2, the method that uses complex exponentials to approximate the Green's functions, i.e. Discrete Complex Images Method (DCIM), will be analyzed, and a new approach: 3-level DCIM will be introduced. Finally, in Section 4.3, numerical examples will be given to demonstrate the situations when the 3-level DCIM works or not.

4.1 Approximation methods for the evaluation of spatial domain Green's functions: An historical overview and existing methods

To overcome the computationally expensive numerical integration of Sommerfeld integrals, an approximation method for the spectral domain Green's function by complex exponentials was first introduced by Chow et.al. [18] for an HED over a thick substrate and extended to a general geometry by Mittra and Aksun [19]. In this method a single level approach was used, which obtained the uniformly-spaced samples of the spectral domain Green's functions on a single path and approximated them by complex exponentials by using Prony's method [76]. Then by using the Sommerfeld identity:

$$\begin{aligned}\frac{e^{-jkr}}{r} &= -\frac{j}{2}\int_{SIP} dk_\rho k_\rho H_0^{(2)}(k_\rho \rho)\frac{e^{-jk_z|z|}}{k_z} \\ &= -j\int_{SIP} dk_\rho k_\rho J_0(k_\rho \rho)\frac{e^{-jk_z|z|}}{k_z} \qquad (4.2)\end{aligned}$$

spatial domain Green's functions are obtained as a superposition spherical waves, of which the amplitudes and phases are determined by the results of complex exponential fitting, i.e. Prony's method. There were several difficulties in the implementation of this method such as the maximum range of the approximation and determining the number of exponentials to approximate the spectral domain Green's functions. These problems were eliminated by the robust approach of Aksun [21], which used a 2-level approach for the approximation. By using this method, the bounds of the approximations were assigned automatically. Also a better approximation scheme is obtained by using the Generalized Pencil-of-Function method (GPOF) [41], which is less noise sensitive compared to the original Prony's method, and also provides a good measure for choosing the number of exponentials. The 2-level approach gives good results for a variety of cases, but for structures: *i*) with lossy materials and *ii*) with no SWPs, the method fails to give correct results especially in the far-field region, as stated in [26, 31]. A number of modifications for the DCIM were introduced recently to increase the efficiency of the method [27, 77, 78], which will be discussed and improved in Section 4.2.

The other approximation techniques include:

1) *Analytical approximations with rational function fitting:* This method [29,31] first obtains the analytical behavior of the spatial domain Green's functions near the source point, i.e. $\rho \to 0$, which represents the asymptotic behavior of the spectral domain Green's functions. Then, after subtracting this contribution from the spectral domain Green's function, a rational function fitting is applied. Therefore the total spatial domain Green's function is obtained as a sum of the contributions of the analytical part and the result of the fitting, which are a set of line sources, that generates cylindrical waves in the spatial domain by

using following integral identity:

$$\int_{-\infty}^{\infty} \frac{1}{k_\rho^2 - k_{\rho p}^2} H_0^{(2)}(k_\rho \rho) k_\rho dk_\rho = -j\pi H_0^{(2)}(k_\rho \rho) \tag{4.3}$$

This method gives results those are in good agreement with the results obtained by numerical integration. But as shown in [29, 31] an intense number of analytical derivations must be carried to obtain the asymptotic behavior of the spectral domain for different layered structures. Therefore one can argue that the method is not fully numerical, and a fully numerical method that gives results with the same accuracy would be preferred.

2) *Rational function fitting only:* This method [25, 28] first obtains the quasi-static images analytically, which represent spherical waves in spatial domain. Then, after subtracting the contribution of the quasi-static images from the spectral domain Green's function, a rational fitting algorithm, vector fitting (VECT-FIT) [79], is applied. As the result, an approximation that contains a set of spherical (quasi-static images) and cylindrical (result of VECT-FIT) waves is obtained in spatial domain by using the integral identities (4.2) and (4.3). This method obtains good results for a variety of different geometries. But since the approximation of rational functions, i.e. the VECT-FIT algorithm, needs relatively higher computational resources and the extraction of quasi-static terms is not unique and can be very tedious, as stated by the authors [28], a fully numerical and unique approach would be preferred.

3) *A combination of rational functions and complex exponentials fitting:* This method [30, 80] can be seen as a mixture of the DCIM and the one given in 2) above (Rational function fitting only). In this method, a two-level approximation is applied on the sampling paths those are exactly the same as the 2-level DCIM. The first level of the method is the same as DCIM and the second level is the application of VECT-FIT to the spatial domain Green's function, after the subtraction of the terms obtained in the first level. Therefore, the total spatial domain Green's function is obtained as a sum of spherical (from the first level, i.e. exponential fitting) and cylindrical (from second level, i.e. VECT-FIT) waves by using the integral identities (4.2) and (4.3), respectively. The shortcomings of this method is similar to the method of the kind given in 2), i.e. the computationally expensive and non-unique nature of VECT-FIT. Therefore a cheaper method would be preferred that gives the same accuracy.

As can be seen, the approximation methods first approximates the spectral domain

Green's functions by using analytical approaches or fitting algorithms. Then by using the appropriate integral identities, a transformation from the spectral domain to spatial domain is obtained. But due to the facts those are stated above, a fully numerical, robust, automatic and unique method would be preferred for the approximation of spatial domain Green's functions.

4.2 The Discrete Complex Images Method (DCIM)

4.2.1 An overview of 2-level DCIM

In the two level approximation approach [21], the spectral domain Green's function is sampled along two paths on the complex k_ρ plane as shown in Fig.4.1.

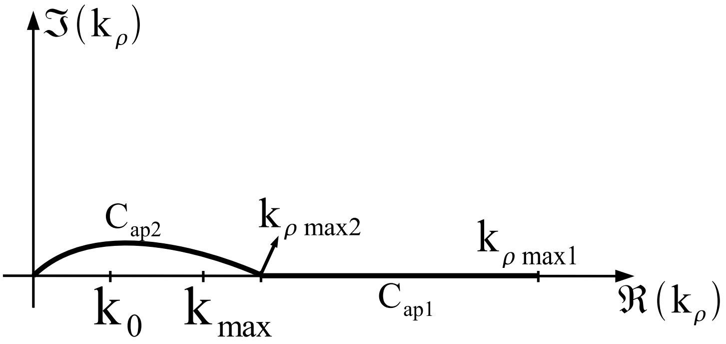

Figure 4.1: Paths of approximation for 2-level DCIM on complex k_ρ plane.

In Fig.4.1, k_{max} is the maximum value of the real parts of the wave vectors of the layers and k_0 is the wave vector of the source region. The paths mapped to complex k_z plane can be seen in Fig.4.2 below. To be able to use GPOF, the samples must be taken linearly with respect to the variable of fitting, t. Therefore, the following mappings are made between the linear sampling variable t and wave vector component in z-direction, k_z, (to be able to use the Sommerfeld identity given in (4.2)).

$$\begin{aligned} &\text{For } C_{ap1}: & k_z &= -jk_0[T_{02}+t] & 0 \le t \le T_{01} \\ &\text{For } C_{ap2}: & k_z &= k_0\left[-jt+\left(1-\tfrac{t}{T_{02}}\right)\right] & 0 \le t \le T_{02} \end{aligned} \qquad (4.4)$$

By using the mapping given in (4.4), the values of k_{zmax1} and k_{zmax2} shown in Fig.4.2 are

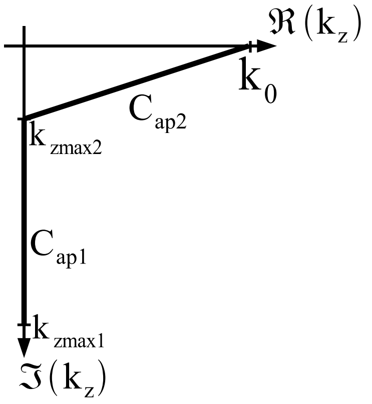

Figure 4.2: Paths of approximation for 2-level DCIM on complex k_z plane.

given by:

$$\begin{aligned} k_{zmax1} &= -jk_0(T_{01}+T_{02}) \\ k_{zmax2} &= -jk_0(T_{02}) \end{aligned} \tag{4.5}$$

by using (4.5), the values of $k_{\rho max1}$ and $k_{\rho max2}$ shown in Fig.4.1 are found to be:

$$\begin{aligned} k_{\rho max1} &= k_0\sqrt{1+(T_{01}+T_{02})^2} \\ k_{\rho max2} &= k_0\sqrt{1+(T_{02})^2} \end{aligned} \tag{4.6}$$

As seen in (4.6), one must be careful when deciding on the boundaries of approximation. In other words, $k_{\rho max2}$ must be greater than the k_{max} value as seen in Fig.4.1. An example of the approximation paths and sampling locations on the complex k_ρ and k_z planes are plotted below in Figs. 4.3 and 4.4 for $T_{01}=1$ and $T_{02}=2$.

Before starting the 2-level approximation, the locations of surface wave poles must be found and subtracted from the integrand, i.e. from the spectral domain Green's function $\tilde{G}$, by using the Cauchy integration formula, as discussed in detail in Chapter 2. For this purpose, numerical root finding algorithms as discussed in Chapter 2 or the modified VECTFIT algorithm as given in Appendix C can be used. After the subtraction of the surface wave poles, in the first step of the 2-level DCIM, the spectral domain Green's function, $\tilde{G}\times k_z$ is sampled on the C_{ap1}, and by applying GPOF, a set of exponentials of the form

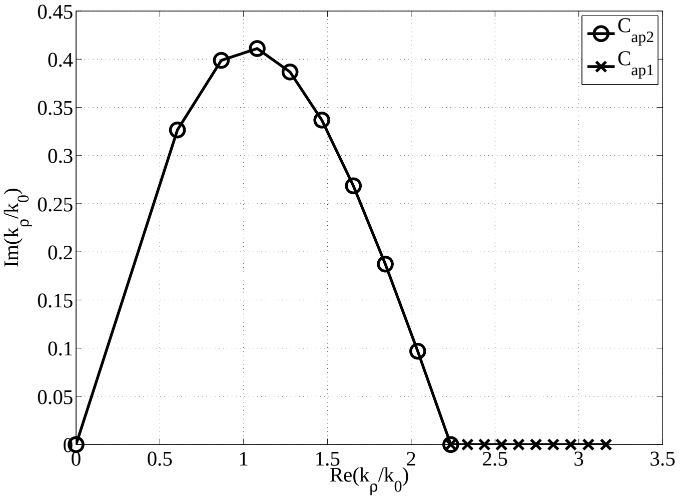

Figure 4.3: Approximation paths and sample point locations of 2-level DCIM on complex k_ρ plane for $T_{01} = 1$ and $T_{02} = 2$. 10 sample points are taken on both paths.

are obtained[21]:

$$\begin{aligned} & f(k_\rho) \left(\cong \tilde{G} \times k_{z0} \text{ for } k_\rho \in C_{ap1} \right) \\ & = \sum_{n=1}^{N_1} b_{1n} e^{\beta_{1n} t} = \sum_{n=1}^{N_1} a_{1n} e^{-\alpha_{1n} k_{z0}} \\ \alpha_{1n} = \frac{\beta_{1n}}{jk_0} \qquad & a_{1n} = b_{1n} e^{-jk_0 \alpha_{1n} T_{02}} \end{aligned} \tag{4.7}$$

where b_{1n} and β_{1n} are the coefficients and exponents obtained from the GPOF method, and N_1 is the number of exponentials used for this approximation. After the first set of exponentials are obtained as seen in (4.7), they are subtracted from the remaining part of the integrand, and the second level of the approximation is performed on the path C_{ap2} seen in Figs.4.1 and 4.2, which gives the following results:

$$\begin{aligned} \tilde{G} \times k_{z0} - f(k_\rho) \cong \sum_{n=1}^{N_2} b_{2n} e^{\beta_{2n} t} = \sum_{n=1}^{N_2} a_{2n} e^{-\alpha_{2n} k_{z0}} \text{ for } k_\rho \in C_{ap2} \\ \alpha_{2n} = \frac{\beta_{2n} T_{02}}{k_0 (1 + jT_{02})} \qquad a_{2n} = b_{2n} e^{k_0 \alpha_{2n}} \end{aligned} \tag{4.8}$$

where b_{2n} and β_{2n} are the coefficients and exponents obtained from the GPOF method, and N_2 is the number of exponentials used for this approximation. Therefore the spatial domain Green's function is given by the sum of the exponentials obtained in the 2-level

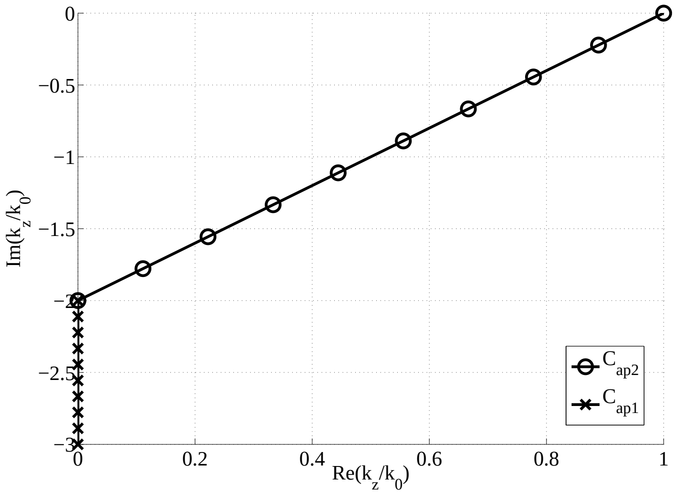

Figure 4.4: Approximation paths and sample point locations of 2-level DCIM on complex k_z plane for $T_{01} = 1$ and $T_{02} = 2$. 10 sample points are taken on both paths.

approximation, by using the Sommerfeld identity (4.2), which is given by:

$$G(\rho) = \sum_{n=1}^{N_1} a_{1n} \frac{e^{-jk_0 r_{1n}}}{r_{1n}} + \sum_{n=1}^{N_2} a_{2n} \frac{e^{-jk_0 r_{2n}}}{r_{2n}} \tag{4.9}$$

where

$$r_{in} = \sqrt{\rho^2 + (-j\alpha_{in})^2} \tag{4.10}$$

A number of different paths were introduced that work without the subtraction of SWPs [27, 77]. They use a higher number of sampling points and exponentials to approximate the spectral domain Green's functions, which can be more expensive computationally.

4.2.2 The 3-level DCIM

As discussed in [26, 31], the most important shortcoming of the 2-level DCIM is its lack of capturing the contribution of the branch point. In spatial domain, the contribution of the branch point is seen as lateral waves [18, 81] which has the following asymptotic behavior for large ρ:

$$\frac{e^{-jk_0\rho}}{\rho^2} \tag{4.11}$$

where k_0 is the branch point of the structure [1]. The other contribution that plays an important role in spatial domain Green's function is the SWPs, which is seen as cylindrical waves and has the following asymptotic behavior for large ρ:

$$\frac{e^{-jk_{swp}\rho}}{\sqrt{\rho}} \tag{4.12}$$

where k_{swp} is the wave number of the SWP. As can be seen in (4.11) and (4.12), when the SWP has an imaginary part, the contribution of the surface waves decay exponentially, and as the result, the contribution of the branch point, i.e. the lateral wave, determines the far-field behavior of the spatial domain Green's function. This situation can be seen in [31]: 1) Lossless materials when the spectral domain Green's function does not have proper poles, 2) Lossy materials and 3) When a pole is very close to the branch point. To overcome this problem, the sampling paths of the 2-level DCIM are modified, which results in a 3-level approximation that is capable of capturing the contribution of the branch point. 3 such sampling paths are given below.

3-level DCIM: Approach 1

This approach was proposed in [78]. In this approach, the spectral domain Green's function is sampled along three paths on the complex k_ρ plane as shown in Fig.4.5. The paths mapped to complex k_z plane can be seen in Fig.4.6 below. The following mappings are

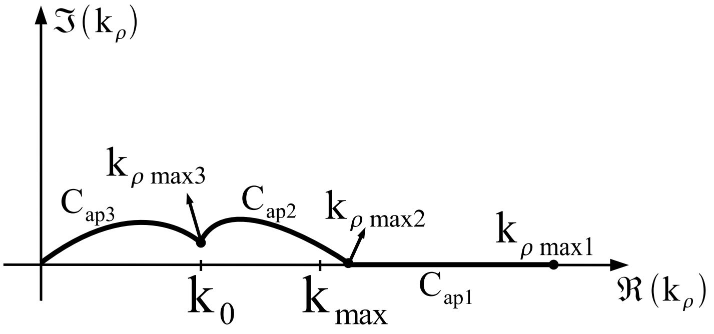

Figure 4.5: Approximation paths for the first 3-level DCIM method on complex k_ρ plane.

---

[1] In structures where the radiating medium is air, k_0 is the wave number of free-space.

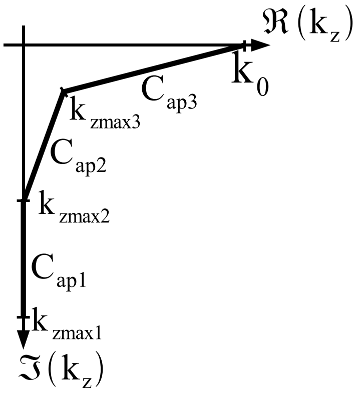

Figure 4.6: Approximation paths for the first 3-level DCIM method on complex k_z plane.

made between the linear sampling variable t and wave vector component in z-direction, k_z (to be able to use the integral identity given in (4.2)).

$$\begin{array}{llr} \text{For } C_{ap1}: & k_z = -jk_0\left[T_{02} + (T_{01} - T_{02})\,t\right] & 0 \le t \le 1 \\ \text{For } C_{ap2}: & k_z = k_0\left[(T'_{03} - jT_{03}) - (T'_{03} + j(T_{02} - T_{03}))t\right] & 0 \le t \le 1 \\ \text{For } C_{ap3}: & k_z = k_0\left[1 - (1 - T'_{03} + jT_{03})t\right] & 0 \le t \le 1 \end{array} \tag{4.13}$$

By using the mapping given in (4.13), the values of k_{zmax1}, k_{zmax2} and k_{zmax3} shown in Fig.4.6 are given by:

$$\begin{aligned} k_{zmax1} &= -jk_0T_{01} \\ k_{zmax2} &= -jk_0T_{02} \\ k_{zmax3} &= k_0(T'_{03} - jT_{03}) \end{aligned} \tag{4.14}$$

by using (4.14), the values of $k_{\rho max1}$, $k_{\rho max2}$ and $k_{\rho max3}$ shown in Fig.4.5 are found to be:

$$\begin{aligned} k_{\rho max1} &= k_0\sqrt{1 + (T_{01})^2} \\ k_{\rho max2} &= k_0\sqrt{1 + (T_{02})^2} \\ k_{\rho max3} &= k_0\sqrt{1 - (T'_{03} - jT_{03})^2} \end{aligned} \tag{4.15}$$

As in the case of 2-level DCIM, one must be careful when deciding on the boundaries of approximation. In other words, $k_{\rho max2}$ must be greater than the k_{max} value as seen in Fig.4.5. An example of the approximation paths and sampling locations on the complex k_ρ

and k_z planes are plotted below in Figs.4.7 and 4.8 for $T_{01} = 3$, $T_{02} = 2$, $T'_{03} = 0.01$ and $T_{03} = 0.01$.

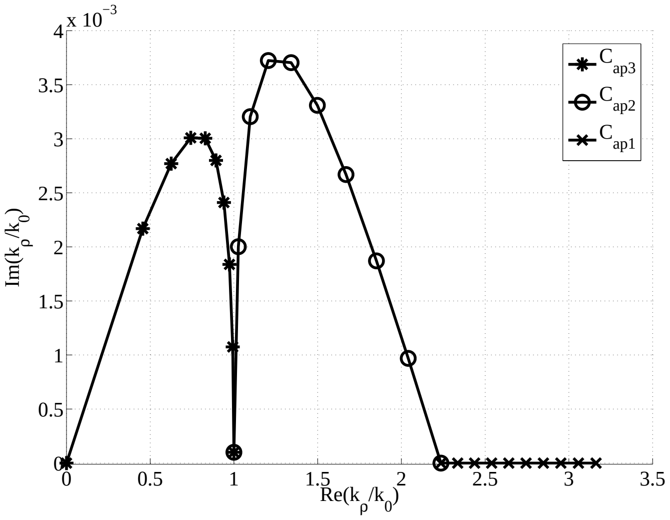

Figure 4.7: Approximation paths and sample point locations of the first 3-level DCIM approach on complex k_ρ plane for $T_{01} = 3$, $T_{02} = 2$ and $T'_{03} = 0.01$ and $T_{03} = 0.01$. 10 sample points are taken on all the three paths.

3-level DCIM: Approach 2

In the second three level approximation approach, the spectral domain Green's function is sampled along three paths on the complex k_ρ plane as shown in Fig.4.9. The paths mapped to complex k_z plane can be seen in Fig.4.10 below. The following mappings are made between the linear sampling variable t and wave vector component in z-direction, k_z (to be able to use the integral identity given in (4.2)).

$$\begin{aligned}
&\text{For } C_{ap1}: && k_z = -jk_0\left[\frac{T_{02}}{T_{03}+1} + t\right] && 0 \le t \le T_{01} \\
&\text{For } C_{ap2}: && k_z = k_0\left[\frac{1}{T_{03}+1}\right]\left[-jt + \left[1 - \frac{t}{T_{02}}\right]\right] && 0 \le t \le T_{02} \\
&\text{For } C_{ap3}: && k_z = k_0\left[1 - \frac{t}{T_{03}+1}\right] && 0 \le t \le T_{03}
\end{aligned} \tag{4.16}$$

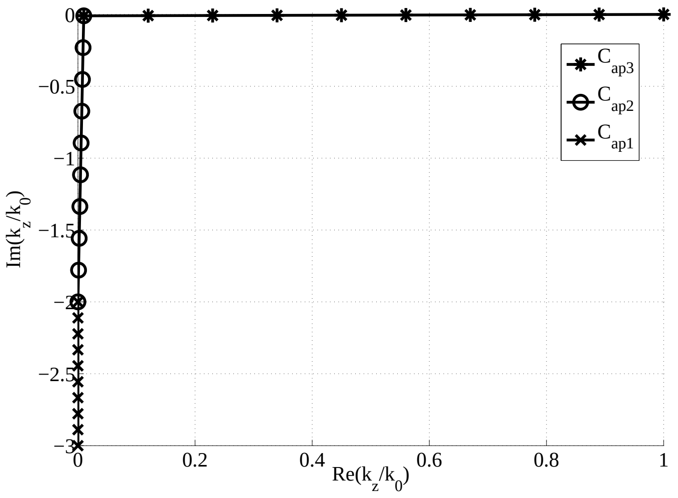

Figure 4.8: Approximation paths and sample point locations of the first 3-level DCIM approach on complex k_z plane for $T_{01} = 3$, $T_{02} = 2$ and $T'_{03} = 0.01$ and $T_{03} = 0.01$. 10 sample points are taken on all the three paths.

By using the mapping given in (4.16), the values of k_{zmax1}, k_{zmax2} and k_{zmax3} shown in Fig.4.10 are given by:

$$\begin{aligned} k_{zmax1} &= -jk_0\left(\frac{T_{02}}{T_{03}+1}+T_{01}\right) \\ k_{zmax2} &= -jk_0\left(\frac{T_{02}}{T_{03}+1}\right) \\ k_{zmax3} &= k_0\frac{1}{T_{03}+1} \end{aligned} \tag{4.17}$$

by using (4.17), the values of $k_{\rho max1}$, $k_{\rho max2}$ and $k_{\rho max3}$ shown in Fig.4.10 are found to be:

$$\begin{aligned} k_{\rho max1} &= k_0\sqrt{1+\left(\frac{T_{02}}{T_{03}+1}+T_{01}\right)^2} \\ k_{\rho max2} &= k_0\sqrt{1+\left(\frac{T_{02}}{T_{03}+1}\right)^2} \\ k_{\rho max3} &= k_0\sqrt{1-\left(\frac{1}{T_{03}+1}\right)^2} \end{aligned} \tag{4.18}$$

An example of the approximation paths and sampling locations on the complex k_ρ and k_z planes are plotted below in Figs. 4.11 and 4.12 for $T_{01} = 1$, $T_{02} = 200$ and $T_{03} = 99$.

As discussed in Chapter 3, in layered structures which contain a combination of lossy LHMs and RHMs, there can be SWPs and SPPs singularities which have positive imaginary

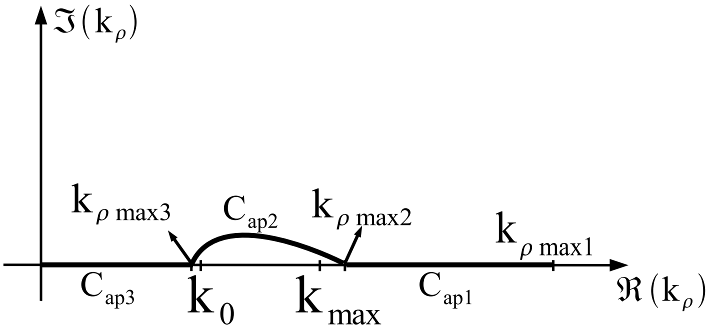

Figure 4.9: Approximation paths for the second 3-level DCIM on complex k_ρ plane.

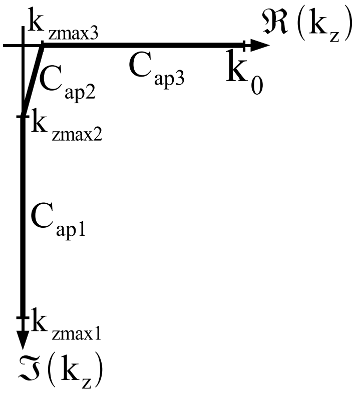

Figure 4.10: Approximation paths for the second 3-level DCIM on complex k_z plane.

parts. A positive imaginary part in the wave vector is not physical, since it represents an exponentially growing function in the direction of power flow for $e^{j\omega t}$ convention. Therefore only the singularities with negative imaginary parts are added as surface wave contributions to the spatial domain Green's functions. But, since the spectral domain Green's functions are even in k_ρ domain, there can be singularities in the first quadrant of the complex k_ρ plane for this kind of layered structures. Due to this fact, the paths introduced above cannot be used in the approximation process of spectral domain Green's functions, since the paths can cross the singularities with positive imaginary parts. To handle this problem, a sampling path is introduced below that passes on the real k_ρ axis.

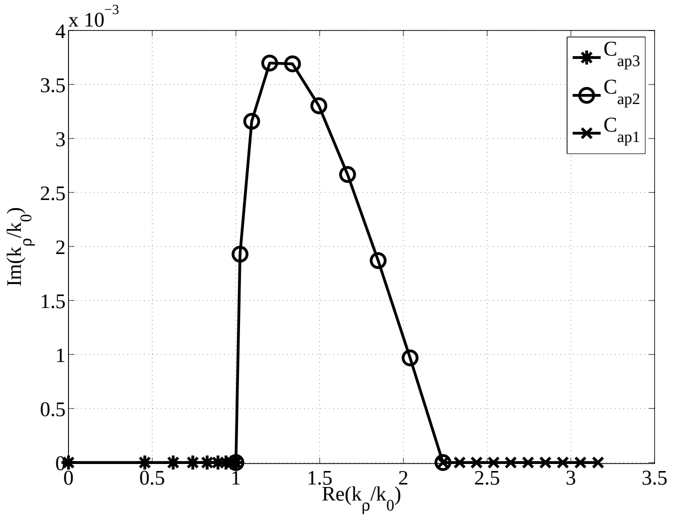

Figure 4.11: Approximation paths and sample point locations of the second 3-level DCIM approach on complex k_ρ plane for $T_{01} = 1$, $T_{02} = 200$ and $T_{03} = 99$. 10 sample points are taken on all the three paths.

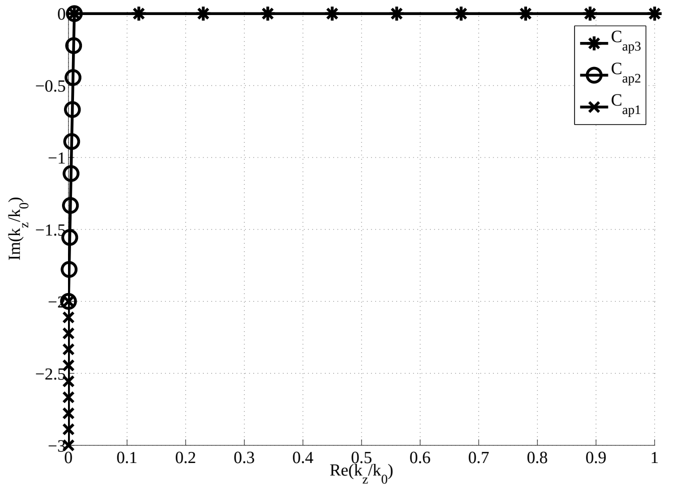

Figure 4.12: Approximation paths and sample point locations of the second 3-level DCIM approach on complex k_z plane for $T_{01} = 1$, $T_{02} = 200$ and $T_{03} = 99$. 10 sample points are taken on all the three paths.

3-level DCIM: Approach 3

In the third three level approximation approach, the spectral domain Green's function is sampled along three paths on the complex k_ρ plane as shown in Fig.4.13. The paths mapped to complex k_z plane can be seen in Fig.4.14 below. The following mappings are made between the linear sampling variable t and wave vector component in z-direction, k_z (to be able to use the integral identity given in (4.2)).

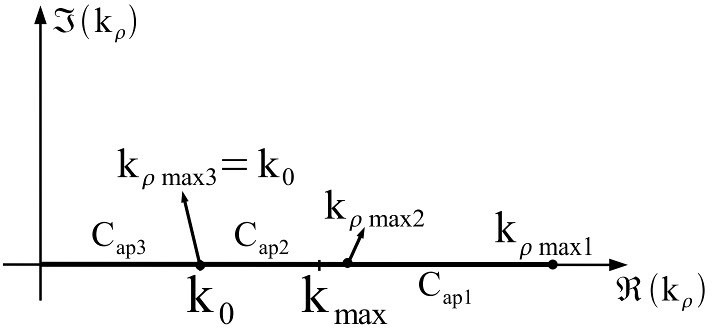

Figure 4.13: Approximation paths for the third 3-level DCIM on complex k_ρ plane.

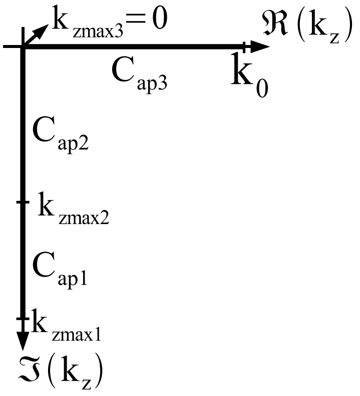

Figure 4.14: Approximation paths for the third 3-level DCIM on complex k_z plane.

$$\begin{aligned}
&\text{For } C_{ap1}: && k_z = -jk_0\left[t + T_{02}\right] && 0 \le t \le T_{01}\\
&\text{For } C_{ap2}: && k_z = -jk_0\left[t\right] && 0 \le t \le T_{02}\\
&\text{For } C_{ap3}: && k_z = k_0\left[1 - \tfrac{t}{T_{03}}\right] && 0 \le t \le T_{03}
\end{aligned} \tag{4.19}$$

By using the mapping given in (4.19), the values of k_{zmax1}, k_{zmax2} and k_{zmax3} shown in Fig.4.14 are given by:

$$\begin{aligned} k_{zmax1} &= -jk_0 \left(T_{01} + T_{02}\right) \\ k_{zmax2} &= -jk_0 \left(T_{02}\right) \\ k_{zmax3} &= 0 \end{aligned} \tag{4.20}$$

by using (4.20), the values of $k_{\rho max1}$, $k_{\rho max2}$ and $k_{\rho max3}$ shown in Fig.4.14 are found to be:

$$\begin{aligned} k_{\rho max1} &= k_0 \sqrt{1 + \left(T_{02} + T_{01}\right)^2} \\ k_{\rho max2} &= k_0 \sqrt{1 + \left(T_{02}\right)^2} \\ k_{\rho max3} &= k_0 \end{aligned} \tag{4.21}$$

An example of the approximation paths and sampling locations on the complex k_ρ and k_z planes are plotted below in Figs. 4.15 and 4.16 for $T_{01} = 1$, $T_{02} = 2$ and $T_{03} = 1$.

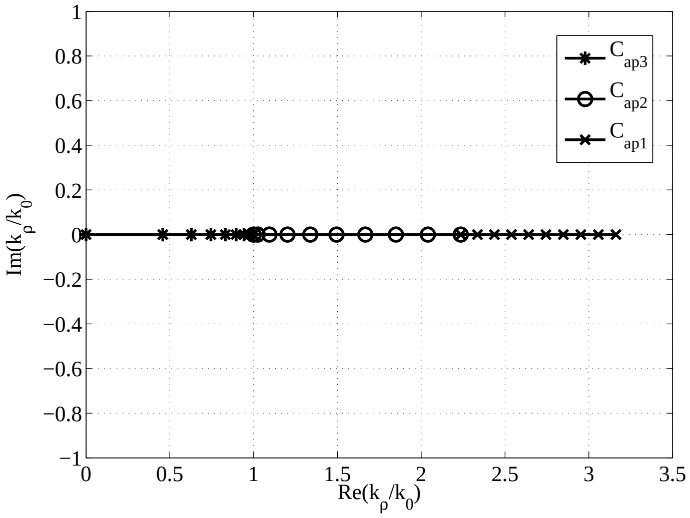

Figure 4.15: Approximation paths and sample point locations of the third 3-level DCIM approach on complex k_ρ plane for $T_{01} = 1$, $T_{02} = 2$ and $T_{03} = 1$. 10 sample points are taken on all the three paths.

Before starting the 3-level approximation, the locations of surface wave poles must be found and subtracted from the integrand, i.e. from the spectral domain Green's function $\tilde{G}$

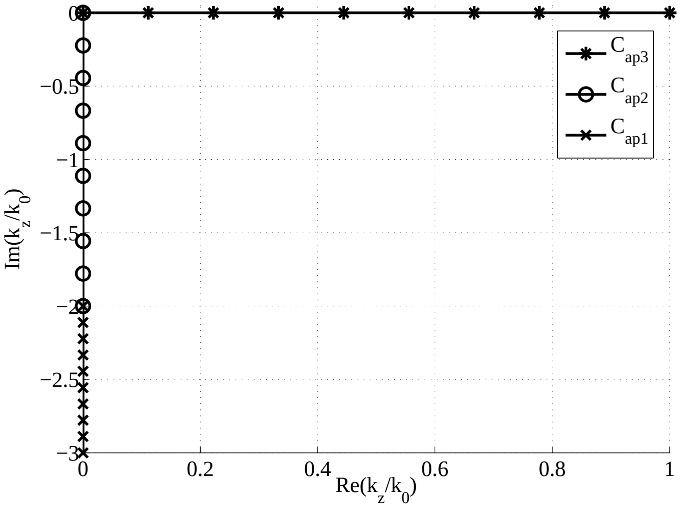

Figure 4.16: Approximation paths and sample point locations of the third 3-level DCIM approach on complex k_z plane for $T_{01} = 1$, $T_{02} = 2$ and $T_{03} = 1$. 10 sample points are taken on all the three paths.

by using the Cauchy integration formula. The locations of the SWPs can be found by the root finding algorithm discussed in Chapter 2 or the modified VECT-FIT algorithm given in Appendix C. After the subtraction of the surface wave poles, in the first step of the 3-level DCIM, the spectral domain Green's function, $\tilde{G} \times k_z$ is sampled on the C_{ap1}, and by applying GPOF, a set of exponentials of the form are obtained:

$$\begin{aligned} & f_1(k_\rho) \left(\cong \tilde{G} \times k_{z0} \text{ for } k_\rho \in C_{ap1} \right) \\ & = \sum_{n=1}^{N_1} b_{1n} e^{\beta_{1n} t} = \sum_{n=1}^{N_1} a_{1n} e^{-\alpha_{1n} k_{z0}} \end{aligned} \tag{4.22}$$

where b_{1n} and β_{1n} are the coefficients and exponents obtained from the GPOF method, and N_1 is the number of exponentials used for this approximation. The coefficients transformed to k_z domain are given by:

$$\alpha_{1n} = \frac{\beta_{1n}}{jk_0(T_{01} - T_{02})} \qquad a_{1n} = b_{1n} e^{-jk_0 \alpha_{1n} T_{02}} \qquad \text{for approach 1} \tag{4.23}$$

$$\alpha_{1n} = \frac{\beta_{1n}}{jk_0} \qquad a_{1n} = b_{1n} e^{-jk_0 \alpha_{1n} \frac{T_{02}}{T_{03}+1}} \qquad \text{for approach 2} \tag{4.24}$$

$$\alpha_{1n} = \frac{\beta_{1n}}{jk_0} \qquad a_{1n} = b_{1n} e^{-jk_0 \alpha_{1n} T_{02}} \qquad \text{for approach 3} \tag{4.25}$$

After the first set of exponentials are obtained as seen in (4.22), they are subtracted from the remaining part of the integrand, and the second level of the approximation is performed on the path C_{ap2}, which gives the following results:

$$\tilde{G} \times k_{z0} - f_1(k_\rho) \cong f_2(k_\rho) = \sum_{n=1}^{N_2} b_{2n} e^{\beta_{2n} t} = \sum_{n=1}^{N_2} a_{2n} e^{-\alpha_{2n} k_{z0}} \text{ for } k_\rho \in C_{ap2}$$

$$\alpha_{2n} = \frac{\beta_{2n} T_{02}(T_{03}+1)}{k_0(1+jT_{02})} \qquad a_{2n} = b_{2n} e^{k_0 \frac{\alpha_{2n}}{T_{03}+1}} \tag{4.26}$$

where b_{2n} and β_{2n} are the coefficients and exponents obtained from the GPOF method, and N_2 is the number of exponentials used for this approximation. The coefficients transformed to k_z domain are given by:

$$\alpha_{2n} = \frac{\beta_{2n}}{k_0(j(T_{02}-T_{03})+T'_{03})} \qquad a_{2n} = b_{2n} e^{k_0 \alpha_{2n}(T'_{03}-jT_{03})} \qquad \text{for approach 1} \tag{4.27}$$

$$\alpha_{2n} = \frac{\beta_{2n} T_{02}(T_{03}+1)}{k_0(1+jT_{02})} \qquad a_{2n} = b_{2n} e^{k_0 \frac{\alpha_{2n}}{T_{03}+1}} \qquad \text{for approach 2} \tag{4.28}$$

$$\alpha_{2n} = \frac{\beta_{2n}}{jk_0} \qquad a_{2n} = b_{2n} \qquad \text{for approach 3} \tag{4.29}$$

After the second set of exponentials are obtained as seen in (4.26), they are subtracted from the remaining part of the integrand, and the second level of the approximation is performed on the path C_{ap3}, which gives the following results:

$$\tilde{G} \times k_{z0} - f_1(k_\rho) - f_2(k_\rho) \cong \sum_{n=1}^{N_3} b_{3n} e^{\beta_{3n} t} = \sum_{n=1}^{N_3} a_{3n} e^{-\alpha_{3n} k_{z0}} \text{ for } k_\rho \in C_{ap3} \tag{4.30}$$

where b_{3n} and β_{3n} are the coefficients and exponents obtained from the GPOF method, and N_3 is the number of exponentials used for this approximation.The coefficients transformed to k_z domain are given by:

$$\alpha_{3n} = \frac{\beta_{3n}}{k_0(1-T'_{03}+jT_{03})} \qquad a_{3n} = b_{3n} e^{k_0 \alpha_{3n}} \qquad \text{for approach 1} \tag{4.31}$$

$$\alpha_{3n} = \frac{\beta_{3n}(T_{03}+1)}{k_0} \qquad a_{3n} = b_{3n} e^{k_0 \alpha_{3n}} \qquad \text{for approach 2} \tag{4.32}$$

$$\alpha_{3n} = \frac{\beta_{3n} T_{03}}{k_0} \qquad a_{3n} = b_{3n} e^{k_0 \alpha_{3n}} \qquad \text{for approach 3} \tag{4.33}$$

Therefore the spatial domain Green's function is given by the sum of the exponentials obtained in the 3-level approximation, by using the Sommerfeld identity (4.2), which is given by:

$$G(\rho) = \sum_{n=1}^{N_1} a_{1n} \frac{e^{-jk_0 r_{1n}}}{r_{1n}} + \sum_{n=1}^{N_2} a_{2n} \frac{e^{-jk_0 r_{2n}}}{r_{2n}} + \sum_{n=1}^{N_3} a_{3n} \frac{e^{-jk_0 r_{3n}}}{r_{3n}} \tag{4.34}$$

where

$$r_{in} = \sqrt{\rho^2 + (-j\alpha_{in})^2} \tag{4.35}$$

where the coefficients α_i and a_i are given above for the different approaches of 3-level DCIM.

4.2.3 Comments on the branch point contribution

As discussed above, the intention of the 3-level method is to be able to capture the branch point contribution. Here, the mathematical background of the fact that lateral waves that decay with $\frac{1}{\rho^2}$ for $\rho \to \infty$ can be approximated by spherical waves, i.e. the far-field behavior of spatial domain Green's functions can be approximated by the DCIM even when the surface wave contribution becomes weak, when $\rho \to \infty$, if the contribution of the branch point is captured.

Let the following exponential is obtained by the DCIM:

$$\frac{e^{-jkr_1}}{r_1} \tag{4.36}$$

where r_1 is given by:

$$r_1 = \sqrt{\rho^2 + (-j\alpha_1)} \tag{4.37}$$

as given in (4.34) and (4.35) and α_1 is the exponent obtained by the DCIM. When $\rho \to \infty$, the square root in (4.37) can be approximated by:

$$\sqrt{\rho^2 + (-j\alpha_1)} \cong \rho\left(1 - \frac{\alpha_1^2}{2\rho^2}\right) \tag{4.38}$$

combining (4.36) with (4.38) gives:

$$\frac{e^{-jkr_1}}{r_1} \cong \frac{e^{-jk\rho}e^{jk\frac{\alpha_1^2}{2\rho}}}{\rho\left(1 - \frac{\alpha_1^2}{2\rho^2}\right)} \cong \frac{e^{-jk\rho}}{\rho}\frac{1 + jk\frac{\alpha_1^2}{2\rho}}{1 - \frac{\alpha_1^2}{2\rho^2}} \tag{4.39}$$

by using the Taylor expansion for fractions i.e.:

$$\frac{1}{t} = 1 + t + t^2 + ... \qquad \text{for } |t| < 1 \tag{4.40}$$

gives the following relation (where $t \equiv \frac{\alpha_1^2}{2\rho^2}$ in (4.40)):

$$\frac{1}{1 - \frac{\alpha_1^2}{2\rho^2}} \cong 1 + \frac{\alpha_1^2}{2\rho^2} \tag{4.41}$$

substituting (4.41) into (4.39) results in:

$$\frac{e^{-jkr_1}}{r_1} \cong \frac{e^{-jk\rho}}{\rho}\left[1 + jk\frac{\alpha_1^2}{2\rho}\right]\left[1 + \frac{\alpha_1^2}{2\rho^2}\right] \tag{4.42}$$

by grouping the same terms in (4.42), the following relation is obtained:

$$\frac{e^{-jkr_1}}{r_1} \cong \frac{e^{-jk\rho}}{\rho} + jk\frac{\alpha_1^2}{2\rho^2}e^{-jk\rho} + O(\frac{1}{\rho^3}) \tag{4.43}$$

Now suppose that 2 exponentials are fitted to the data, obtained from a path that is close to the branch point. Using (4.43), one can obtain the following relation in spatial domain:

$$a_1\frac{e^{-jkr_1}}{r_1} + a_2\frac{e^{-jkr_2}}{r_2} \cong (a_1 + a_2)\frac{e^{-jk\rho}}{\rho} + \frac{jk}{2}\left(a_1\alpha_1^2 + a_2\alpha_2^2\right)\frac{e^{-jk\rho}}{\rho^2} + O(\frac{1}{\rho^3}) \tag{4.44}$$

From the result obtained in (4.44), it can be concluded that the DCIM method can represent lateral waves (i.e. a wave with the algebraic decay of $\frac{1}{\rho^2}$ as given in 4.11) if the following relations hold:

$$\begin{aligned} a_1 &+ a_2 \cong 0 \\ \alpha_1 &+ \alpha_2 \ncong 0 \end{aligned} \tag{4.45}$$

in (4.44). To investigate this behavior, a problematic case for the 2-level DCIM, a layered geometry that contains lossy materials, is analyzed by applying the DCIM method only on the data obtained from second path (C_{ap2}) of the 3-level DCIM as discussed in Section 4.2.2. Before the application of DCIM, the SWPs are subtracted analytically. The example geometry can be seen in Fig.4.17. The results of the fitting are tabulated below in Table 4.1.

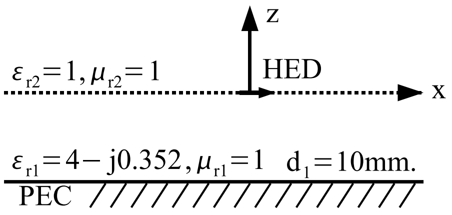

Figure 4.17: A geometry that is known to be problematic for the 2-level DCIM: A PEC backed, lossy slab. ($f = 10GHz$)

Method	Path	T_{02}	$T_{03}(-T'_{03})$	$a_1 + a_2$	$\alpha_1 + \alpha_2$
2-lvl	C_{ap2}	2	–	$-0.0006 + j0.0103$	$-2.509 \times 10^{-2} - j2.8597 \times 10^{-1}$
3-lvl, approach 1	C_{ap2}	0.1	$0.01 - 0.01$	$0.02057 + j0.0109$	$-3.4898 \times 10^{-6} + j4.3693 \times 10^{-5}$
3-lvl, approach 1	C_{ap2}	2	$0.01 - 0.01$	$0.0130 + j0.01807$	$-1.7739 \times 10^{-3} - j2.3609 \times 10^{-3}$
3-lvl, approach 1	C_{ap2}	20	$0.01 - 0.01$	$-0.0134 + j0.0164$	$-9.4937 \times 10^{-2} - j8.2253 \times 10^{-2}$
3-lvl, approach 2	C_{ap2}	1	99	$-0.0131 - j0.0168$	$1.8777 \times 10^{-9} + j6.5919 \times 10^{-10}$
3-lvl, approach 2	C_{ap2}	200	99	$-0.0129 - j0.0578$	$-6.3126 \times 10^{-3} + j1.8262 \times 10^{-4}$
3-lvl, approach 2	C_{ap2}	2000	99	$-0.0006 - j0.0055$	$2.0466 \times 10^{-2} - j1.1210 \times 10^{-2}$
3-lvl, approach 3	C_{ap2}	0.01	1	$0.0085 - j0.0016$	$-2.6062 \times 10^{-11} + 9.0802 \times 10^{-12}$
3-lvl, approach 3	C_{ap2}	2	1	$-0.0013 - j0.0057$	$-6.1649 \times 10^{-9} + j1.1410 \times 10^{-3}$
3-lvl, approach 3	C_{ap2}	20	1	$-0.0006 - j0.0051$	$1.9767 \times 10^{-2} - 1.1712 \times 10^{-2}$

Table 4.1: The results of the different DCIM methods applied only on the path indicated. As the test, $\tilde{G}^A_{xx}$ data of the geometry shown in Fig.4.17, after the subtraction of the SWP, is used. For all the cases, 100 data points are taken.

As can be seen in Table 4.1, the 2-level approach cannot capture the contribution of the branch point, since the value of $\alpha_1 + \alpha_2$ is relatively high. For the 3-level DCIM approaches the value of $\alpha_1 + \alpha_2$ is smaller, therefore they can capture the contribution of the branch point, as long as the second bound for the approximation, T_{02}, is not very high. The numerical results of the whole DCIM method applied to different geometries can be seen in the next section.

4.3 Numerical Examples

In this section numerical examples of layered structures will be given to show the robustness and the efficiency of the 3-level approximation method. Since all the 3 approaches give the same results in most of the cases, only the results of the second approach are shown in the examples, unless otherwise is indicated.

4.3.1 Surface Wave Pole very close to branch point

This example is given in [29]. The geometry seen in Fig.4.18 is studied at $f = 4.075GHz$. The locations of the observation and the source (HED) points are at the interface between the air and the dielectric layer ($z = h = 0$).

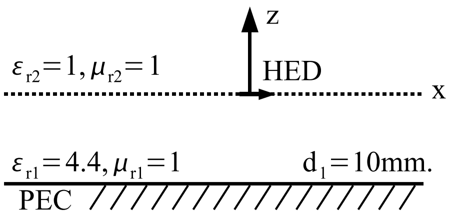

Figure 4.18: Geometry of the example: SWP very close to branch point and no SWP.

For this geometry the free space wave vector is $k_0 = 85.3466m^{-1}$. The TE-mode surface wave pole is found to be at $k_{sw,TE} = 85.3489 = 1.00001440k_0$ and the TM-mode surface wave pole is found to be at $k_{sw,TM} = 126.1984 = 1.478658k_0$. For this example, in 2-level approximation, the following constants are used: $T_{01} = 100$ and $T_{02} = 3$, number of samples=100 for both of the paths, and the number of exponentials used are $N_1 = 6$ and $N_2 = 7$ for vector potential and $N_1 = 5$ and $N_2 = 6$ for scalar potential Green's functions.

In the 3-level approximation the following constants are used: $T_{01} = 100$, $T_{02} = 200$ and $T_{03} = 99$, number of samples are 50, 100 and 100 for C_{ap1}, C_{ap2} and C_{ap3} respectively. The number of exponentials used are $N_1 = 4$, $N_2 = 5$ and $N_3 = 4$ for vector potential and $N_1 = 4$, $N_2 = 7$ and $N_3 = 5$ for scalar potential Green's functions. The results of numerical integration and both the 2 and 3-level DCIMs are plotted below in Figs.4.19 and 4.20, for the vector and the scalar potentials, respectively.

Since the TE-mode surface wave pole is very close to the branch point, the contribution from the branch point becomes crucial and the 2-level DCIM gives errors for large ρ values.

4.3.2 No surface wave poles

The geometry seen in Fig.4.18 is studied at $f = 3GHz$ [29]. The locations of the observation and the source (HED) points are at the interface between the air and the dielectric layer ($z = h = 0$). For this geometry the free space wave vector is $k_0 = 62.8318m^{-1}$. There is no TE-mode surface wave pole at $f = 3GHz$ and the TM-mode surface wave pole is found to be at $k_{sw,TM} = 76.9527 = 1.4786k_0$. For this example, in 2-level approximation, the following constants are used: $T_{01} = 100$ and $T_{02} = 3$, number of samples=100 for both of the paths, and the number of exponentials used are $N_1 = 6$ and $N_2 = 5$ for vector potential and $N_1 = 5$ and $N_2 = 4$ for scalar potential Green's functions. In the 3-level approximation the following constants are used: $T_{01} = 100$, $T_{02} = 200$ and $T_{03} = 99$, number of samples are 50, 100 and 100 for C_{ap1}, C_{ap2} and C_{ap3} respectively. The number of exponentials used are $N_1 = 3$, $N_2 = 3$ and $N_3 = 3$ for vector potential and $N_1 = 3$, $N_2 = 3$ and $N_3 = 4$ for scalar potential Green's functions. The results of numerical integration and both the 2 and 3-level DCIM are plotted below in Figs.4.21 and 4.22.

Since there are no SWPs for the vector potential case, the contribution of the branch point determines the far-field behavior. Since the 2-level DCIM cannot capture the contribution of the branch point, it gives errors for large values of ρ.

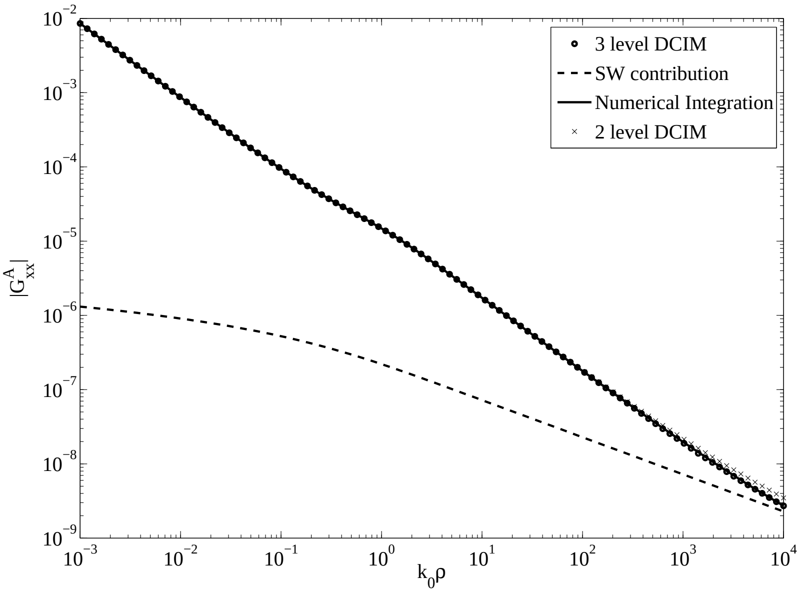

Figure 4.19: Magnitude of vector potential of the geometry in Fig.4.18 at $f = 4.075GHz$.

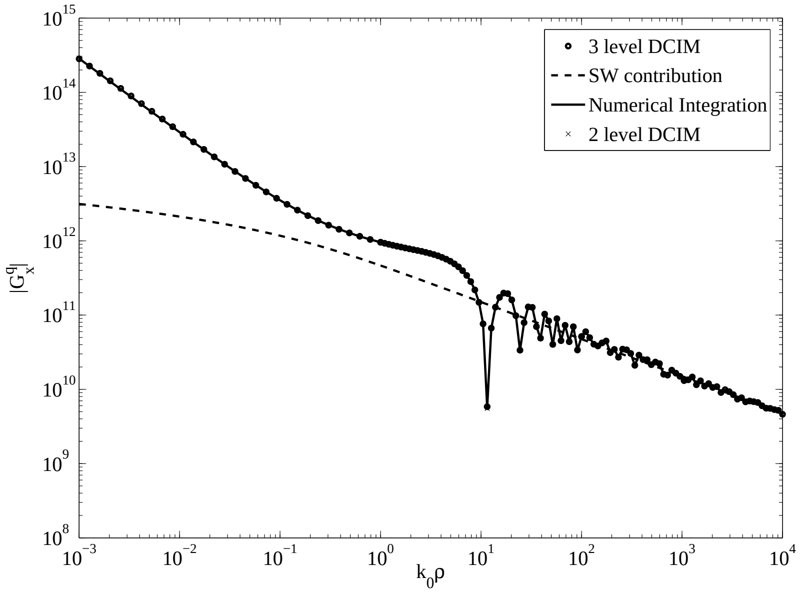

Figure 4.20: Magnitude of scalar potential of the geometry in Fig.4.18 at $f = 4.075GHz$.

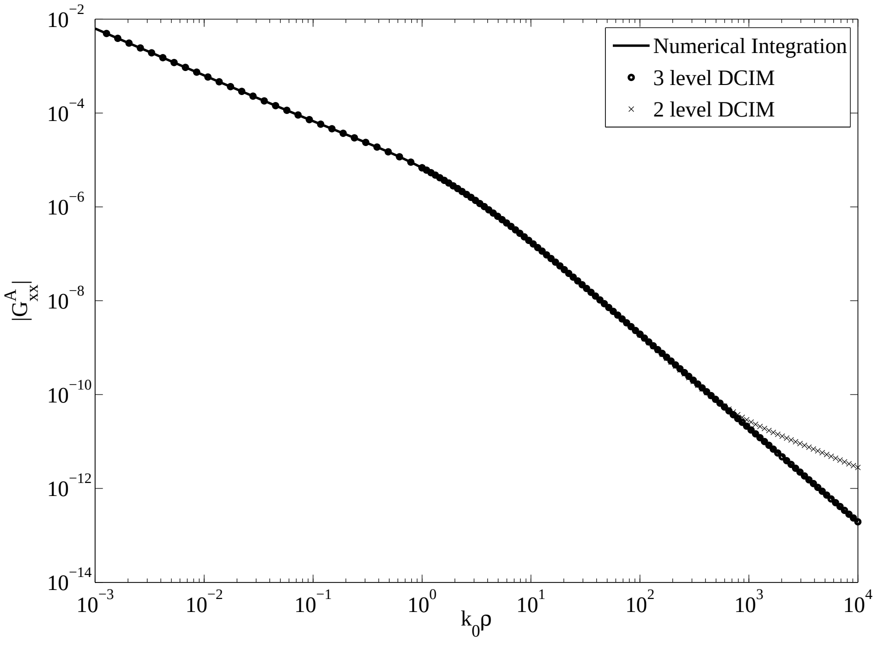

Figure 4.21: Magnitude of vector potential of the geometry in Fig.4.18 at $f = 3GHz$.

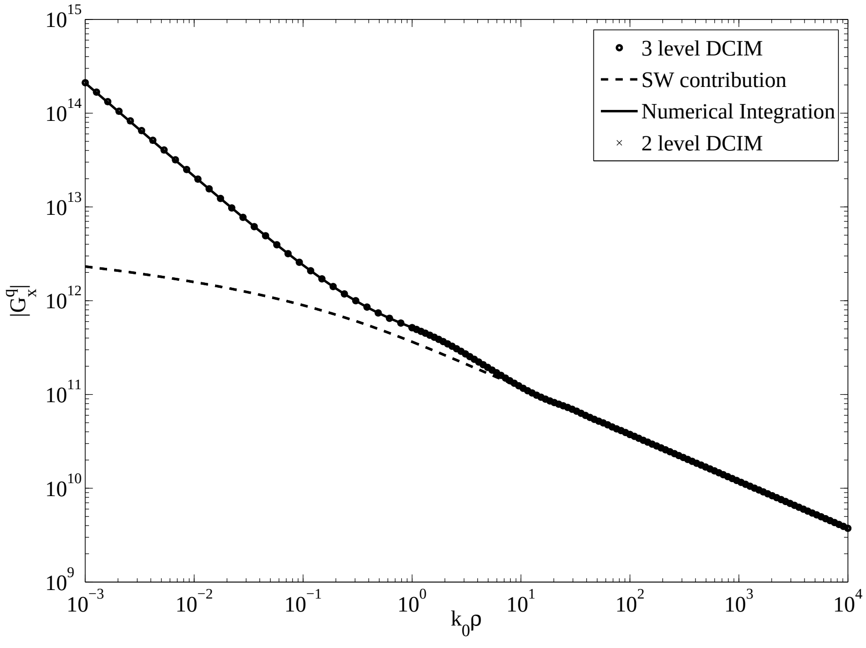

Figure 4.22: Magnitude of scalar potential of the geometry in Fig.4.18 at $f = 3GHz$.

4.3.3 A lossy, PEC backed material

This example is given in [24]. The geometry seen in Fig.4.23 is studied at $f = 10GHz$. The locations of the observation and the source (HED) points are at the interface between the air and the dielectric layer ($z = h = 0$).

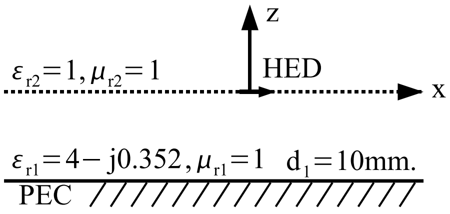

Figure 4.23: Geometry of the example: lossy, PEC-backed slab.

For this geometry the free space wave vector is $k_0 = 209.4395m^{-1}$. For this example, there are two TM-mode surface wave poles found at $k_{sw,TM,1} = 213.2321 - j4.0539 = (1.0181 - j0.0193)k_0$, and $(k_{sw,TM,2} = 392.9631 - j19.0667 = (1.8762 - j0.0910)k_0$, and one TE-mode surface wave pole found at $(k_{sw,TE,1} = 342.7213 - 19.8548j = (1.6363 - j0.0947)k_0$. For this example, in 2-level approximation, the following constants are used: $T_{01} = 100$ and $T_{02} = 3$, number of samples=100 for both of the paths, and the number of exponentials used are $N_1 = 3$ and $N_2 = 4$ for vector potential and $N_1 = 4$ and $N_2 = 4$ for scalar potential Green's functions. In the 3-level approximation the following constants are used: $T_{01} = 100$, $T_{02} = 200$ and $T_{03} = 99$, number of samples are 50, 100 and 100 for C_{ap1}, C_{ap2} and C_{ap3} respectively. The number of exponentials used are $N_1 = 3$, $N_2 = 3$ and $N_3 = 5$ for vector potential and $N_1 = 3$, $N_2 = 3$ and $N_3 = 7$ for scalar potential Green's functions. The results of numerical integration, 2 and 3-level DCIM are plotted below in Figs.4.24 and 4.25.

Since the SWPs have an imaginary part, the contribution of the SWPs disappears for large ρ values due to the exponential decay of the surface waves. As a result, the contribution of the branch point determines the far-field behavior, therefore it becomes crucial to capture the contribution of the branch point. As seen in the results, the 2-level approach generates results with a decay of $1/\rho$ for large ρ values, since it cannot capture the contribution of the branch point, as discussed in Section 4.2.3. In the 3-level case, the method can capture the contribution of the branch point, and as the result, it generates results with a decay

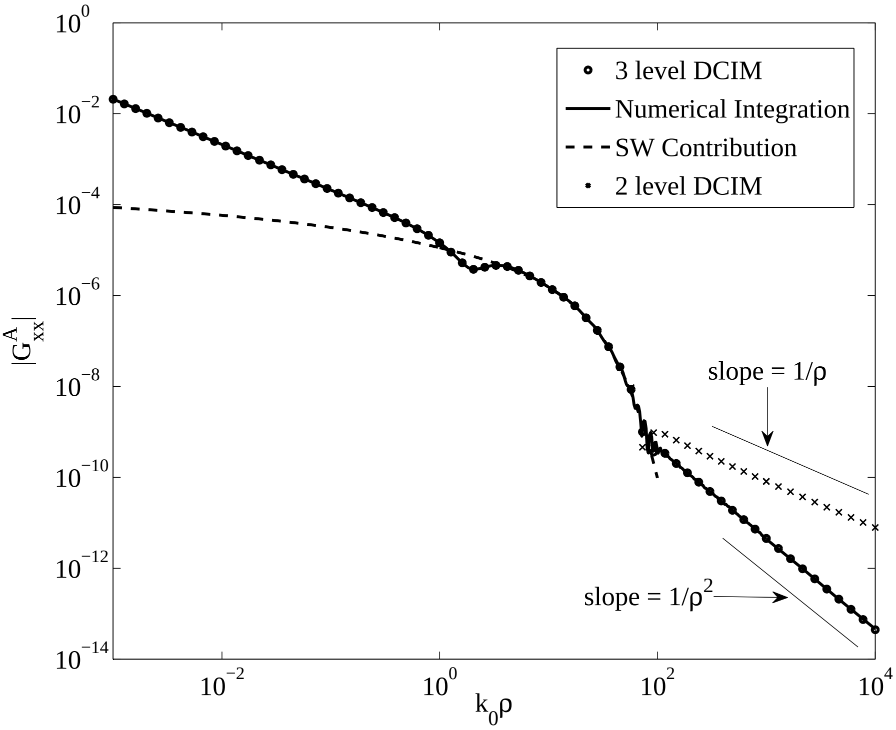

Figure 4.24: Magnitude of vector potential of the geometry in Fig.4.23 at $f = 10GHz$.

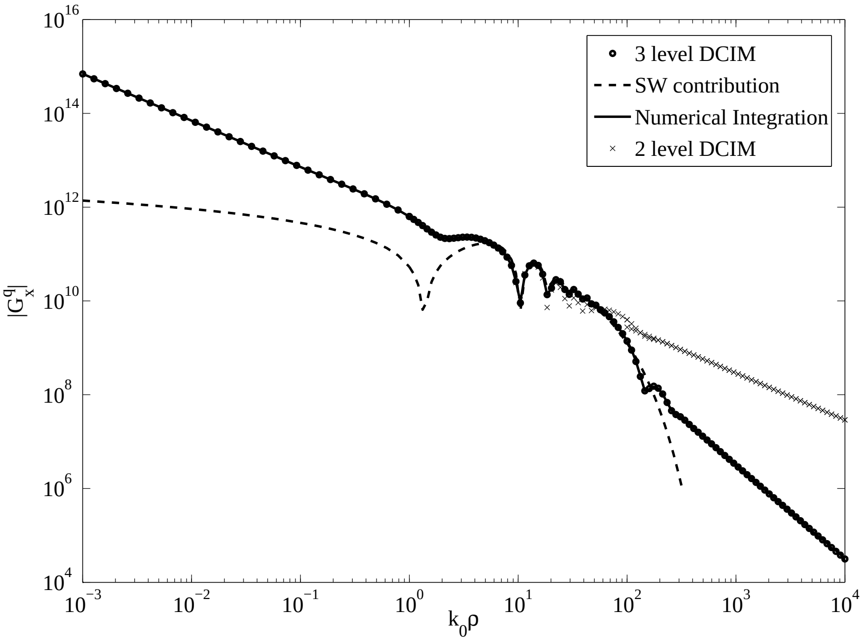

Figure 4.25: Magnitude of scalar potential of the geometry in Fig.4.23 at $f = 10GHz$.

of $1/\rho^2$ for large ρ values. This behavior can be seen in Fig.4.24, where two lines with the indicated slopes are plotted. The situation is the same for the other examples, when a SWP with imaginary part is observed.

4.3.4 A combination of lossy and lossless materials in a PEC backed geometry

The geometry seen in Fig.4.26 is studied at $f = 10GHz$. The locations of the observation and the source (HED) points are at the interface between the air and the dielectric layer ($z = h = 0$).

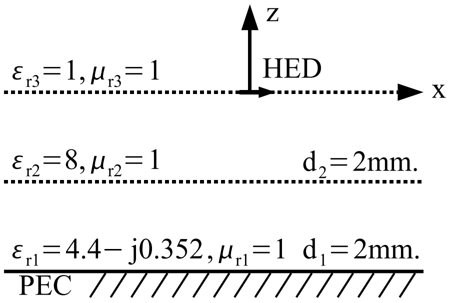

Figure 4.26: Geometry of the example: both lossy and lossless materials in a PEC-backed geometry.

For this geometry the free space wave vector is $k_0 = 209.4395m^{-1}$. The TE-mode surface wave pole is found to be at $k_{sw,TE} = 281.8020 - j2.5031 = (1.3455 - j0.0119)k_0$ and the TM-mode surface wave pole is found to be at $k_{sw,TM} = 355.5048 - j11.7667 = (1.6974 - j0.0561)k_0$. For this example, in 2-level approximation, the following constants are used: $T_{01} = 100$ and $T_{02} = 3$, number of samples=100 for both of the paths, and the number of exponentials used are $N_1 = 4$ and $N_2 = 4$ for vector potential and $N_1 = 4$ and $N_2 = 5$ for scalar potential Green's functions. In the 3-level approximation the following constants are used: $T_{01} = 100$, $T_{02} = 300$ and $T_{03} = 99$, number of samples are 50, 100 and 100 for C_{ap1}, C_{ap2} and C_{ap3} respectively. The number of exponentials used are $N_1 = 3$, $N_2 = 4$ and $N_3 = 4$ for vector potential and $N_1 = 3$, $N_2 = 5$ and $N_3 = 5$ for scalar potential Green's functions. The results of numerical integration and the 2 and 3-level DCIM are plotted below in Figs.4.27 and 4.28.

The solution is very similar to the case of PEC backed lossy structure. Since the SWP

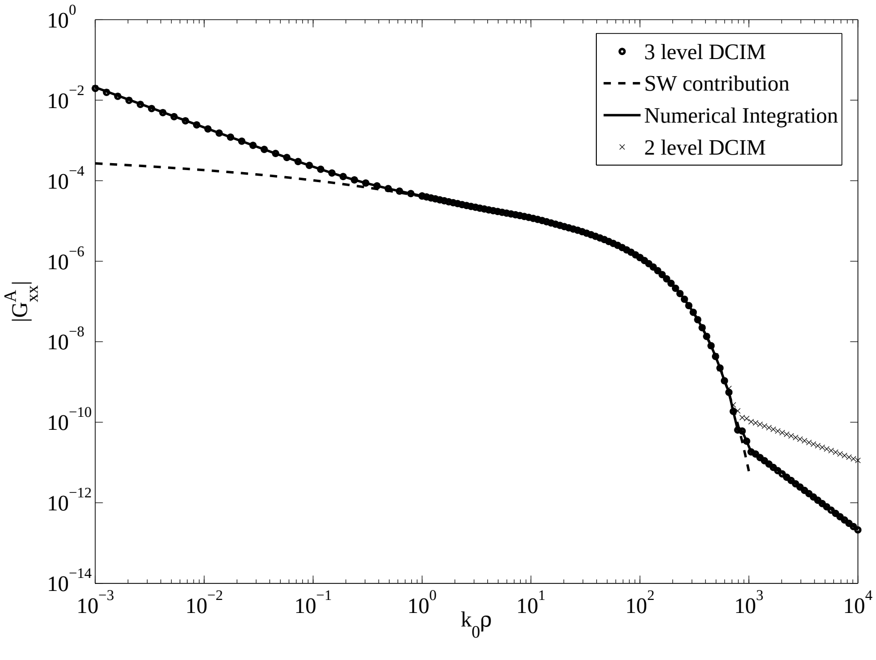

Figure 4.27: Magnitude of vector potential of the geometry in Fig.4.26 at $f = 10GHz$.

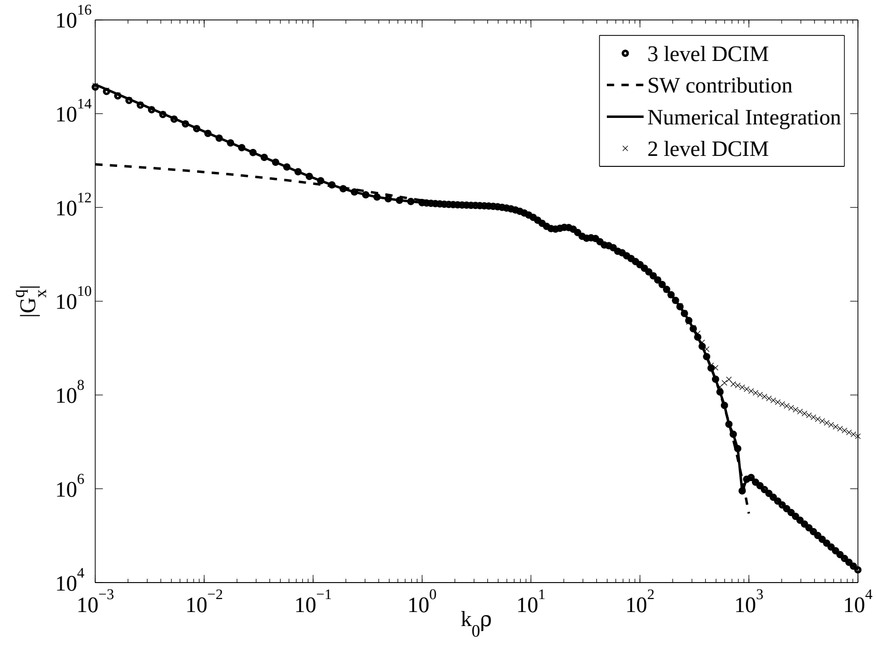

Figure 4.28: Magnitude of scalar potential of the geometry in Fig.4.26, at $f = 10GHz$.

contribution decay exponentially the branch point contribution determines the behavior when $\rho \to \infty$. Since the contribution cannot be captured by the 2-level approach, it gives errors in the far field region, as discussed in the previous example.

4.3.5 A lossy slab in air

The geometry seen in Fig.4.29 is studied at $f = 4GHz$. The locations of the observation and the source (HED) points are at the interface between the air and the upper boundary of the dielectric layer ($z = z' = 0$).

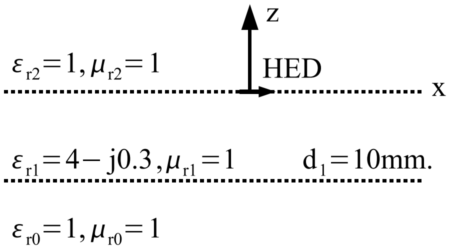

Figure 4.29: Geometry of the example: a lossy material in air.

For this geometry the free space wave vector is $k_0 = 83.7758m^{-1}$. The TE-mode surface wave pole is found to be at $k_{sw,TE} = 117.0866 - j4.6437 = (1.3976 - j0.0554)k_0$ and the TM-mode surface wave pole is found to be at $k_{sw,TM} = 89.1354 - j0.4889 = (1.0640 - j0.0058)k_0$. For this example, in 2-level approximation, the following constants are used: $T_{01} = 100$ and $T_{02} = 2$, number of samples=100 for both of the paths, and the number of exponentials used are $N_1 = 4$ and $N_2 = 3$ for vector potential and $N_1 = 4$ and $N_2 = 4$ for scalar potential Green's functions. In the 3-level approximation the following constants are used: $T_{01} = 100$, $T_{02} = 200$ and $T_{03} = 99$, number of samples are 50, 100 and 100 for C_{ap1}, C_{ap2} and C_{ap3} respectively. The number of exponentials used are $N_1 = 3$, $N_2 = 5$ and $N_3 = 5$ for vector potential and $N_1 = 3$, $N_2 = 5$ and $N_3 = 5$ for scalar potential Green's functions. The results of numerical integration and the 2 and 3-level DCIM are plotted below in Figs.4.30 and 4.31.

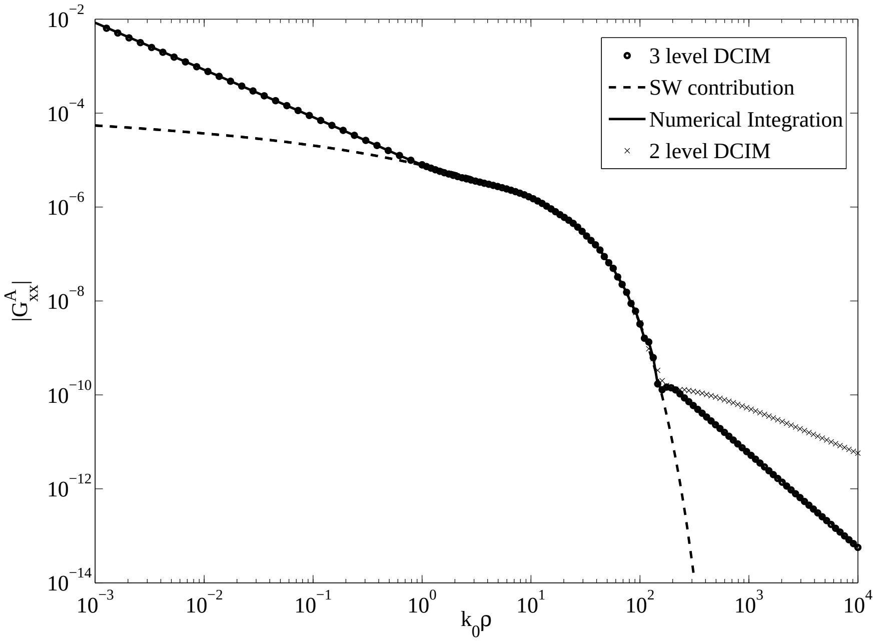

Figure 4.30: Magnitude of vector potential of the geometry in Fig.4.29 at $f = 4GHz$.

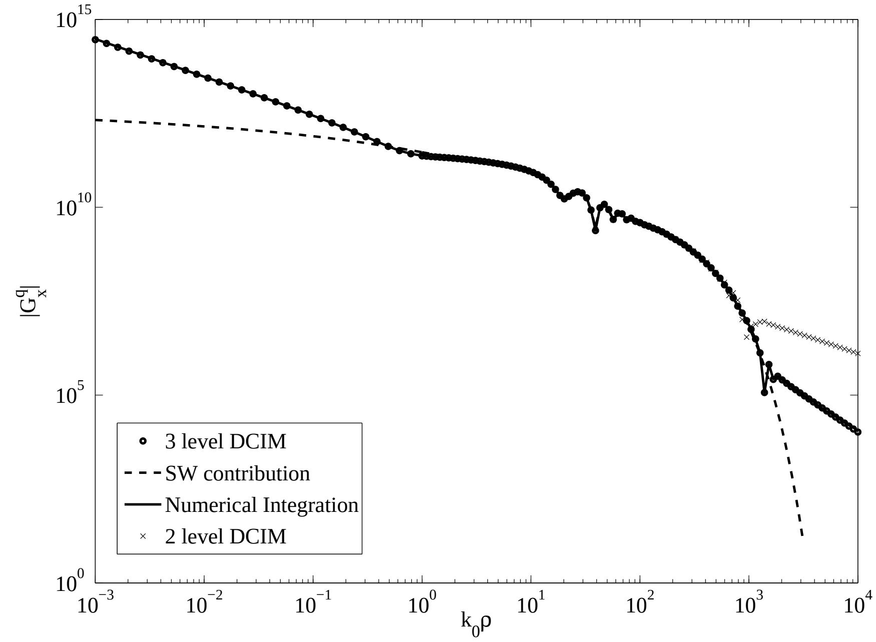

Figure 4.31: Magnitude of scalar potential of the geometry in Fig.4.29 at $f = 4GHz$.

4.3.6 A multi-layered structure in air

This example is taken from [82]. The geometry seen in Fig.4.32 is studied at $f = 47.393GHz$. The location of the source point is $2.5mm$ above the uppermost slab ($h = 2.5mm$) and the results are obtained along a line as shown in Fig.4.32.

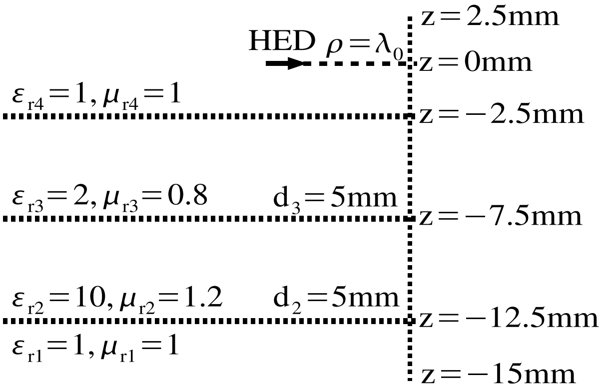

Figure 4.32: Geometry of the example: A multi-layered structure in air. The observation locations are taken to be on the line, where the distance between the line and the source point is $\lambda_0 = 6.33mm$.

For this geometry the free space wave vector is $k_0 = 992.5966m^{-1}$. The TE-mode surface wave poles are found to be at $k_{sw,TE1} = 1121.5166m^{-1} = 1.12k_0$, $k_{sw,TE2} = 1245.4442m^{-1} = 1.25k_0$ and the TM-mode surface wave poles are found to be at $k_{sw,TM1} = 1021.1547m^{-1} = 1.03k_0$ and $.k_{sw,TM2} = 1181.4495m^{-1} = 1.19k_0$. The results obtained by numerical integration and 3-level DCIM, along the vertical line seen in Fig.4.29 ($z = -15mm$ to $2.5mm$) can be seen in the figures below.

Since the results are obtained on the vertical line, the number of exponentials fitted in the 3-level approximation is changed for each data point on the line, since a different spectral domain Green's function is obtained. Therefore the tolerance values for the GPOF are set to be $tol_1 = 10^-4$, $tol_1 = 10^-2$ and $tol_1 = 10^-4$. As can be seen in the results, the 3-level approach gives excellent results for this case also.

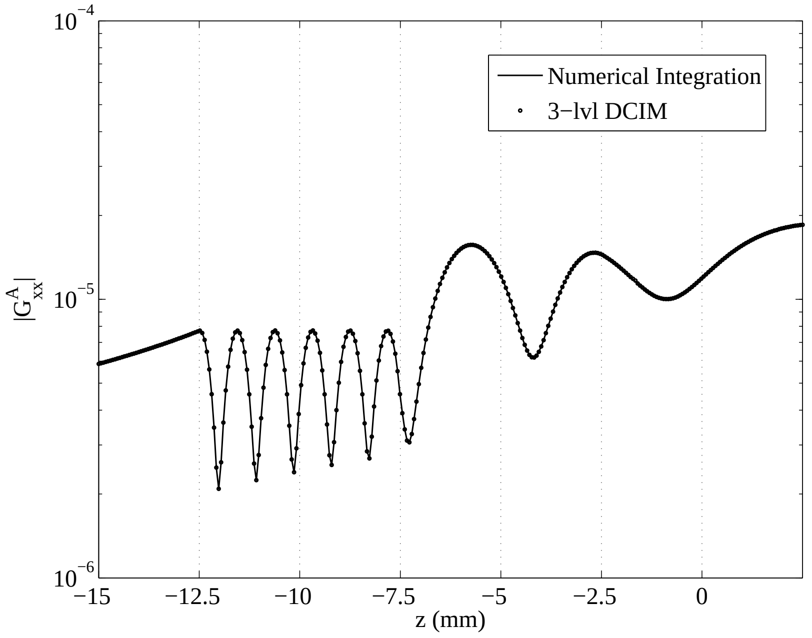

Figure 4.33: Magnitude of vector potential of the geometry in Fig.4.32 at $f = 47.393GHz$.

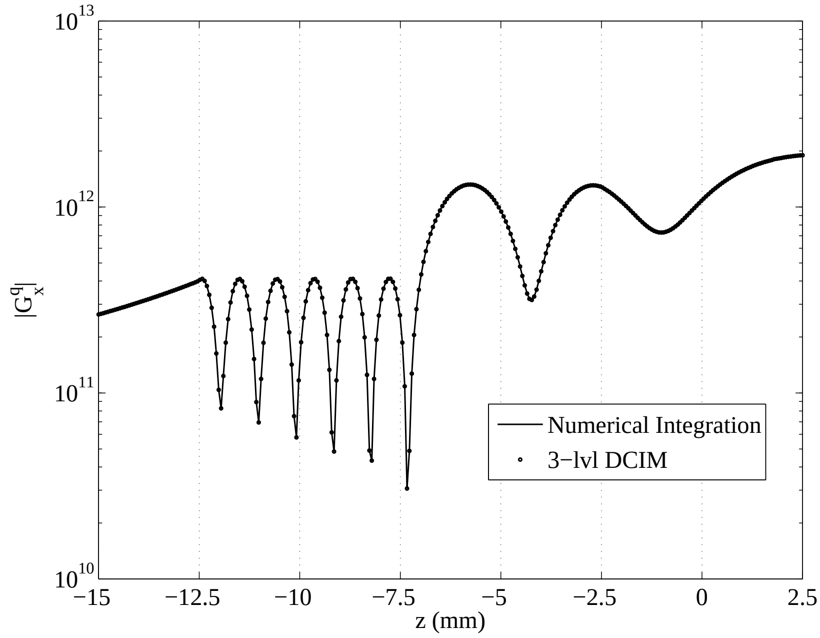

Figure 4.34: Magnitude of scalar potential of the geometry in Fig.4.32 at $f = 47.393GHz$.

4.3.7 A PEC backed LHM

The geometry seen in Fig.4.35 is studied at $f = 1GHz$. The locations of the observation and the source (HED) points are at the interface between the air and the dielectric layer ($z = h = 0$).

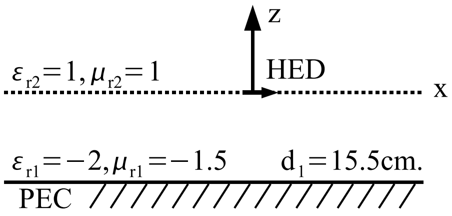

Figure 4.35: Geometry of the example: A PEC backed LHM slab.

For this geometry the free space wave vector is $k_0 = 20.9439m^{-1}$. The TE-mode surface wave poles are found to be at $k_{sw,TE1} = 21.1320m^{-1} = 1.0089k_0$, $k_{sw,TE2} = 25.3469m^{-1} = 1.2102k_0$ and the TM-mode surface wave pole is found to be at $k_{sw,TM} = 34.4150m^{-1} = 1.6431k_0$. The parameters used in the 3-level DCIM, approach 3, are: $T_{01} = 100$, $T_{02} = 2$ and $T_{03} = 1$, number of samples are 50, 100 and 100 for C_{ap1}, C_{ap2} and C_{ap3} respectively. The number of exponentials used are $N_1 = 4$, $N_2 = 4$ and $N_3 = 5$ for vector potential and $N_1 = 5$, $N_2 = 4$ and $N_3 = 5$ for scalar potential Green's functions. The results of numerical integration and the 3-level DCIM are plotted below in Figs.4.36 and 4.37.

As seen in the results, the 3-level DCIM can approximate geometries containing LHMs.

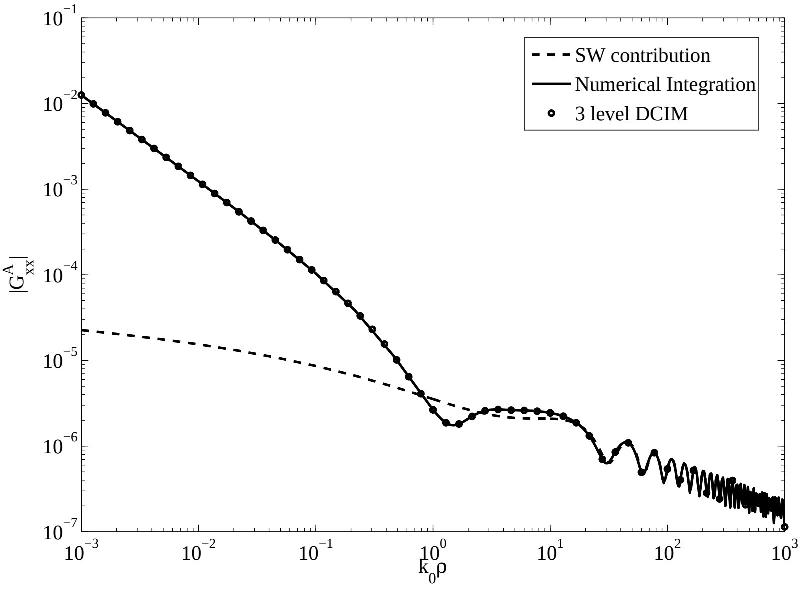

Figure 4.36: Magnitude of vector potential of the geometry in Fig.4.35 at $f = 1GHz$.

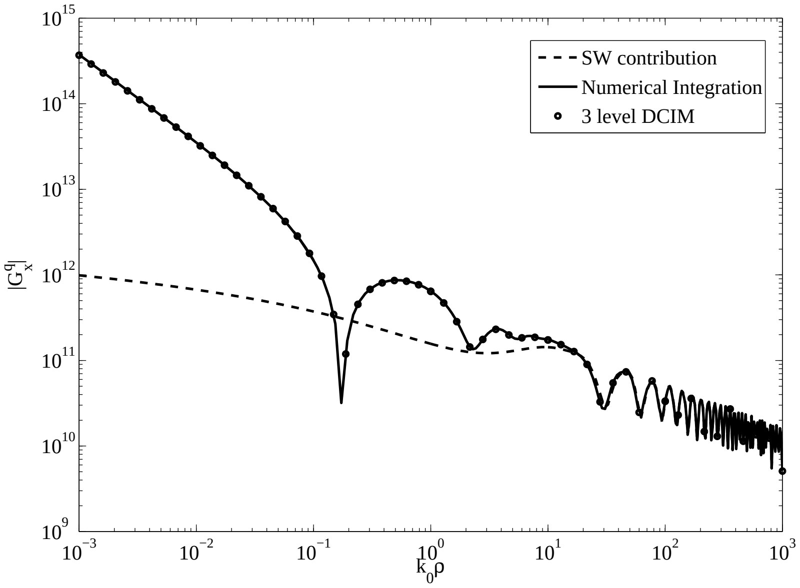

Figure 4.37: Magnitude of scalar potential of the geometry in Fig.4.35 at $f = 1GHz$.

4.3.8 A Lossy Slab of LHM in air

The geometry seen in Fig.4.38 is studied at $f = 1GHz$. The locations of the observation and the source (HED) points are at the interface between the air and the dielectric layer ($z = h = 0$).

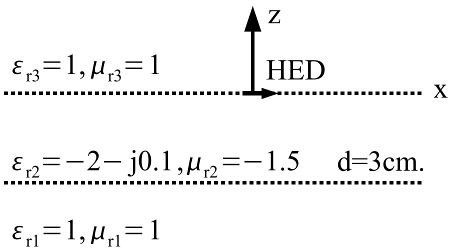

Figure 4.38: Geometry of the example: A lossy LHM slab in air.

For this geometry the free space wave vector is $k_0 = 20.9439m^{-1}$. The TE-mode surface wave pole is found to be at $k_{sw,TE} = (53.8399 - j0.2813)m^{-1} = (2.5706 - j0.0134)k_0$ and the TM-mode surface wave pole is found to be at $k_{sw,TM} = (39.8186 - j1.9000)m^{-1} = (1.9011 - 0.09071)k_0$. The parameters used in the 3-level DCIM, approach 3, are: $T_{01} = 100$, $T_{02} = 2$ and $T_{03} = 1$, number of samples are 50, 100 and 100 for C_{ap1}, C_{ap2} and C_{ap3} respectively. The number of exponentials used are $N_1 = 3$, $N_2 = 4$ and $N_3 = 4$ for vector potential and $N_1 = 4$, $N_2 = 4$ and $N_3 = 6$ for scalar potential Green's functions. The results of numerical integration and the 3-level DCIM are plotted below in Figs.4.39 and 4.40.

As seen in the results, the 3-level DCIM can approximate geometries containing lossy LHMs. As in the case of RHMs, the contribution of the branch point is captured by the 3-level approach in LHMs.

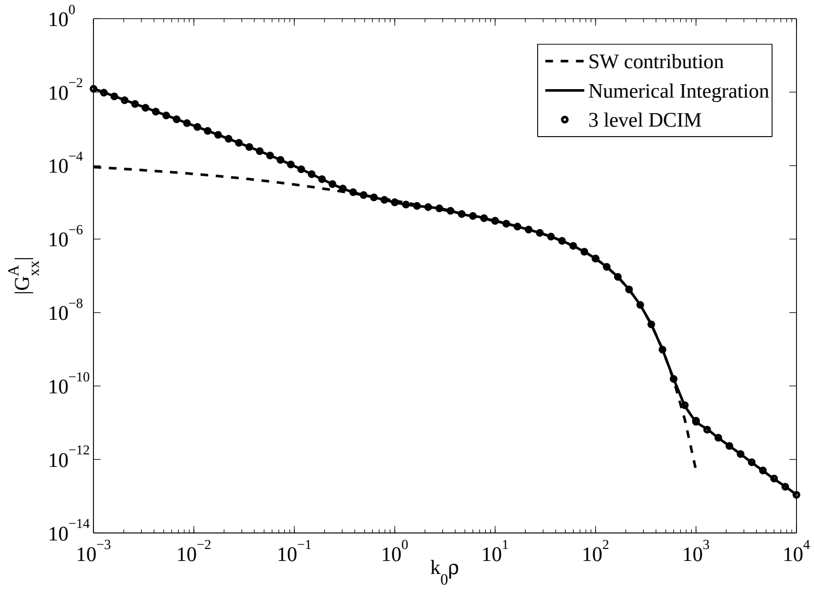

Figure 4.39: Magnitude of vector potential of the geometry in Fig.4.38 at $f = 1GHz$.

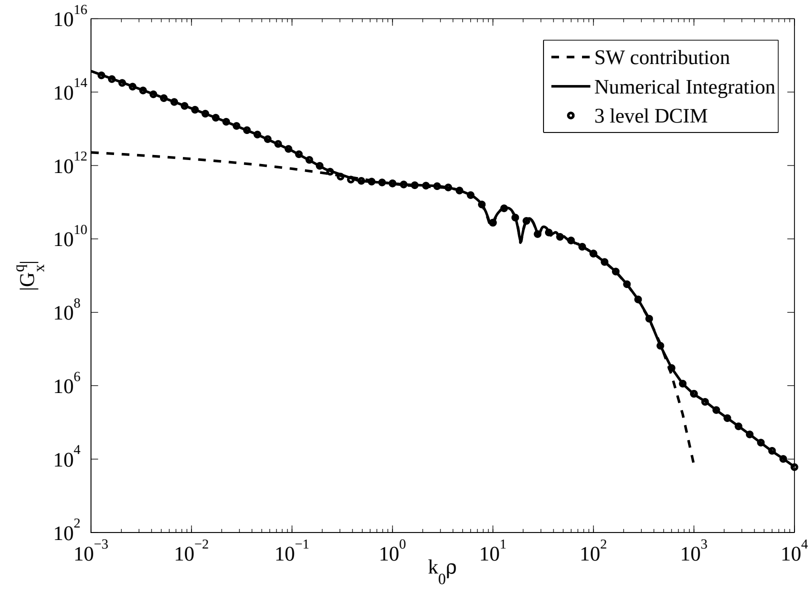

Figure 4.40: Magnitude of scalar potential of the geometry in Fig.4.38 at $f = 1GHz$.

4.3.9 A combination of RHM and LHM in a PEC backed geometry

The geometry seen in Fig.4.41 is studied at $f = 1GHz$. The location of the source point is $1mm$ above the uppermost slab ($h = 1mm$) and the results are taken on the interface between the LHM and the RHM ($z = -11mm$).

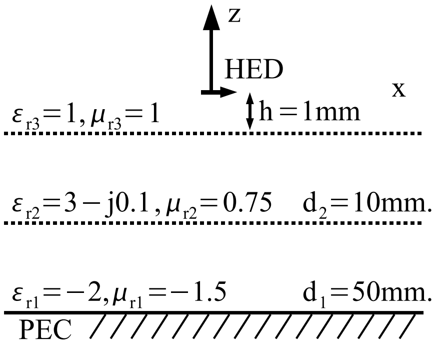

Figure 4.41: Geometry of the example: A combination of LHM and RHM in a PEC backed structure. The source point is at $h = 1mm$ and the observation points are at the interface between regions 1 and 2.

For this geometry the free space wave vector is $k_0 = 20.9439m^{-1}$. The TE-mode surface wave pole is found to be at $k_{sw,TE} = (23.0402 - j0.2034)m^{-1} = (1.1001 - j0.0097)k_0$ and the TM-mode surface wave pole is found to be at $k_{sw,TM} = (-64.7608 - j2.24499)m^{-1} = (-3.0921 - j0.1071)k_0$. The results obtained by numerical integration and 3-level DCIM, approach 3, along the interface between the LHM and the RHM ($z = -11mm$) can be seen below. The parameters used for the approximation are: $T_{01} = 100$, $T_{02} = 3$ and $T_{03} = 1$, number of samples are 50, 100 and 100 for C_{ap1}, C_{ap2} and C_{ap3} respectively. The number of exponentials used are $N_1 = 5$, $N_2 = 5$ and $N_3 = 5$ for vector potential and $N_1 = 5$, $N_2 = 6$ and $N_3 = 6$ for scalar potential Green's functions. The results of numerical integration and the 3-level DCIM are plotted below in Figs.4.42 and 4.43.

As can be seen in the results, the 3-level DCIM gives excellent results in near, intermediate and far field regions of the geometry, when the source and observation points are in different regions.

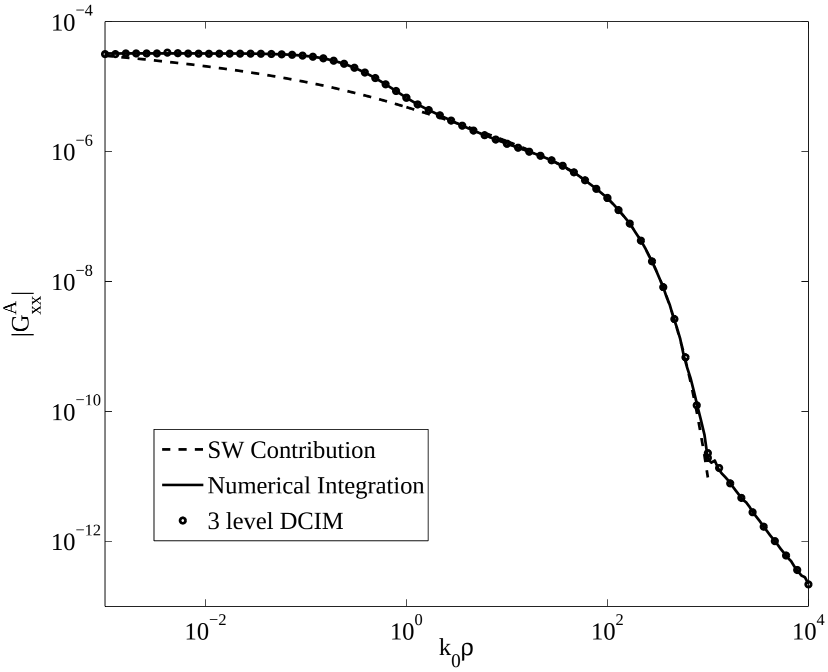

Figure 4.42: Magnitude of vector potential of the geometry in Fig.4.41 at $f = 1GHz$.

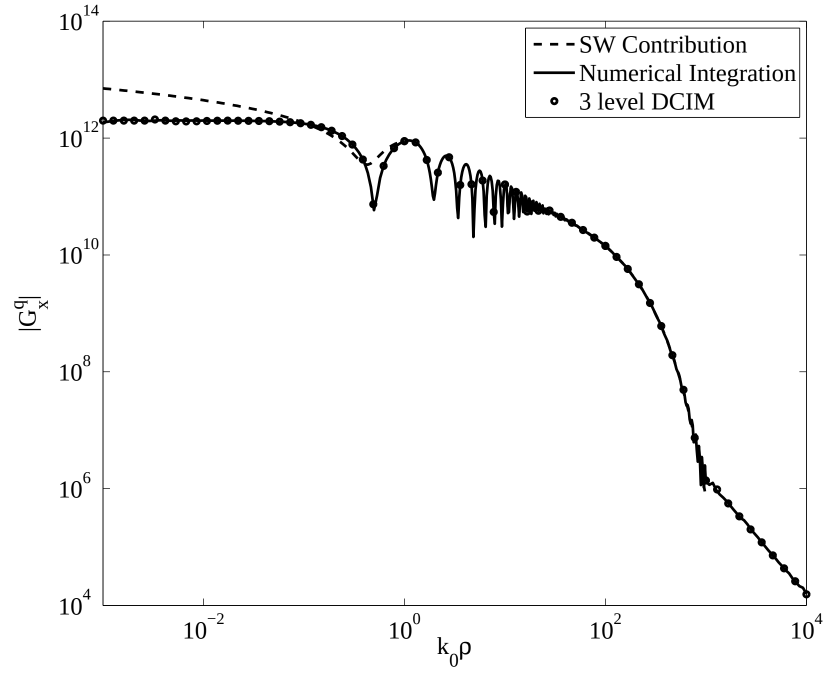

Figure 4.43: Magnitude of scalar potential of the geometry in Fig.4.41 at $f = 1GHz$.

4.3.10 A discussion on the perfect lens and numerical examples of lossy perfect lens

It is well known that, in conventional optical systems the resolution of the image is limited by the wavelength of the light. More specifically, the area on which the light is focussed cannot be less than a square wavelength of the light. This behavior of the traditional lenses is because of the fact that the evanescent spectrum ($k_\rho > k$) decays exponentially and as a result some of the information is lost and a point image (of a point source) cannot be obtained. The analytical solution to this problem is to use a slab of LHM with the constitutive parameters of $\varepsilon = -1$ and $\mu = -1$ in air, which was first proposed by Pendry in 2000 and discussed in detail in [46]. An example of the perfect lens configuration can be seen in Fig.4.44. As can be seen in Fig.4.44, the rays are negatively refracted and as the result, a slab of LHM with the constitutive parameters of $\varepsilon = -1$ and $\mu = -1$ is able to form an image both inside and outside the slab. Mathematically, to obtain a perfect image (the exact same image of the objects), all the wave vectors on the image location must be in phase and magnitude with the wave vectors of the object after passing through the perfect lens. To understand this fact, the generalized transmission and reflection coefficients must be analyzed. For the geometry seen in Fig. 4.44, the generalized reflection and transmission coefficients are found to be $\tilde{R} = 0$ and $\tilde{T}(k_z) = e^{jk_z d}$ respectively [46]. As can be seen easily, the generalized transmission coefficient makes it possible to transfer the phase information for the visible spectrum ($0 < k_\rho < k_0$) and the magnitude information for the evanescent spectrum ($k_0 < k_\rho$), which results in the exact same spectral domain information in the image location with the source. Therefore, one can conclude that a slab of LHM with the constitutive parameters of $\varepsilon = -1$ and $\mu = -1$ forms the exact same image of the object,

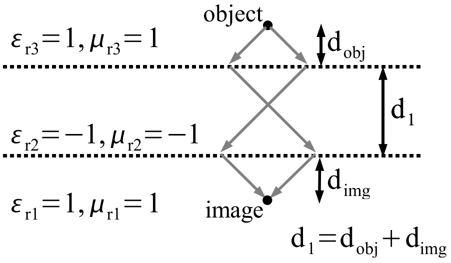

Figure 4.44: The ray directions in a perfect lens.

due to which such layered structures are called *the perfect lens.*

Here a study on the lossy perfect lens will be carried out to understand the effect of losses on the physics of the perfect lens. For this purpose, 2 different geometries are used. In the first one, effect of losses on the waves generated on the surface of the lossy perfect lens is investigated by changing the loss value. In the second one, the effect of losses on the image resolution is analyzed by comparing the changes seen in the spectral and spatial domain Green's functions as a function of loss.

Numerical example of lossy perfect lens: change of potential on the perfect lens surface depending on the loss.

To see the effect of losses on the wave components those are generated on the surface of the lossy perfect lens, the geometry seen in Fig.4.45 is studied at $f = 1GHz$. The locations of the observation and the source (HED) points are at the interface between the air and the upper boundary of the dielectric layer ($h = z = 0$). As can be seen in Fig.4.45, the perfect lens has a loss both in the permittivity and permeability values, i.e. κ. Below there are 4 examples for different values of κ, where the 3-level DCIM is applied to the G_{xx}^A of the geometry. The following constants are used in the 3-level DCIM, approach 3: $T_{01} = 100$, $T_{02} = 0.5$ and $T_{03} = 1$ and the number of exponentials used are as follows: for $\kappa = 1$, $N_1 = 4$, $N_2 = 4$ and $N_3 = 5$, for $\kappa = 0.1$, $N_1 = 10$, $N_2 = 6$ and $N_3 = 6$, for $\kappa = 0.01$, $N_1 = 12$, $N_2 = 6$ and $N_3 = 5$ and for $\kappa = 0.001$, $N_1 = 20$, $N_2 = 6$ and $N_3 = 4$. The results can be seen below in Figs.4.46-4.49.

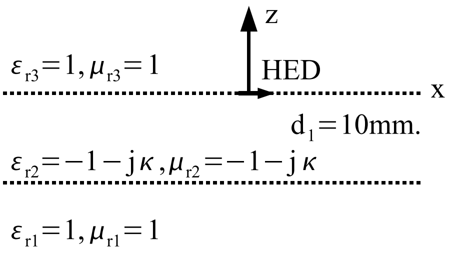

Figure 4.45: Geometry of the example: A lossy perfect lens in air with the object on the boundary between the lens and air.

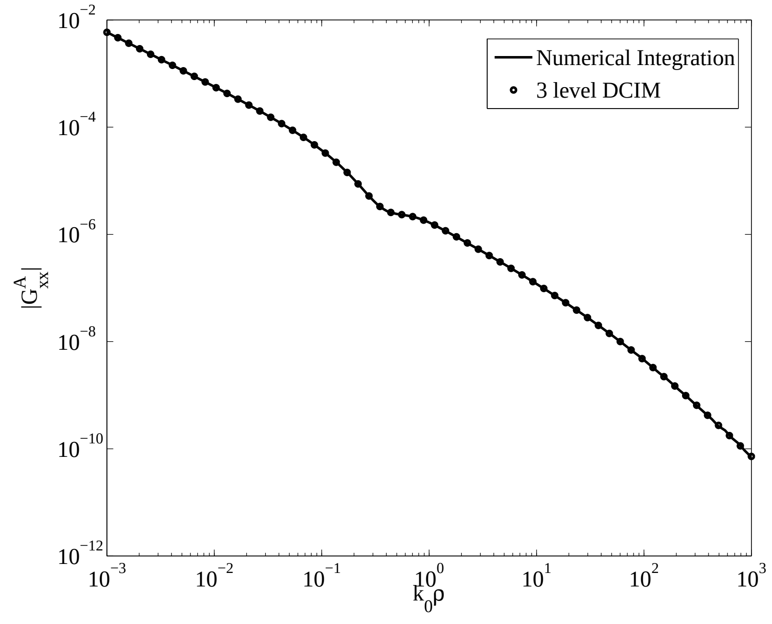

Figure 4.46: Magnitude of vector potential of the geometry in Fig.4.45 at $f = 1GHz$ and $\kappa = 1$.

As can be seen in the results, as the losses decrease, more wave components are seen on the surface and as the result, stronger interferences are observed on the surface of the perfect lens. Also, it is seen that the 3-level DCIM gives very good results for the case of lossy perfect lens.

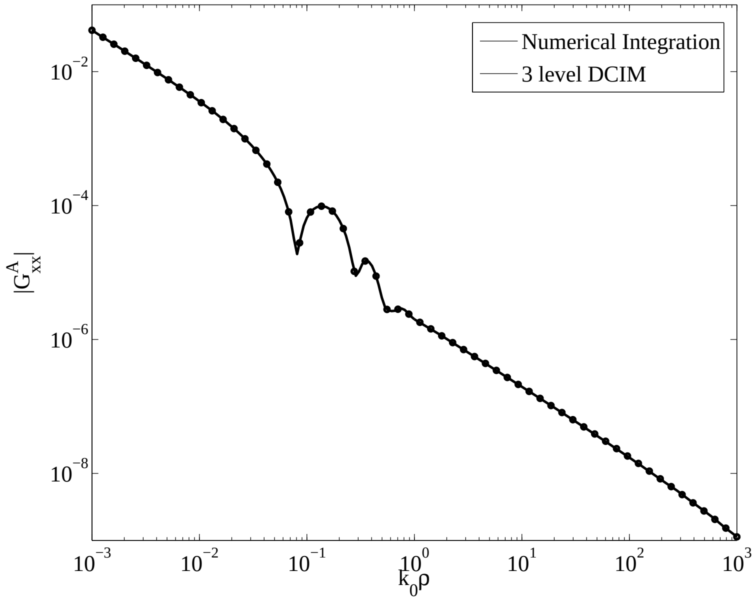

Figure 4.47: Magnitude of vector potential of the geometry in Fig.4.45 at $f = 1GHz$ and $\kappa = 0.1$.

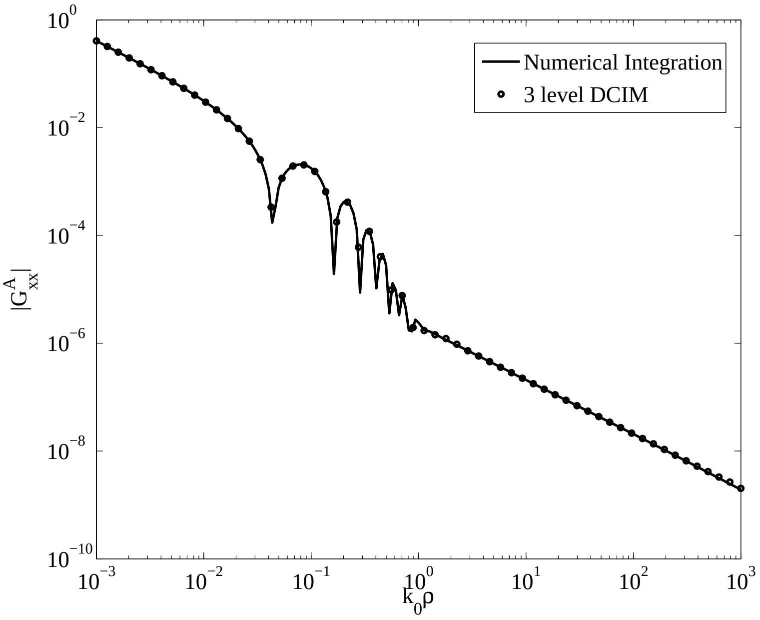

Figure 4.48: Magnitude of vector potential of the geometry in Fig.4.45 at $f = 1GHz$ and $\kappa = 0.01$.

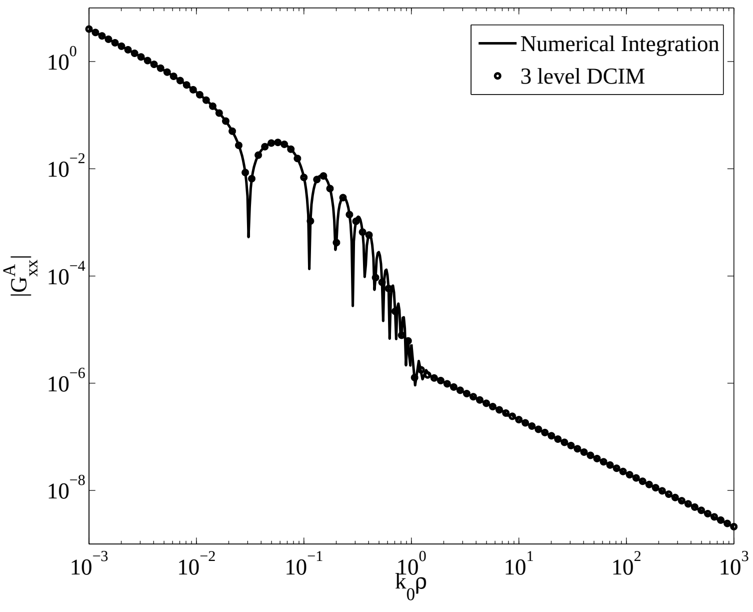

Figure 4.49: Magnitude of vector potential of the geometry in Fig.4.45 at $f = 1GHz$ and $\kappa = 0.001$.

Numerical example of lossy perfect lens: effect of losses on the resolution

To analyze the effect of losses to the image resolution, the geometry seen in Fig.4.50 is analyzed at $f = 1GHz$. The source (HED) is put $5mm$ above the surface of the lossy perfect lens and the results of the Green's functions, both in spectral and spatial domain, are collected at the image plane as shown in Fig.4.50 ($h = 5mm$ and $z = 20mm$). The

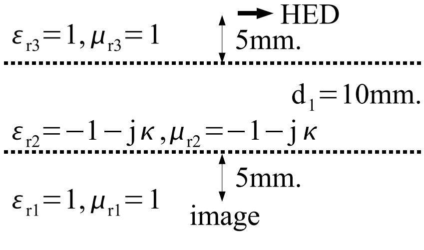

Figure 4.50: Geometry of the example: A lossy perfect lens in air with the object $5mm$ above the lens.

spectral and spatial Green's functions (for the vector potential) are plotted in Figs. 4.51 and 4.52, respectively.

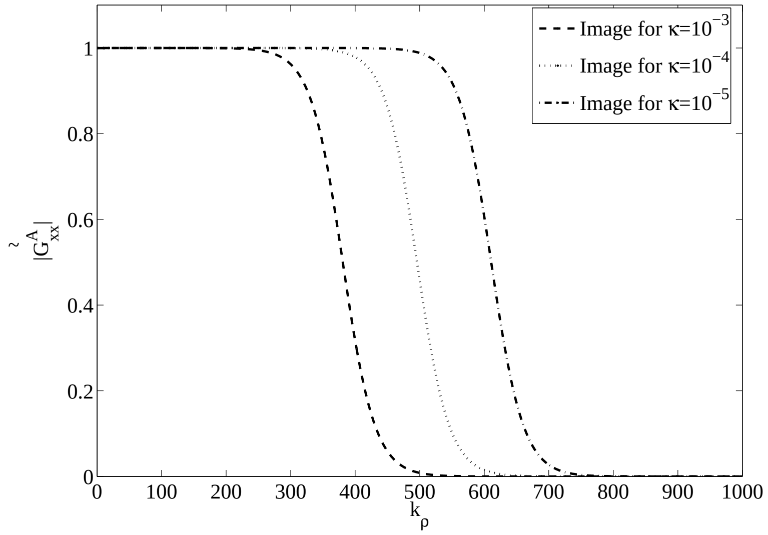

Figure 4.51: Spectral domain Green's function for the vector potential of the geometry shown in Fig. 4.50, for different values of κ.

For sake of eliminating crowded images, only the result of 3-level DCIM, 3rd approach for $\kappa = 10^{-4}$ is given. For the other values κ, the 3-level DCIM, 3rd approach gives the correct results. The following constants are used in the 3-level DCIM, approach 3: $T_{01} = 100$, $T_{02} = 0.5$ and $T_{03} = 1$ and the number of exponentials used are $N_1 = 7$, $N_2 = 4$ and $N_3 = 4$.

As can be seen in the results, when the loss of the perfect lens is small, a better image resolution is obtained, since an higher portion of the spectral domain Green's function is transferred to the image plane, as seen in Fig. 4.51.

4.3.11 A slab between two different semi-infinite dielectrics, at high frequency

The geometry seen in Fig.4.53 is studied at $f = 30GHz$. The locations of the observation and the source (HED) points are at the interface between the air and the upper boundary of the dielectric layer ($z = h = 0$). For this structure, since one of the surrounding media has a dielectric constant greater than the slab, there are no surface waves. The results of

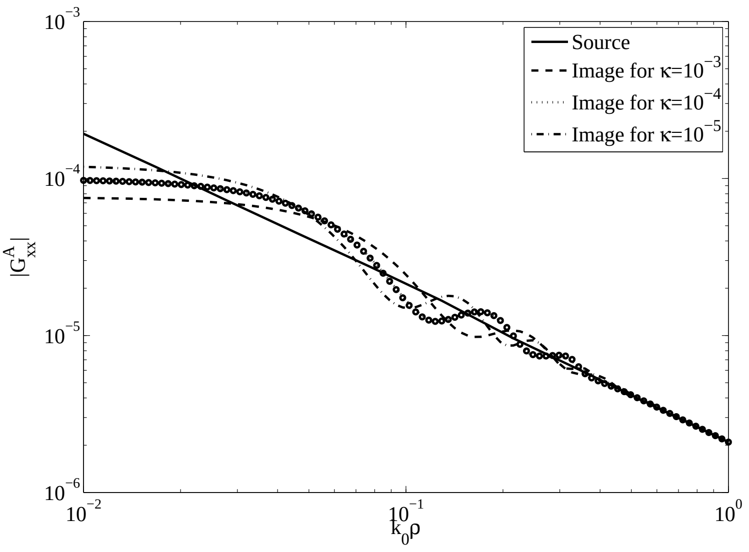

Figure 4.52: Spatial domain Green's function for the vector potential of the geometry shown in Fig. 4.50, for different values of κ. The circles are the result of 3-level DCIM.

numerical integration, and the 3-level DCIM are plotted below in Figs.4.54 and 4.55 below.

During the 3-level DCIM, as in the previous cases, VECT-FIT is run and 2 surface wave-like (cylindrical waves) poles are obtained for the G^A_{xx} and 4 surface wave-like (cylindrical waves) poles are obtained for the G^q_x between k_0 and $k_{max} = \sqrt{4}k_0 = 2k_0$. The values of the pole locations and the corresponding residues are tabulated below in Table 4.2. For this case the following parameters are used for the 3-level DCIM: $T_{01} = 100$, $T_{02} = 200$ and $T_{03} = 99$,

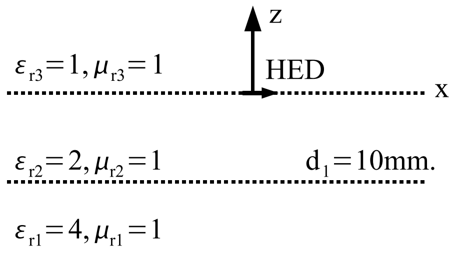

Figure 4.53: Geometry of the example: A slab between 2 different semi-infinite dielectric materials.

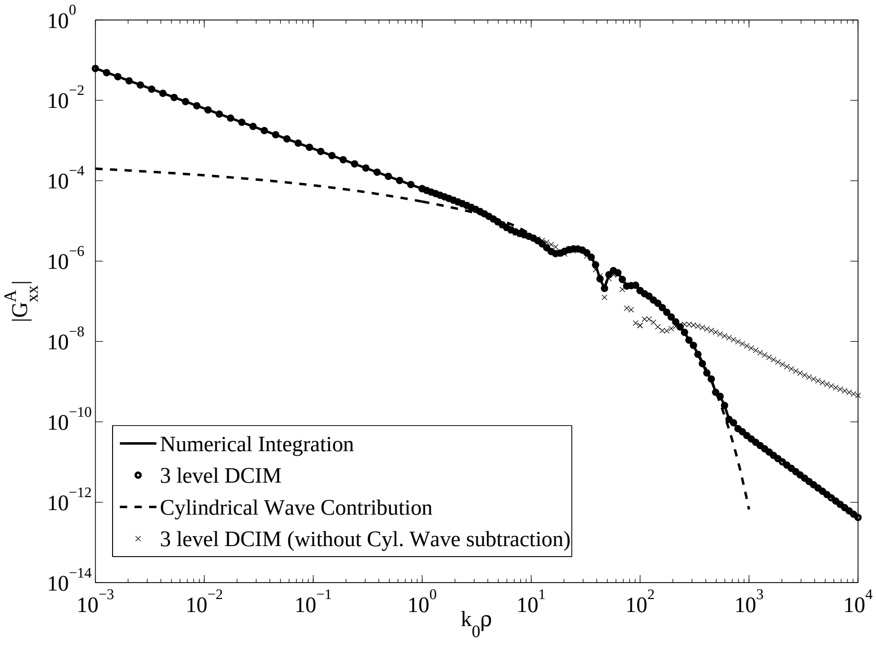

Figure 4.54: Magnitude of vector potential of the geometry in Fig.4.53 at $f = 30GHz$.

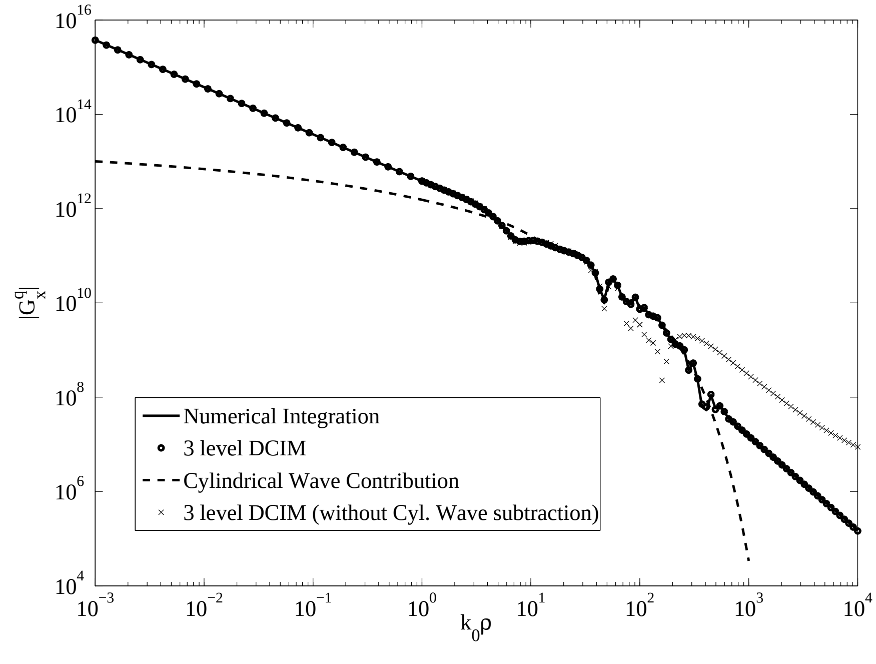

Figure 4.55: Magnitude of scalar potential of the geometry in Fig.4.53 at $f = 30GHz$.

number of samples are 50, 100 and 100 for C_{ap1}, C_{ap2} and C_{ap3} respectively. The number of exponentials used are $N_1 = 3$, $N_2 = 3$ and $N_3 = 8$ for vector potential and $N_1 = 3$, $N_2 = 3$ and $N_3 = 6$ for scalar potential Green's functions.In Figs.4.54 and 4.55, also the results obtained by 3-level DCIM, without subtracting the cylindrical wave contributions are plotted. For this case the following parameters are used: $T_{01} = 100$, $T_{02} = 200$ and $T_{03} = 99$, number of samples are 50, 100 and 100 for C_{ap1}, C_{ap2} and C_{ap3} respectively. The number of exponentials used are $N_1 = 3$, $N_2 = 9$ and $N_3 = 6$ for vector potential and $N_1 = 3$, $N_2 = 8$ and $N_3 = 5$ for scalar potential Green's functions.

G^A_{xx}		G^q_x	
Pole location	Residue	Pole location	Residue
(1.3493-j0.0127)k_0	$1.75 \times 10^{-2} + j5.15 \times 10^{-3}$	$(1.3497 - j0.0126)k_0$	$9.30 \times 10^{-3} + j3.52 \times 10^{-3}$
(1.1433-j0.0510)k_0	$7.47 \times 10^{-2} + j1.88 \times 10^{-2}$	$(1.3493 - j0.0308)k_0$	$-3.49 \times 10^{-3} - j4.04 \times 10^-3$
		$(1.1910 - j0.1101)k_0$	$-7.20 \times 10^{-3} - j5.11 \times 10^{-3}$
		$(1.1435 - j0.0507)k_0$	$5.37 \times 10^{-2} + j2.16 \times 10^{-2}$

Table 4.2: Pole-residue pairs obtained by VECT-FIT for the geometry shown in 4.53 at $f = 30GHz$.

The surface-wave like behavior is the result of the leaky wave nature of the structure [6]. Since the frequency is high, (in other words, the thickness of the slab is high compared to the wavelength) the contribution of the branch point of region-1 is suppressed by the leaky waves, therefore, capturing only the branch point contribution of region-3 is sufficient to approximate the spatial domain Green's functions for this case.

4.3.12 3-level DCIM error: A slab between two different semi-infinite dielectrics, at low frequency

The geometry seen in Fig.4.53 is studied at $f = 1GHz$. The locations of the observation and the source (HED) points are at the interface between the air and the upper boundary of the dielectric layer ($z = h = 0$). For this structure, since one of the surrounding media has a dielectric constant greater than the slab, there are no surface waves. The results of numerical integration, and the 3-level DCIM are plotted below in Figs.4.56 and 4.57 below. For this example, VECT-FIT could not find any poles between k_0 and $k_{max} = 2k_0$ values for both the G^A_{xx} and G^q_x cases. In the 3-level DCIM, the following parameters are used: $T_{01} = 100$, $T_{02} = 200$ and $T_{03} = 99$, number of samples are 50, 100 and 100 for C_{ap1}, C_{ap2} and C_{ap3} respectively. The number of exponentials used are $N_1 = 3$, $N_2 = 3$ and $N_3 = 4$ for vector potential and $N_1 = 3$, $N_2 = 3$ and $N_3 = 4$ for scalar potential Green's functions.

As can be seen, the results obtained by the 3-level DCIM has errors, since it is not capable of capturing the second branch point. The only contribution captured is the branch point of region-1. Therefore, since there are no leaky wave contributions for this example and therefore both of the branch point contributions needed to be captured, the 3-level DCIM does not work for these kind of structures.

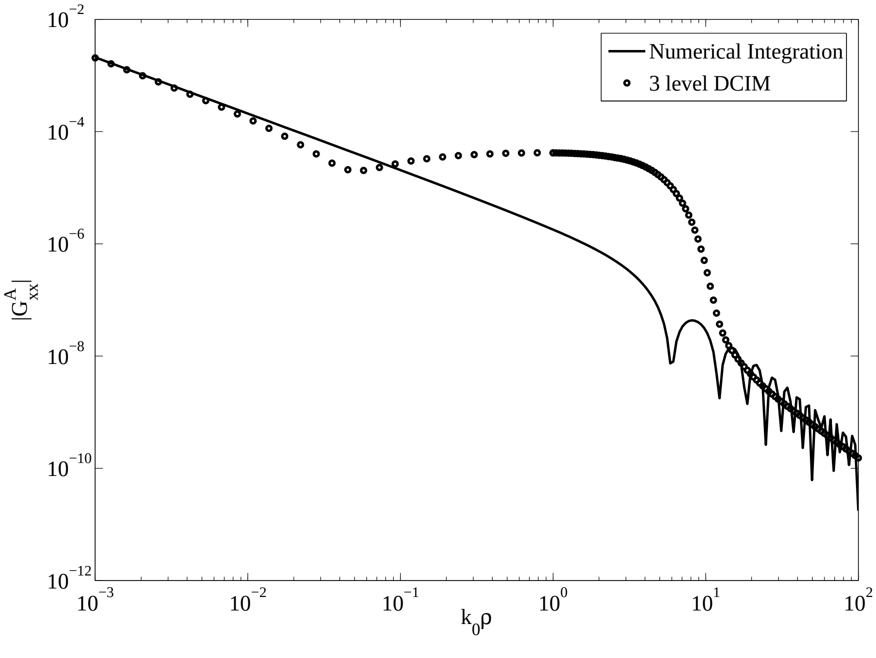

Figure 4.56: Magnitude of vector potential of the geometry in Fig.4.53 at $f = 1GHz$.

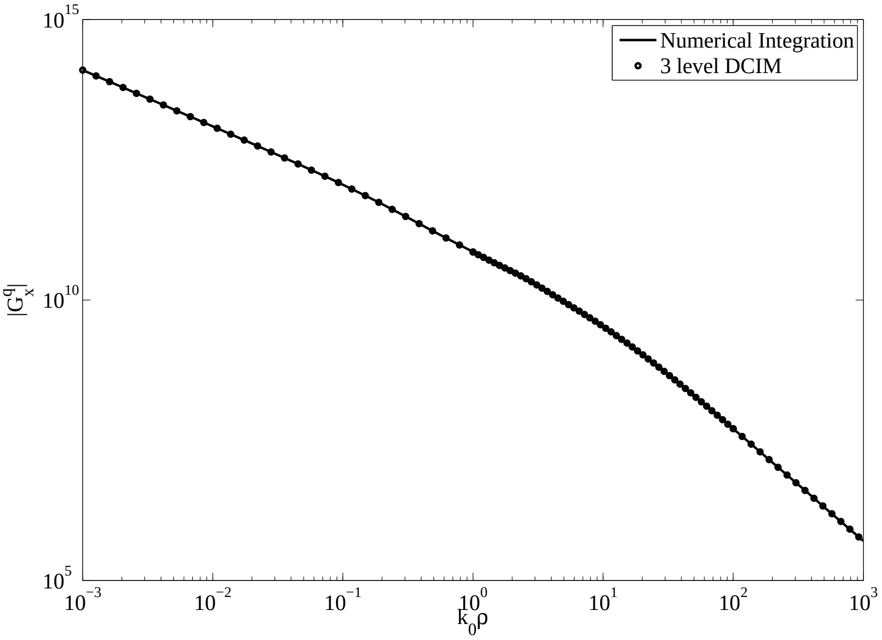

Figure 4.57: Magnitude of scalar potential of the geometry in Fig.4.53 at $f = 1GHz$.

Chapter 5

CONCLUSIONS AND FUTURE WORK

In this thesis, field and potential Green's functions of layered media were obtained for layered structures that contain RHMs, LHMs and metals by numerical integration and a modified approximation technique: 3-level DCIM. It was seen that the 3-level DCIM can solve the problematic cases of the original 2-level DCIM, as well as geometries those include LHMs. The results obtained by the 3-level DCIM were verified with the results obtained by numerical integration.

The study started with the general derivation of Green's functions for unbounded general and layered media. Then, to be able to solve the geometries that contain LHMs, the physical and analytical concepts of LHMs were investigated with a special emphasis on the singularities that cannot be seen in ordinary layered media, i.e. layered media containing only RHMs. At that stage, two new concepts: critical and threshold thicknesses, were presented to obtain a guideline for the possible locations of the singularities of such layered structures.

In the second part of the thesis, the original 2-level DCIM was analyzed in detail, and the problems of the method were discussed. The mostly pronounced problem of the original DCIM, i.e. lack of capturing the branch point contribution, was solved by the modified 3-level DCIM. It was shown both analytically and numerically that the contribution of the branch point can be captured by the 3-level DCIM, and as the result, the spectral domain Green's functions of the structures containing lossy slabs and structures with no surface wave poles can be approximated with great accuracy, both in near and far-field regions, which cannot be done by using the original 2-level approximation. Since the locations of the singularities may vary in layered media that contain LHMs, several 3-level DCIM versions were introduced to handle all kinds materials with arbitrary constitutive parameters and thicknesses. Several numerical examples of spatial domain Green's functions were presented, and it was shown that the results obtained by numerical integration and the 3-level DCIM are in very good agreement.

Even though the 3-level DCIM gives very good results in a variety of different cases, it cannot approximate the Green's functions of layered media with two different branch points, when the thicknesses of the slabs are small compared to wavelength. This problem can be solved by using both of the branch points in the approximation. To be able to achieve this, the paths of approximation need to be redefined carefully to capture the contributions of the branch points, by using the correct value of wave numbers, which is the future work for this study.

Appendix A

GENERALIZED PENCIL OF FUNCTION ALGORITHM

The generalized pencil of function algorithm (GPOF) is used in Chapter 2 and 4. In Chapter 2, it is used to determine the direct term of the series which is used to accelerate the convergence of Sommerfeld integration tails. In Chapter 4, it is used to approximate the spectral domain Green's functions by a set complex exponentials. Since the method plays an important role in the applications, it is given as an appendix here.

Consider an EM transient signal which can be approximated as follows:

$$y_k = \sum_{i=1}^{M} b_i \cdot e^{s_i \delta t k} \qquad k = 0, 1, 2, ...N-1 \tag{A.1}$$

where b_i are the complex residues, s_i are the complex poles and σt is the sampling interval. In order to find the poles, one can use the following algorithm [41, 83]:

1. Construct the following matrices:

$$\begin{aligned} Y_1 &= [\mathbf{y_0}, \mathbf{y_1}, ..., \mathbf{y_{L-1}}] && \text{(A.2)} \\ Y_2 &= [\mathbf{y_1}, \mathbf{y_2}, ..., \mathbf{y_L}] && \text{(A.3)} \\ & && \text{(A.4)} \end{aligned}$$

   where

$$\mathbf{y_i} = [y_i, y_{i+1}, ..., y_{i+N-L-1}]^T \tag{A.5}$$

   and L is the pencil parameter and its choice is around $L = N/2$.

2. Find the Z matrix as follows:

$$VD^{-1}U^H = SVD(Y_1) \tag{A.6}$$

$$V \leftarrow [V]_{M\times M}$$

$$U \leftarrow [U]_{M\times M}$$

$$D \leftarrow [D]_{M\times M}$$

$$Z = D^{-1}U^H Y_2 V \tag{A.7}$$

where SVD and H are the singular value decomposition and the complex conjugate transpose of a matrix respectively. The number of exponentials to be used to approximate the data, M, is decided according to the singular values of matrix Y_1.

3. The poles of the system are obtained as:

$$s_i = \frac{\log z_i}{\delta t} \qquad i = 1, 2, 3, ..., M \tag{A.8}$$

where z_i's are the eigenvalues of the Z matrix evaluated in step 2.

4. The residues are found from the least-squares solution of the following system:

$$\begin{bmatrix} 1 & 1 & ... & 1 \\ z_1 & z_2 & ... & z_M \\ \vdots & \vdots & \vdots & \vdots \\ z_1^{N-1} & z_2^{N-1} & ... & z_M^{N-1} \end{bmatrix} \begin{bmatrix} b_1 \\ b_2 \\ \vdots \\ b_M \end{bmatrix} = \begin{bmatrix} y_1 \\ y_2 \\ \vdots \\ y_M \end{bmatrix} \tag{A.9}$$

For the sake of completeness, the following MATLAB function, which implements the GPOF algorithm, is also given here.

```
% This Matlab script file approximates a given
% function with complex exponentials by using
% the Generalized Pencil of Function (GPOF)
% in the following form:
% f(t)=B(1)*exp(e(1)*Dt*t) + B(2)*exp(e(2)*Dt*t) + ... + B(M)*exp(e(M)*Dt*t)
% Input arguments:
% f: Samples pf the function which is going
%    to be approximated
% tol: tolerance value for the number of exponentials. Singular values
% with greater normalized magnitude are included.
% Output arguments
% e: Array containing the complex poles
% B: Array containing the complex residues
% M: Number of exponentials
function[e,B,M]=gpof_mod2fig(f,tol)
N=length(f);
G=f(1:N);
L=floor(N/2);
start=cputime;
% Construct the information vectors
for i=1:L
Y1(:,i)=G(i:i+N-L-1);
end;
%
for i=1:L
Y2(:,i)=G(i+1:i+N-L);
end;
% Apply the singular value decomposition to Y1.
[U,D,V]=svd(Y1);
count=0;
for ii=1:length(D(1,:))
```

```
    if abs(D(ii,ii))/abs(D(1,1))>tol
        count=count+1;
    else
        break;
    end
end
M=count;
DD=D(1:M,1:M); %since D is already a diagonal matrix
UU=U(:,1:M);
VV=V(:,1:M);
% Find the complex poles
Z=inv(DD)*UU'*Y2*VV;
z=eig(Z);
e=log(z);
for i=1:N
for k=1:M
ZZ(i,k)=z(k)^(i-1);
end;
end;
% Find the complex residues.
if M==0
    B=0;
else
    B=ZZ\diag(diag(G));
end
%
% Find the total cpu time.
%
approxtime=cputime-start;
% Construct the approximated function fapprox
for k=1:N
```

```
fapprox(k,1)=0.0;
for i=1:M
fapprox(k,1)=fapprox(k)+B(i)*exp(e(i)*(k-1));
end;
end;
error=norm(diag(diag(G))-fapprox);
% Plot the original function and the approximated functions
figure;
plot(real(fapprox),'r+');
hold on
plot(real(G));
xlabel('Data points');
ylabel('magnitude of the functions');
legend('magnitude of approximated function','Real part of original function');
```

Appendix B

PLANE WAVE SOLVER TOOL FOR LAYERED MEDIA

In Chapter 3, a number of propagation pattern results in layered media are shown. A code that calculates the amplitude transfer function in each layer, given in (2.63), is used to obtain these results. The amplitude of the incident field, i.e. the amplitude of the up-going wave in the source region, A_i^+, is set to a complex quantity with the magnitude of 1. By adding phase to this quantity, a propagation pattern on a plane or a movie on a line is obtained. This code, written in MATLAB, is given below.

```
 function kk=field_plotter(theta,f,E,M,D,polarization,mag_check,...
...geom_check,movie_check,z,x,zres,xres,movframe)
% theta: incident angle (degrees)
% f: frequency of operation (Hz.)
% E: permittivity of each layer, starting with the incident layer (unitless)
% M: permeability of each layer, starting with the incident layer (unitless)
% D: thickness of each layer (m.)
% polarization: 1: TE, 2: TM
% mag_check: 1: real part, 2: imaginary part, 3: absolute value of the solution
% geom_check: 1: only line, 2: only surface
% movie_check: 0: no movie, 1: only line movie
% z: thickness of the first and last layers (m.) (must be positive)
% x: thickness in x direction (m.) (must be positive)
% zres: resolution in z direction
% xres: resolution in x direction
% movframe: total movie frames
%%% Aytac Alparslan 7 Apr. 2008
%%%% allocation of the layers
h=0;
```

```
midlayerthick=sum(D);
zstart=-(midlayerthick+z(2));
if length(z)==2
    zend=z(1);
elseif length(z)==1
    zend=z;
else
    error('Please check the thickness values of the first and last layers');
end
zgeom=linspace(zstart,zend,zres);
xgeom=linspace(0,abs(x),xres);
%%% physical parameters
if polarization==2 %% interchange the values to handle TM polarization
    Ex=M; M=E; E=Ex; clear Ex;
end
c0=3e8;
kk=sqrt(E(1)*M(1))*2*pi*f/c0;
if real(E(1))<0 && real(M(1))<0
    lhstart=-1;
elseif real(E(1))>0 && real(M(1))>0
    lhstart=1;
else
    error('No field can propagate in the first layer');
end
teta=theta*pi/180;
kkx=sin(teta)*kk;
xph=abs(x)*kkx;
N=length(E);
%%% the solution generator
if geom_check==1 && movie_check==0
    phase=0;
```

```
elseif geom_check==1 && movie_check==1
    phase=-lhstart.*linspace(0,2*pi,movframe);
elseif geom_check==2
    phase=lhstart.*linspace(0,xph,xres);
else
    error('Please choose the geometry to show the solution...');
end
fprintf('Generating solution file...\n');
tic
for kkk=1:length(phase)
for ii=1:length(zgeom)
kk(kkk,length(zgeom)-ii+1)=fieldfun2(theta,N,f,E,M,D,zgeom(ii),h,phase(kkk));
end
end
toc
if mag_check==1
    kk_plot=real(kk); pl_term='Real part ';
elseif mag_check==2
    kk_plot=imag(kk); pl_term='Imaginary part ';
elseif mag_check==3
    kk_plot=abs(kk); pl_term='Magnitude ';
else
    error('Please choose what kind of result is needed...');
end
%%%the plotter
maxval=max(max(kk_plot)); minval=min(min(kk_plot));
zgeom=zgeom-z(1)+z(2);
if geom_check==1 && movie_check==0
    plot(zgeom,kk_plot);
    axis([min(zgeom) max(zgeom) minval maxval]);
    title([pl_term 'of the solution']);
```

```
    xlabel('Z (m.)');
    line([h h],[minval maxval],'LineStyle','--','LineWidth',2);
    hh=0;
    for kl=length(D):-1:1
        hh=hh-D(kl);
        line([hh hh],[minval maxval],'LineStyle','--','LineWidth',2);
    end
elseif geom_check==1 && movie_check==1
    while 1
    for ii=1:length(phase)
    plot(zgeom,kk_plot(ii,:));
    axis([min(zgeom) max(zgeom) minval maxval]);
    title([pl_term 'of the solution']);
    xlabel('Z (m.)');
    line([h h],[minval maxval],'LineStyle','--','LineWidth',2);
    hh=0;
    for kl=length(D):-1:1
        hh=hh-D(kl);
        line([hh hh],[minval maxval],'LineStyle','--','LineWidth',2);
    end
    pause(0.1);
    end
    end
elseif geom_check==2
    [Z,X]=meshgrid(zgeom,xgeom);
    hold on;
    %surfc(X,Z,kk_plot,'LineStyle','none'); %surface
    contourf(X,Z,kk_plot,linspace(minval,maxval,50),'LineStyle','none'); %contour
    axis equal;
    axis ([min(xgeom) max(xgeom) min(zgeom) max(zgeom)]);
    xlabel('X (m.)'); ylabel('Z (m.)');
```

```
    title([pl_term 'of the solution']);
    colorbar;
    line([0 x],[h h],'LineStyle','--','LineWidth',2);
    hh=0;
    for kl=length(D):-1:1
        hh=hh-D(kl);
        line([0 x],[hh hh],'LineStyle','--','LineWidth',2);
    end
end
return;
%%%the solver
function fieldE=fieldfun2(theta,N,f,E,M,D,Z,h,phase)
% generated by E. Pinar Karabulut
teta=theta*pi/180; %angle of incidence in radian
c=3e8; %speed of light
DD=[D 0];
freq=f;
w=2*pi*freq; %angular frequency
% propogation constants of the layers
n=sqrt(E.*M); % refractive index of each layer
for klm=1:length(E)
    if real(E(klm))<0 & real(M(klm))<0 %is the layer lhm?
        n(klm)=-n(klm); signer(klm)=1;
    else
        signer(klm)=0;
    end
end
k=n.*w/c;%propagation constant of each layer
ki=k(1,1); kix=ki*sin(teta);
kz=sqrt(((w*n./c).^2)-kix^2);
for klm=1:length(kz)
```

```
    if imag(kz(klm))>0
        kz(klm)=-kz(klm);
    end
end
for klm=1:length(kz)
    if signer(klm)==1 & real(kz(klm))>0
        kz(klm)=-kz(klm); %if lhm, change the wave vector
    end
end
% fresnel reflections
tt=1;
for t=2:N
    R(tt)=(M(t)*kz(t-1)-M(t-1)*kz(t))/(M(t)*kz(t-1)+M(t-1)*kz(t));%TE
    tt=tt+1;
end
T=R+1;
Rinv=-R;
Tinv=Rinv+1;
% GRC
GRC=zeros(1,N);
%%% eps=-0.99 mu=-0.99 means pec
if E(N)==-0.99 & M(N)==-0.99
    GRC(N-1)=-1;
else
    GRC(N-1)=R(N-1);
end
GRC(N)=0;
A=zeros(1,N);
A(1)=1*exp(-j*phase); %up-going wave's amplitude in source layer.
dist11=h+cumsum([0 D]);
dist1=dist11;
```

```
zz=Z;
for t=N-2:-1:1
    GRC(t)=R(t)+(T(t)*Tinv(t)*GRC(t+1)*exp(-j*kz(t+1)*2*DD(t))/...
...(1+GRC(t+1)*R(t)*exp(-j*kz(t+1)*2*DD(t))));
end
% Amplitude Transfer function and corresponding fields
dd=-dist1;
for t=1:N-1
    A(t+1)=(A(t)*(T(t)*exp(-j*kz(t)*dist1(t))/(1+GRC(t+1)*R(t)...
...*exp(-j*kz(t+1)*2*DD(t)))))*exp(j*kz(t+1)*dist1(t));
        if zz>=dd(t)
        fieldE=A(t)*(exp(j*kz(t)*zz)+GRC(t)*exp(-j*kz(t)*zz)...
...*exp(-j*kz(t)*2*dist1(t)));
        break
        else
        fieldE=A(N)*exp(j*kz(N)*zz);
        end
end
return;
```

As an example, to obtain the pattern in Fig.3.3.b, the following input must be given:

```
 kk=field_plotter(45,1e9,[1 -2-0.2j 1],[1 -1.5-0.2j 1],...
...[0.6],1,1,2,0,[0.6 0.6],1,70,70,0);
```

To see the movie of the propagation of waves on a lie for the same geometry, the following input must be given:

```
 kk=field_plotter(45,1e9,[1 -2-0.2j 1],[1 -1.5-0.2j 1],...
...[0.6],1,1,1,1,[0.6 0.6],1,70,70,0);
```

The code with the graphical user interface can be obtained from `aytac@ieee.org`.

Appendix C

VECTOR FITTING ALGORITHM

C.1 The VECT-FIT Algorithm

The vector fitting algorithm was first proposed in power delivery and systems community [79]. It is then applied to EM problems to approximate the spectral domain Green's functions in terms of rational functions [28, 30].

The method is capable of fitting rational functions to the frequency response of systems of the form:

$$f(s) \approx \sum_{n=1}^{N} \frac{c_n}{s-a_n} + d + sh \tag{C.1}$$

In (C.1), note that the constants d and/or h can be zero depending on whether the system is strictly proper, proper or improper. If the system is strictly proper, i.e. $order(numerator) = order(denominator) - 1$, both of the coefficients would be zero. If the system is proper, i.e. $order(numerator) = order(denominator)$, only h would be zero and if the system is improper, i.e. $order(numerator) = order(denominator) + 1$, both of the coefficients would be non-zero. In the derivation below, the system is assumed to be improper as it is the most general case. The vect-fit algorithm solves the problem of approximation of frequency responses of linear systems in 2 stages as follows [79]: *1. Pole identification* Consider the rational approximation given in (C.1). Consider a set of starting poles $\bar{a}_n$ and multiply $f(s)$ by an unknown function $\sigma(s)$ which gives the following augmented problem:

$$\begin{bmatrix} \sigma(s)f(s) \\ \sigma(s) \end{bmatrix} = \begin{bmatrix} \sum_{n=1}^{N} \frac{c_n}{s-\bar{a}_n} + d + sh \\ \sum_{n=1}^{N} \frac{\tilde{c}_n}{s-\bar{a}_n} + 1 \end{bmatrix} \tag{C.2}$$

In (C.2), note that the poles of the rational approximation og $\sigma(s)$ and $f(s)\sigma(s)$ has the same pole locations. Multiplying the second row of (C.2) gives the following relation:

$$\begin{aligned} (\sigma(s)f(s))_{fit} &\approx \sigma_{fit} f(s) \\ \sum_{n=1}^{N} \frac{c_n}{s-\bar{a}_n} + d + sh &\approx \left(\sum_{n=1}^{N} \frac{\tilde{c}_n}{s-\bar{a}_n} + 1 \right) f(s) \end{aligned} \tag{C.3}$$

At a given frequency point, s_k, (C.3) can be written as a matrix equation as follows:

$$\mathbf{A_k x} = b_k \tag{C.4}$$

where

$$\begin{aligned}\mathbf{A_k} &= \left[\frac{1}{s_k - a_1} \;\; ... \;\; \frac{1}{s_k - a_N} \quad 1 \quad s_k \quad \frac{-f(s_k)}{s_k - a_1} \;\; ... \;\; \frac{-f(s_k)}{s_k - a_N}\right] \\ \mathbf{x} &= \left[c_1 \;\; ... \;\; c_N \;\; d \;\; h \;\; \tilde{c}_1 \;\; ... \;\; \tilde{c}_N\right]^T, \;\; b_k = f(s_k)\end{aligned} \tag{C.5}$$

In (C.5), $\mathbf{A_k}$ and $\mathbf{x}$ are row and column vectors respectively. By writing (C.4) at a set of frequency points, $s_1 ... s_M$, a linear matrix equation is formed as:

$$\mathbf{Ax} = \mathbf{b} \tag{C.6}$$

where the unknowns $c_n, \bar{c}_n, h$ and d are the elements of $\mathbf{x}$.

When the two sum of partial fractions in (C.3) are written as a fraction, the following relation is obtained:

$$(\sigma f)_{fit}(s) = h\frac{\Pi_{n=1}^{N+1}(s - z_n)}{\Pi_{n=1}^{N}(s - \bar{a}_n)}, \sigma_{fit}(s) = \frac{\Pi_{n=1}^{N}(s - \bar{z}_n)}{\Pi_{n=1}^{N}(s - \bar{a}_n)} \tag{C.7}$$

from (C.7), $f(s)$ can be written as:

$$f(s) = h\frac{\Pi_{n=1}^{N+1}(s - z_n)}{\Pi_{n=1}^{N}(s - \bar{z}_n)} \tag{C.8}$$

As seen in (C.7) and (C.8), the zeros of $\sigma(s)$ becomes the poles of f(s). Therefore by calculating the zeros of $\sigma_{fit}(s)$, one can get a set of poles for fitting the original function $f(s)$. To determine the zeros of $\sigma_{fit}(s)$ consider the following linear system:

$$Y(s) = \sigma_{fit}(s)U(s) \tag{C.9}$$

where $\sigma_{fit}(s)$ is written in the form of sum of partial fractions in the second row of (C.2). The state-space realization of this system is:

$$\begin{aligned}\dot{x} &= A'x + B'u \\ y &= C'x + D'u\end{aligned} \tag{C.10}$$

where

$$\begin{aligned}A' &= diag(\bar{a}_1 ... \bar{a}_N) \\ B' &= [1 ... 1]^T \\ C' &= [\tilde{c}_1 ... \tilde{c}_N] \\ D' &= 1\end{aligned} \tag{C.11}$$

Interchanging the input and output gives the state space realization of inverse of $\sigma_{fit}(s)$ as follows:,

$$\begin{aligned} \dot{x} &= \left(A' - B'D'^{-1}C'\right) + B'D'^{-1}u \\ u &= -D'^{-1}C'x + D'^{-1}y \end{aligned} \tag{C.12}$$

From (C.12), the inverse of $\sigma_{fit}(s)$, i.e. $1/\sigma_{fit}(s)$, is given by:

$$U = \left(-D'^{-1}C'(sI - (A' - B'D'^{-1}C'))^{-1}B'D'^{-1} + D'^{-1})\right) Y \tag{C.13}$$

The zeros of the function $\sigma_{fit}(s)$, are given by the eigenvalues of the matrix $A' - B'C'$, where the elements A', B' and C' are given in (C.11). The reason for this fact is clear in (C.13): The denominator of $1/\sigma_{fit}(s)$, i.e. the zeros of $\sigma_{fit}(s)$, comes from $(sI - (A' - B'D'^{-1}C'))^{-1}$, which is equal to eigenvalues of $sI - (A' - B'C')$ (since $D' = D'^{-1} = 1$). *2. Residue Identification* Step 1 of vect-fit algorithm is done in an iterative fashion, until a convergence is reached. After a convergence is obtained, the residues of the fractions are found as the solution of the following equation:

$$\mathbf{Ax} = \mathbf{b} \tag{C.14}$$

where kth row of the matrix $\mathbf{A}$, the vector $\mathbf{x}$ and the kth element of vector $\mathbf{b}$ are given as:

$$\begin{gathered} \mathbf{A_k} = \begin{bmatrix} \frac{1}{s_k - a_1} & \dots & \frac{1}{s_k - a_N} & 1 & s_k \end{bmatrix} \\ \mathbf{x} = \begin{bmatrix} c_1 & \dots & c_N & d & h \end{bmatrix}^T, \quad b_k = f(s_k) \end{gathered} \tag{C.15}$$

Together with the poles obtained in Step 1, the solution of (C.15) gives a rational function fitting shown in (C.1).

C.2 Modifying the VECT-FIT Algorithm for extracting poles of Green's functions

In the discussion above, the poles are extracted in the form given in (C.1). In the case of extracting poles of Green's functions, which corresponds to the poles of surface waves which are cylindrical waves, the following integral identity is used to obtain the spatial domain Green's functions from spectral domain Green's functions:

$$\int_{-\infty}^{\infty} \frac{1}{k_\rho^2 - k_{\rho p}^2} H_0^{(2)}(k_\rho \rho) k_\rho dk_\rho = -j\pi H_0^{(2)}(k_{\rho p}\rho) \tag{C.16}$$

where $k_{\rho p}$ is the pole of Green's function in spectral domain. As seen in (C.16), the poles of the Green's function must be extracted in the form:

$$g(k_\rho) \approx \sum_{n=1}^{N} \frac{c_n}{k_\rho^2 - k_{\rho p,n}^2} \tag{C.17}$$

To use the vector fitting algorithm for this purpose, following changes are applied to the original vector fitting algorithm:

1. The system is assumed to be strictly proper in quadratic sense, i.e. $order(numerator) = order(denominator) - 2$. This step is crucial, since both of the coefficients h and d given in (C.1) must be zero to apply the integral identity to the result of the fitting. The changes made in the original vector fitting algorithm are:

$$\begin{aligned} A_k &= \begin{bmatrix} \frac{1}{s_k^2-a_1^2} & \dots & \frac{1}{s_k^2-a_N^2} & \frac{-f(s_k)}{s_k^2-a_1^2} & \dots & \frac{-f(s_k)}{s_k^2-a_N^2} \end{bmatrix} \\ x &= \begin{bmatrix} c_1 & \dots & c_N & \tilde{c}_1 & \dots & \tilde{c}_N \end{bmatrix}^T \end{aligned} \tag{C.18}$$

2. The imaginary parts of the poles must be negative to ensure that the fields defined by the RHS of (C.16) obey causality and radiation conditions, i.e. they must vanish at infinity. In the original vect-fit algorithm, the poles and corresponding residues come in complex conjugate pairs. In the case of extracting the poles of Green's functions, the pole locations are enforced have negative imaginary parts with the corresponding residues as discussed in [28].

By using the changes given above, the surface wave poles of the Green's functions can be found by the VECT-FIT algorithm. For this purpose, a set of rational functions of the form shown in (C.17) is fitted to the spectral-domain Green's functions on the line shown in Fig.C.1. After the fitting, a set of rational functions are obtained as follows:

$$\frac{\tilde{G}}{j2k_{zi}} = \sum_{n=1}^{N_1} \frac{c_{1,n}}{k_\rho^2 - k_{\rho p1,n}^2} + \sum_{n=1}^{N_2} \frac{c_{2,n}}{k_\rho^2 - k_{\rho p2,n}^2} \text{where } \mathrm{Re}(k_{\rho p1,n}) \in [k_0, k_{max}] \tag{C.19}$$

As seen in (C.19), the set of poles $k_{\rho p1,n}$ have a real part between k_0 and k_{max}. Since the real parts of surface wave poles of a layered structure lies in this region, the set $k_{\rho p1,n}$ with $c_{1,n}$ makes a pole-residue pair which are used to extract the surface wave singularities from the spectral domain Green's functions as follows:

$$\tilde{F}(k_\rho) = \tilde{G} - \sum_{n=1}^{N_1} \frac{c_{1,n}}{k_\rho^2 - k_{\rho p1,n}^2} 2jk_{zi}e^{jk_{zi}|z|} \tag{C.20}$$

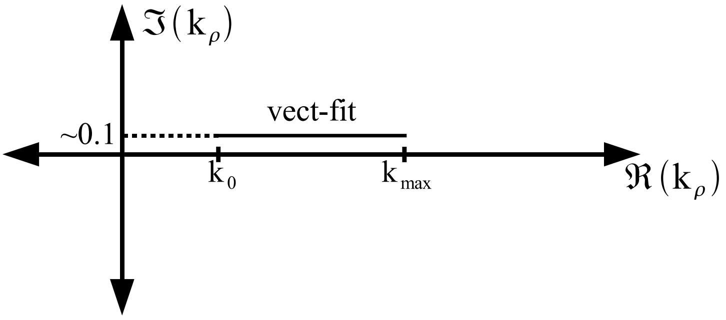

Figure C.1: The path on which the vect-fit algorithm is used to extract poles of the spectral-domain Green's functions.

By applying DCIM to the remaining spectral-domain Green's functions, $\tilde{F}(k_\rho)$ in (C.20), an improved DCIM is obtained which can approximate spatial-domain Green's functions by a set of point (exponentials obtained by DCIM) and line (rational functions obtained by vect-fit) sources as:

$$G(\rho) = \sum_{i=1}^{M} a_{1,i} \frac{e^{-jk_i r_{1,i}}}{4\pi\varepsilon_i r_{1,i}} - \frac{j}{4\varepsilon_i} \sum_{n=1}^{N_1} c_{1,n} H_0^{(2)}(k_{\rho p1,n}\rho) \tag{C.21}$$

It must be noted that the derivation above is done under the assumption that all the regions of the layered medium are RHMs. By changing the bounds of the possible SWP locations, the SWPs and SPPs can also be captured by using the VECT-FIT algorithm. For sake of completeness a MATLAB code of VECT-FIT is given here.

```
function [poles,residues,conver,checker]=vectfitem2(f,s,poles,...
...residues_old,count,checker,tol)
%inputs:
%f: data samples
%s: sampling points
%residues_old: residues from the previous iteration
%count: current number of iteration (for statistical purpose)
%checker: error term from the previous iteration (for statistical purpose)
%tol: tolerance for stop
%outputs:
%poles: poles obtained
```

```
%residues: residues obtained
%conver: convergence variable
%checker: error term of the current iteration (for statistical purpose)
Np=size(f);
Npole=length(poles);
A=[]; b=[];
[k,l]=size(poles);
if k==1
    poles=poles;
elseif l==1
    poles=poles';
else
    error('Please check the initial pole locations');
end
if Np(1)<Np(2)
    f=f';
    s=s';
elseif Np(1)>Np(2)
    f=f;
    s=s;
else
    error('Please check f vector');
end
Np=size(f);
for kk=1:Np(1)
    Adum=[];
for M=1:Np(2)
    K1=1./(s(kk,M)^2-poles); K2=-K1.*f(kk,M);
    K=[K1 K2]; Adum=[Adum;K];
end
A=[A;Adum]; b=[b f(kk,:)];
```

```
end
b=b.';
for col=1:length(A(1,:));
  Escale(col)=norm(A(:,col),2);
  A(:,col)=A(:,col)./Escale(col);
end
x=A\b; x=x./Escale.';
for N=1:length(poles)
    Ahat(N,N)=poles(N).^2;
end
C=[]; C(1:Npole,1)=x(1:Npole,1);
C(1:Npole,2)=x(Npole+1:2*Npole,1);
C=C.';
for N=1:length(poles)
    Ahat(N,N)=poles(N);
end
newpoleident=norm(poles);
Hhat=Ahat-ones(length(C(2,:)),1)*C(2,:);
oldresident=abs(sum(residues_old));
poles=eig(Hhat);
poles=poles.';
%%%determination of residues
clear A K1 K2 K;
    A=[];
    for kk=1:Np(1)
        Adum=[];
        for M=1:Np(2)
            K1=1./(s(kk,M).^2-poles);
            Adum=[Adum;K1];
        end
        A=[A;Adum];
```

```
end
residues=A\b;
newresident=abs(sum(residues));
checker(count)=abs(newresident-oldresident)/max(abs(residues));
if checker(count)>tol
    conver=0;
else
    conver=1;
end
```

The original version of the vect-fit algorithm can be downloaded from the webpage of the author of [79]: `http://www.energy.sintef.no/Produkt/VECTFIT/MENU.htm`

VITA

Aytaç Alparslan was born in İstabul, Turkey on January 23, 1983. He received the B.S. degree in Electrical and Electronics Engineering from Koç University, İstanbul, Turkey in 2006. Starting from September 2006, he was a research and teaching assistant at Koç University, Electrical and Computer Engineering Department. He received the Undergraduate Scholarships from IEEE MTT and AP societies in 2005. His research interests include computational electromagnetics, metamaterials and photonic band-gap structures and nanophotonics.

BIBLIOGRAPHY

[1] R. E. Colin, "Hertzian dipole radiating over a lossy earth or sea: Some early and late 20th-century controversies," *Antennas and Propagation Magazine, IEEE*, vol. 46, no. 2, pp. 64–79, Apr. 2004.

[2] R. F. Harrington, *Field Computation by Moment Methods*, Florida: Robert E. Krieger Publishing Company, 1982.

[3] J. R. Mosig and F. E. Gardiol, "General integral equation formulation for microstrip antennas and scatterers," *Proceedings, IEEE*, vol. 132, no. 7, pp. 424–432, Dec 1985.

[4] J. R. Mosig, "Arbitrarily shaped microstrip structures and their analysis with a mixed potential integral equation," *Microwave Theory and Techniques, IEEE Transactions on*, vol. 36, no. 2, pp. 314–323, Feb 1988.

[5] K.A. Michalski and D. Zheng, "Electromagnetic scattering and radiation by surfaces of arbitrary shape in layered media. i. theory," *Antennas and Propagation, IEEE Transactions on*, vol. 38, no. 3, pp. 335–344, Mar 1990.

[6] W. C. Chew, *Waves and Fields in Inhomogeneous Media*, New York: Van Nostrand Reinhold, 1990.

[7] L. Alatan, M.I. Aksun, K. Mahadevan, and T. Birand, "Analytical evaluation of the mom matrix elements," *Microwave Theory and Techniques, IEEE Transactions on*, vol. 44, no. 4, pp. 519–525, Apr 1996.

[8] N. Kinayman and M. I. Aksun, "Efficient use of closed-form green's functions for the analysis of planar geometries with vertical connections," *Microwave Theory and Techniques, IEEE Transactions on*, vol. 45, no. 5, pp. 593–603, May 1997.

[9] M.J. Tsai, F.D. Flavis, O. Fordharn, and N.G. Alexopoulos, "Modeling planar arbitrarily shaped microstrip elements in multilayered media," *Microwave Theory and Techniques, IEEE Transactions on*, vol. 45, no. 3, pp. 330–337, Mar 1997.

[10] M. R. Abdul-Gaffoor, H. K. Smith, A. A. Kishk, and A. W. Glisson, "Simple and efficient full-wave modeling of electromagnetic coupling in realistic rf multilayer pcb layouts," *Microwave Theory and Techniques, IEEE Transactions on*, vol. 50, no. 6, pp. 1445–1457, Jun 2002.

[11] T. Onal, M. I. Aksun, and N. Kinayman, "An efficient full-wave simulation algorithm for multiple vertical conductors in printed circuits," *Microwave Theory and Techniques, IEEE Transactions on*, vol. 54, no. 10, pp. 3739–3745, Oct 2006.

[12] T. Onal, M. I. Aksun, and N. Kinayman, "A rigorous and efficient analysis of 3-d printed circuits: vertical conductors arbitrarily distributed in multilayer environment," *Antennas and Propagaton, IEEE Transactions on*, vol. 55, no. 12, pp. 3726–3729, Dec 2007.

[13] N. Kinayman and M. I. Aksun, *Modern Microwave Circuits*, Artech House, 2005.

[14] J. R. Mosig and F. E. Gardiol, "A dynamical radiation model for microstrip structures," in *Advances in Electronics and Electron Physics*, P. W. Hawkes, Ed. 1982, vol. 59, pp. 139–237, New York: Academic.

[15] N. Kinayman and M. I. Aksun, "Comparative study of acceleration techniques for integrals and series in electromagnetic problems," *Radio Science*, vol. 30, pp. 1713–1722, Nov.-Dec. 1995.

[16] K.A. Michalski, "Extrapolation methods for sommerfeld integral tails," *Antennas and Propagation, IEEE Transactions on*, vol. 46, no. 10, pp. 1405–1418, Oct 1998.

[17] D. C. Fang, J. J. Yang, and G. Y. Delisle, "Discrete image theory for horizontal electric dipoles in a multilayered medium," *Proceedings, IEEE*, vol. 135, no. 5, pp. 297–303, Oct 1988.

[18] Y.L. Chow, J.J. Yang, D.G. Fang, and G.E. Howard, "A closed-form spatial green's function for the thick microstrip substrate," *Microwave Theory and Techniques, IEEE Transactions on*, vol. 39, no. 3, pp. 588–592, Mar 1991.

[19] M.I. Aksun and R. Mittra, "Derivation of closed-form green's functions for a general microstrip geometry," *Microwave Theory and Techniques, IEEE Transactions on*, vol. 40, no. 11, pp. 2055–2062, Nov 1992.

[20] G. Dural and M.I. Aksun, "Closed-form green's functions for general sources and stratified media," *Microwave Theory and Techniques, IEEE Transactions on*, vol. 43, no. 7, pp. 1545–1552, Jul 1995.

[21] M.I. Aksun, "A robust approach for the derivation of closed-form green's functions," *Microwave Theory and Techniques, IEEE Transactions on*, vol. 44, no. 5, pp. 651–658, May 1996.

[22] C. Tokgoz and G. Dural, "Closed-form green's functions for cylindrically stratified media," *Microwave Theory and Techniques, IEEE Transactions on*, vol. 48, no. 1, pp. 40–49, Jan 2000.

[23] Yuehe Ge and K.P. Esselle, "New closed-form green's functions for microstrip structures theory and results," *Microwave Theory and Techniques, IEEE Transactions on*, vol. 50, no. 6, pp. 1556–1560, Jun 2002.

[24] N.V. Shuley, R.R. Boix, F. Medina, and M. Horno, "On the fast approximation of green's functions in mpie formulations for planar layered media," *Microwave Theory and Techniques, IEEE Transactions on*, vol. 50, no. 9, pp. 2185–2192, Sep 2002.

[25] V.I. Okhmatovski and A.C. Cangellaris, "Evaluation of layered media green's functions via rational function fitting," *Microwave and Wireless Components Letters, IEEE*, vol. 14, no. 1, pp. 22–24, Jan. 2004.

[26] M.I. Aksun and G. Dural, "Clarification of issues on the closed-form green's functions

in stratified media," *Antennas and Propagation, IEEE Transactions on*, vol. 53, no. 11, pp. 3644–3653, Nov. 2005.

[27] Mengtao Yuan, T.K. Sarkar, and M. Salazar-Palma, "A direct discrete complex image method from the closed-form green's functions in multilayered media," *Microwave Theory and Techniques, IEEE Transactions on*, vol. 54, no. 3, pp. 1025–1032, March 2006.

[28] V.N. Kourkoulos and A.C. Cangellaris, "Accurate approximation of green's functions in planar stratified media in terms of a finite sum of spherical and cylindrical waves," *Antennas and Propagation, IEEE Transactions on*, vol. 54, no. 5, pp. 1568–1576, May 2006.

[29] R. R. Boix, F. Mesa, and F. Medina, "Application of total least squares to the derivation of closed-form green's functions for planar layered media," *Microwave Theory and Techniques, IEEE Transactions on*, vol. 55, no. 2, pp. 268–280, Feb. 2007.

[30] A.G. Polimeridis, T.V. Yioultsis, and T.D. Tsiboukis, "A robust method for the computation of green's functions in stratified media," *Antennas and Propagation, IEEE Transactions on*, vol. 55, no. 7, pp. 1963–1969, July 2007.

[31] F. Mesa, R. R. Boix, and F. Medina, "Closed-form expressions of multilayered planar green's functions that account for the continuous spectrum in the far field," *Microwave Theory and Techniques, IEEE Transactions on*, vol. 56, no. 7, pp. 1601–1614, July 2008.

[32] K. Michalski, "On the scalar potential of a point charge associated with a time-harmonic dipole in a layered medium," *Antennas and Propagation, IEEE Transactions on*, vol. 35, no. 11, pp. 1299–1301, Nov 1987.

[33] Feng Ling and Jian-Ming Jin, "Discrete complex image method for green's functions of general multilayer media," *Microwave and Guided Wave Letters, IEEE*, vol. 10, no. 10, pp. 400–402, Oct 2000.

[34] A. G. Polimeridis, T. V. Yioultsis, and T. D. Tsiboukis, “An efficient pole extraction technique for the computation of green’s functions in stratified media using a sine transformation,” *Antennas and Propagation, IEEE Transactions on*, vol. 55, no. 1, pp. 227–229, Jan. 2007.

[35] Shung-Wu Lee, J. Boersma, Chak-Lam Law, and G. Deschamps, “Singularity in green’s function and its numerical evaluation,” *Antennas and Propagation, IEEE Transactions on*, vol. 28, no. 3, pp. 311–317, May 1980.

[36] S.-A. Teo, S.-T. Chew, and M.-S. Leong, “Error analysis of the discrete complex image method and pole extraction,” *Microwave Theory and Techniques, IEEE Transactions on*, vol. 51, no. 2, pp. 406–413, Feb. 2003.

[37] Mengtao Yuan and T.K. Sarkar, “Computation of the sommerfeld integral tails using the matrix pencil method,” *Antennas and Propagation, IEEE Transactions on*, vol. 54, no. 4, pp. 1358–1362, April 2006.

[38] J. H. Mathew and K. D. Fink, *Numerical Methods using MATLAB*, Prentice-Hall, 1999.

[39] Herbert H. H. Homeier, “Analytical and numerical studies of the convergence behavior,” *of the J transformation, J. Comput. Appl. Math*, vol. 69, pp. 81–112, 1996.

[40] Lucas S.K., “Evaluating infinite integrals involving products of bessel functions of arbitrary order,” *Journal of Computational and Applied Mathematics*, vol. 64, pp. 269–282(14), 20 December 1995.

[41] Y. Hua and T.K. Sarkar, “Generalized pencil-of-function method for extracting poles of an em system from its transient response,” *Antennas and Propagation, IEEE Transactions on*, vol. 37, no. 2, pp. 229–234, Feb 1989.

[42] V. G. Veselago, “The electrodynamics of substances with simultaneous negative values of,” *Sov. Phys.–Usp.*, vol. 47, pp. 509–514, Jan.–Feb. 1968.

[43] David R. Smith and Norman Kroll, "Negative refractive index in left-handed materials," *Phys. Rev. Lett.*, vol. 85, no. 14, pp. 2933–2936, Oct 2000.

[44] Richard W. Ziolkowski and Ehud Heyman, "Wave propagation in media having negative permittivity and permeability," *Phys. Rev. E*, vol. 64, no. 5, pp. 056625, Oct 2001.

[45] Victor Veselago, Leonid Braginsky, Valery Shklover, and Christian Hafner, "Negative refractive index materials," *Journal of Computational and Theoretical Nanoscience*, vol. 3, pp. 189–218(30), April 2006.

[46] J. B. Pendry, "Negative refraction makes a perfect lens," *Phys. Rev. Lett.*, vol. 85, no. 18, pp. 3966–3969, Oct 2000.

[47] D. R. Smith, Willie J. Padilla, D. C. Vier, S. C. Nemat-Nasser, and S. Schultz, "Composite medium with simultaneously negative permeability and permittivity," *Phys. Rev. Lett.*, vol. 84, no. 18, pp. 4184–4187, May 2000.

[48] R.W. Ziolkowski, "Design, fabrication, and testing of double negative metamaterials," *Antennas and Propagation, IEEE Transactions on*, vol. 51, no. 7, pp. 1516–1529, July 2003.

[49] J.B. Pendry, A.J. Holden, D.J. Robbins, and W.J. Stewart, "Magnetism from conductors and enhanced nonlinear phenomena," *Microwave Theory and Techniques, IEEE Transactions on*, vol. 47, no. 11, pp. 2075–2084, Nov 1999.

[50] J. B. Pendry, A. J. Holden, W. J. Stewart, and I. Youngs, "Extremely low frequency plasmons in metallic mesostructures," *Phys. Rev. Lett.*, vol. 76, no. 25, pp. 4773–4776, Jun 1996.

[51] Viktor A. Podolskiy and Evgenii E. Narimanov, "Near-sighted superlens," *Opt. Lett.*, vol. 30, no. 1, pp. 75–77, 2005.

[52] V. M. Shalaev, W. Cai, U. K. Chettiar, H.-K. Yuan, A. K. Sarychev, V. P. Drachev, and A. V. Kildishev, "Negative index of refraction in optical metamaterials," *Optics Letters*, vol. 30, pp. 3356–3358, Dec. 2005.

[53] Stefan Linden, Christian Enkrich, Gunnar Dolling, Matthias W. Klein, Jiangfeng Zhou, Thomas Koschny, Costas M. Soukoulis, Sven Burger, Frank Schmidt, and Martin Wegener, "Photonic metamaterials: Magnetism at optical frequencies," *Selected Topics in Quantum Electronics, IEEE Journal of*, vol. 12, no. 6, pp. 1097–1105, Nov.-dec. 2006.

[54] Z. Liu, S. Durant, H. Lee, Y. Pikus, N. Fang, Y. Xiong, C. Sun, and X. Zhang, "Far-field optical superlens," *Nano Letters*, vol. 7, no. 2, pp. 403–408, 2007.

[55] Costas M. Soukoulis, Stefan Linden, and Martin Wegener, "PHYSICS: Negative Refractive Index at Optical Wavelengths," *Science*, vol. 315, no. 5808, pp. 47–49, 2007.

[56] Xudong Chen, Bae-Ian Wu, Jin Au Kong, and Tomasz M. Grzegorczyk, "Retrieval of the effective constitutive parameters of bianisotropic metamaterials," *Physical Review E (Statistical, Nonlinear, and Soft Matter Physics)*, vol. 71, no. 4, pp. 046610, 2005.

[57] D. R. Smith, D. C. Vier, Th. Koschny, and C. M. Soukoulis, "Electromagnetic parameter retrieval from inhomogeneous metamaterials," *Physical Review E (Statistical, Nonlinear, and Soft Matter Physics)*, vol. 71, no. 3, pp. 036617, 2005.

[58] M.I. Aksun, A. Alparslan, E.P. Karabulut, E. Irci, and V.B. Erturk, "Determining the effective constitutive parameters of finite periodic structures: Photonic crystals and metamaterials," *Microwave Theory and Techniques, IEEE Transactions on*, vol. 56, no. 6, pp. 1423–1434, June 2008.

[59] Andrea Alù and Nader Engheta, "Plasmonic materials in transparency and cloaking problems: mechanism, robustness, and physical insights," *Opt. Express*, vol. 15, no. 6, pp. 3318–3332, 2007.

[60] D. R. Smith, J. B. Pendry, and M. C. K. Wiltshire, "Metamaterials and negative refractive index," *Science*, vol. 305, no. 5685, pp. 788–792, 2004.

[61] R. Merlin, "Analytical solution of the almost-perfect-lens problem," *Applied Physics Letters*, vol. 84, no. 8, pp. 1290–1292, 2004.

[62] David K. Cheng, *Field and Wave Electromagnetics*, Addison Wesley, 2 edition, 1989.

[63] Robert E. Collin, *Field Theory of Guided Waves*, Wiley Interscience, 2 edition, 1991.

[64] P. Baccarelli, P. Burghignoli, F. Frezza, A. Galli, P. Lampariello, G. Lovat, and S. Paulotto, "Fundamental modal properties of surface waves on metamaterial grounded slabs," *Microwave Theory and Techniques, IEEE Transactions on*, vol. 53, no. 4, pp. 1431–1442, April 2005.

[65] Bae-Ian Wu, Tomasz M. Grzegorczyk, Yan Zhang, and Jin Au Kong, "Guided modes with imaginary transverse wave number in a slab waveguide with negative permittivity and permeability," *Journal of Applied Physics*, vol. 93, no. 11, pp. 9386–9388, 2003.

[66] Jie Lu, M. Grzegorczyk, Bae-Ian Wu, Joe Pacheco, Min Chen, and Jin Au Kong, "Effect of poles on subwavelength focusing by an lhm slab," *Microwave Optical Technology Letters*, vol. 45, no. 1, pp. 49–53, Apr. 2005.

[67] H. Cory and A. Barger, "Surface-wave propagation along a metamaterial slab," *Microwave Optical Technology Letters*, vol. 38, no. 5, pp. 392–395, Sept. 2003.

[68] C. Li, Q. Sui, and F. Li, "Complex guided wave solutions of grounded dielectric slab made of metamaterials," *Progress In Electromagnetic Research, PIER*, vol. 51, pp. 187–195, 2005.

[69] V. Agranovich, Y. R. Shen, R. H. Baughman, and Zakhidov A. A., "Optical Bulk and Surface Waves with Negative Refraction," *Journal of Luminescence*, vol. 110, pp. 167–173, 2004.

[70] R. Ruppin, "Surface polaritons of a left-handed medium," *Physics Letters A*, vol. 277, pp. 61–64, Nov. 2000.

[71] A. Ishimaru, J.R. Thomas, and S. Jaruwatanadilok, "Electromagnetic waves over half-space metamaterials of arbitrary permittivity and permeability," *Antennas and Propagation, IEEE Transactions on*, vol. 53, no. 3, pp. 915–921, March 2005.

[72] C. Caloz, Cheng-Jung Lee, D.R. Smith, J.B. Pendry, and T. Itoh, "Existence and properties of microwave surface plasmons at the interface between a right-handed and a left-handed media," *Antennas and Propagation Society International Symposium, 2004. IEEE*, vol. 3, pp. 3151–3154 Vol.3, June 2004.

[73] Darmanyan S.A., Neviere M., and Zakhidov A.A., "Surface modes at the interface of conventional and left-handed media," *Optics Communications*, vol. 225, pp. 233–240(8), 1 October 2003.

[74] A. Ishimaru, S. Jaruwatanadilok, and Y. Kuga, "Generalized surface plasmon resonance sensors using metamaterials and negative index materials," *Progress In Electromagnetic Research, PIER*, vol. 51, pp. 139–152, 2005.

[75] G. Lévêque, O. J. F. Martin, and J. Weiner, "Transient behavior of surface plasmon polaritons scattered at a subwavelength groove," *Physical Review B (Condensed Matter and Materials Physics)*, vol. 76, no. 15, pp. 155418, 2007.

[76] R. W. Hamming, *Numerical Methods for Scientists and Engineers*, New York: Dover, 1973.

[77] Lei Zhuang, Guoqiang Zhu, Yunhua Zhang, and Boxun Xiao, "An improved discrete complex image method for greenprimes functions in multilayered media," *Microwave and Optical Technology Letters*, vol. 49, no. 6, pp. 1337–1340, 2007.

[78] K.A. Michalski, J.R. Mosig, and M.I. Aksun, "Enhancing the robustness of the discrete complex image method for planar multilayered media," *Microwave Conference, 2007. APMC 2007. Asia-Pacific*, pp. 1–4, Dec. 2007.

[79] B. Gustavsen and A. Semlyen, "Rational approximation of frequency domain responses

by vector fitting," *Power Delivery, IEEE Transactions on*, vol. 14, no. 3, pp. 1052–1061, Jul 1999.

[80] A. G. Polimeridis and T. V. Yioultsis, "On the efficient computation of closed-form green's functions in planar stratified media," *Int. J. RF Microw. Comput.-Aided Eng.*, vol. 18, no. 2, pp. 118–126, 2008.

[81] N. Felsen, L. B. Marcuvitz, *Radiation and Scattering of Waves*, John Wiley and Sons, 1994.

[82] E. Simsek, Qing Huo Liu, and Baojun Wei, "Singularity subtraction for evaluation of green's functions for multilayer media," *Microwave Theory and Techniques, IEEE Transactions on*, vol. 54, no. 1, pp. 216–225, Jan. 2006.

[83] Noyan Kinayman, *A Novel CAD Algorithm for the Analysis of Printed Circuits*, PhD in electrical and electronics engineering, Bilkent University, 1997.